Petrographic, fluid-inclusion, and secondary ion mass spectrometry stable isotopic (O, S) study of Mississippi Valley–type mineralization in British Columbia and Alberta

D.J. Kontak[1]*, S. Paradis[2], Z. Waller[1], and M. Fayek[3]

Kontak, D.J, Paradis, S., Waller, Z., and Fayek, M., 2022. Petrographic, fluid-inclusion, and secondary ion mass spectrometry stable isotopic (O, S) study of Mississippi Valley–type mineralization in British Columbia and Alberta; in *Targeted Geoscience Initiative 5: volcanic- and sediment-hosted massive-sulfide deposit genesis and exploration methods, (ed.) J.M. Peter and M.G. Gadd; Geological Survey of Canada, Bulletin 617, p. 203–245. https://doi.org/10.4095/327994*

Abstract: A comprehensive study of Mississippi Valley–type base-metal deposits across the Canadian Cordillera was done to compare and contrast their features. Extensive dissolution of host rocks is followed by multiple generations of dolomite cements from early, low-temperature, fine-grained to coarser, higher temperature types that overlap with Zn-Pb sulfide minerals; late-stage calcite occludes residual porosity. Dolomite is generally chemically stoichiometric, but ore-stage types are often rich in Fe (<1.3 weight per cent FeO) with small sphalerite inclusions. Sphalerite-hosted fluid inclusions record ranges for homogenization temperatures (77–214°C) and fluid salinity (1–28 weight per cent equiv. NaCl±$CaCl_2$). These data suggest fluid mixing with no single fluid type related to all sulfide mineralization. In situ secondary ion mass spectrometry (SIMS) generated $\delta^{18}O_{VSMOW}$ values for carbonate minerals (13–33‰) reflect dolomite and calcite formation involving several fluids (seawater, basinal, meteoric) over a large temperature range at varying fluid-rock ratios. Sphalerite and pyrite SIMS $\delta^{34}S_{VCDT}$ values vary (8–33‰) but in single settings have small ranges (<2–3‰) that suggest sulfur was reduced via thermochemical sulfate reduction from homogeneous sulfur reservoirs. Collectively, the data implicate several fluids in the mineralizing process and suggest mixing of a sulfur-poor, metal-bearing fluid with a metal-poor, sulfide-bearing fluid.

Résumé : Nous avons réalisé une étude exhaustive des gîtes de métaux communs de type Mississippi-Valley dans la Cordillère canadienne afin de comparer et d'opposer leurs caractéristiques. Une dissolution étendue des roches hôtes a été suivie de plusieurs générations de ciments dolomitiques allant des types précoces de basse température et à grain fin aux types plus grossiers de température plus élevée, dont la formation chevauche dans le temps celle de minéraux sulfurés à Zn-Pb; de la calcite de stade tardif colmate la porosité résiduelle. La dolomite présente généralement une chimie stœchiométrique, mais les types contemporains du stade de la minéralisation sont souvent riches en Fe (<1,3 % en poids de FeO) et présentent de petites inclusions de sphalérite. Les inclusions fluides contenues dans la sphalérite nous révèlent des plages de températures d'homogénéisation (77–214 °C) et de salinité des fluides (1–28 % d'équivalent en poids de NaCl±$CaCl_2$). Ces données suggèrent un mélange de fluides sans qu'il n'y ait un seul type de fluide qui puisse être lié à l'ensemble de la minéralisation sulfurée. La spectrométrie de masse d'ions secondaires in situ (SIMS) a généré des valeurs $\delta^{18}O_{VSMOW}$ pour les minéraux carbonatés (13-33 ‰) qui reflètent la formation de dolomite et de calcite mettant en jeu plusieurs fluides (eau de mer, fluide de bassin, fluide météorique) sur une large plage de températures avec des rapports fluide/roche variables. Les valeurs $\delta^{34}S_{VCDT}$ de la sphalérite et de la pyrite déterminées par SIMS varient (8-33 ‰), mais dans un contexte donné, elles présentent de faibles écarts (<2-3 ‰), ce qui semble indiquer que le soufre a été produit par une réduction thermochimique des sulfates provenant de réservoirs de soufre homogènes. Dans l'ensemble, les données révèlent la participation de plusieurs fluides dans le processus minéralisateur, et laissent à penser qu'il y a eu mélange d'un fluide métallifère pauvre en soufre avec un fluide sulfuré pauvre en métaux.

[1]Harquail School of Earth Sciences, Laurentian University, 935 Ramsey Lake Road, Sudbury, Ontario P3E 2C6
[2]Geological Survey of Canada, 9860 West Saanich Road, Sidney, British Columbia V8L 4B2
[3]Department of Geological Sciences, University of Manitoba, Winnipeg, Manitoba R3T 2N2
*Corresponding author: D.J. Kontak (email: dkontak@laurentian.ca)

INTRODUCTION

Carbonate-hosted base-metal (i.e. Zn-Pb) deposits of western Canada, which includes the Canadian Cordillera and the Western Canadian Sedimentary Basin, have been ascribed to Mississippi Valley–type (MVT) mineral systems. As summarized by Leach and Sangster (1993), these epigenetic deposits are stratabound, carbonate-hosted (i.e. dolostone) sulfide bodies dominated by Zn and Pb sulfide minerals (sphalerite, galena) mainly occluding porosity generated via dissolution or collapse features (e.g. breccias), which were infiltrated by saline fluids in the range of 75 to 200°C. In addition, the settings are generally confined to carbonate platform settings, typically in relatively undeformed orogenic foreland rocks, but also foreland thrust belts. Deposit formation is generally attributed to large-scale fluid migration during sedimentary basin evolution, with mineralization related to mixing of low-temperature, oxidized, base-metal–bearing fluids with another fluid that either initiates reduction of sulfate in the latter fluid or provides reduced sulfur (i.e. H_2S) at the site of mineralization (Leach et al., 2005, 2010a; Bodnar et al., 2014; Wilkinson, 2014). Although models are generally similar, they differ in how and when H_2S is generated (*see* Wilkinson (2014) for summary).

The MVT deposits of western Canada (Fig. 1, 2) vary in age, physical and chemical properties of host rocks, diversity of metal budget (Zn–Pb±Ag, ±Cu), ore textures, and temperature and chemical composition of fluids; consequently, a study of samples from MVT deposits of western Canada, incorporating the Canadian Cordillera and Western Canadian Sedimentary Basin was completed as part of a single integrated study to compare and contrast many of the relevant features of the ores with the goal of better assessing the style(s) and nature of mineralization and addressing the question of whether these reflect common or dissimilar mineralizing processes. This work follows on that of previous studies at regional and local scales (e.g. Paradis and Nelson, 2007; Paradis et al., 2007; Paradis et al., 2015; Paradis and Simandl, 2017; Drage and Paradis, 2018).

We present the results of detailed petrographic and fluid-chemical related studies on samples collected as part of previous and ongoing studies. Our approach follows in part an in situ analytical protocol for stable isotopes (O, S) that is preferred because original textural relationships are preserved in the analyzed phases. We applied this approach to carbonate rocks from both barren (Mathieu et al., 2015; Hahn et al., 2018) and mineralized (Mathieu et al., 2018) settings to document the evolution of fluids interacting with carbonate host rocks during burial. In the present study, material was subjected to 1) detailed petrological study of host rocks and sulfide minerals that included transmitted and reflect light microscopy, scanning electron microscopy–energy dispersive spectroscopy (SEM-EDS), and cathodoluminescence (CL) to establish mineral paragenesis of both barren and mineralized samples; 2) SEM-EDS chemistry to characterize carbonate phases; 3) fluid-inclusion petrography and microthermometry; and 4) in situ secondary ion mass spectrometric (SIMS) analysis for carbonate ($\delta^{18}O$) and sulfide ($\delta^{34}S$) mineral phases. The SIMS analysis was done in part to confirm results of earlier work that used the conventional bulk analysis approach (e.g. Paradis et al., 2006; Paradis et al., this volume).

GEOLOGY OF THE STUDY AREAS

The current study draws on the extensive work of other researchers who determined the context of the MVT deposits studied (Fig. 1, 2), including such relevant material and understanding as regional geology, dolomitization, and the nature of mineralization. These works include studies focused on 1) the northern (Macqueen and Thompson, 1978; Nelson et al., 1999, 2000; Paradis et al., 1999; Nelson et al., 2002; Paradis and Nelson, 2007) and southern Canadian (Nesbitt and Muehlenbachs, 1994; Vandeginste et al., 2007) Rocky Mountains; 2) the Kootenay Arc (Paradis, 2007; Paradis et al., 2015); 3) northern Alberta, the Peace River Arch (Pană, 2006; Paradis et al., 2006); and 4) the Pine Point district (Kyle, 1981; Krebs and Macqueen, 1984; Rhodes et al., 1984; Qing and Mountjoy, 1992; Qing, 1998; Adams et al., 2000; Coniglio et al., 2006; Paradis et al., 2006; Turner, 2006).

Rocky Mountain fold and thrust belt

The Rocky Mountain fold and thrust belt is part of the North American Cordillera and is a zone, up to 300 km wide, of east-verging shallow thrust faulting and décollement folding that follows the boundary between the Cordilleran miogeocline and the North American Craton from Yukon to southeast California (Burchfiel and Davis, 1972; Price, 1981). In the Canadian Cordillera, stratabound Zn-Pb occurrences are hosted in platform carbonate rocks in the Rocky Mountains, crossing from British Columbia into Alberta. Mississippi Valley–type mineralization variably occurs within carbonate strata throughout this entire belt of rocks.

Northern Rocky Mountains

The Robb Lake deposit is the largest outcropping and the most extensively explored MVT deposit in the northern Rocky Mountains, British Columbia. The deposit is hosted in Silurian to Devonian dolostone of the Mucho-McConnell Formation (Macqueen and Thompson, 1978; Nelson et al., 1999, 2000; Paradis and Nelson, 2007). The extent of this formation parallels the local trend of the Devonian shelf margin, which departs from the overall northwest Cordilleran structural trends and may reflect deep basement structures (Nelson et al., 2002). This Zn-Pb deposit consists of numerous stratabound and crosscutting mineralized zones of sphalerite, galena, and pyrite occurring as breccias, veins, and stockworks (Paradis and Nelson, 2007).

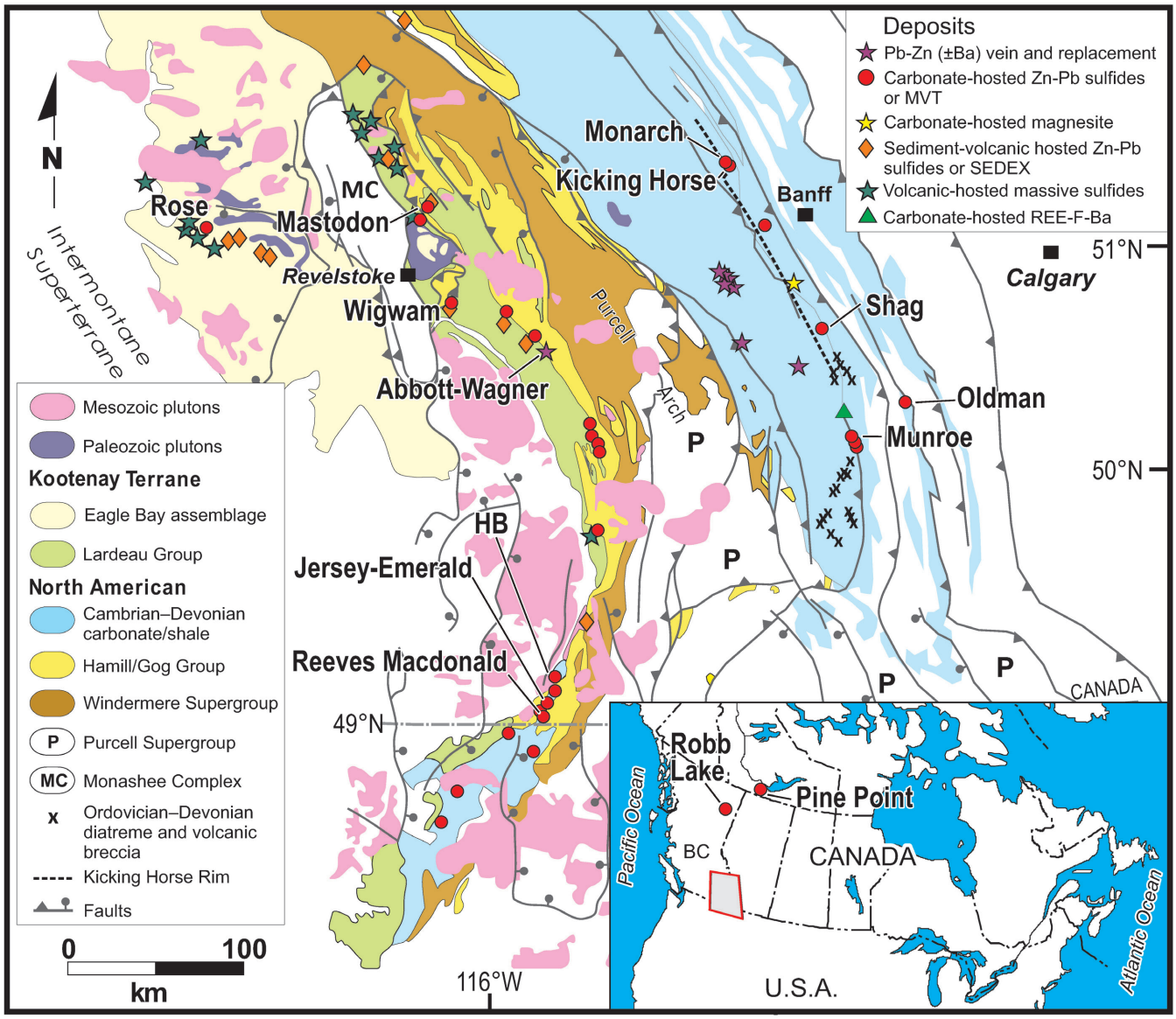

Figure 1. Regional geological map of southeastern British Columbia (outlined in inset) showing the locations of the carbonate-hosted Zn-Pb deposits discussed in this paper. The location of Pine Point and Robb Lake deposits in northern British Columbia and the Northwest Territories, respectively, are shown in the inset map and in Figure 2. *Modified from* Wheeler and McFeely (1991), Logan and Colpron (2006), and Paradis (2007).

Southern Canadian Rocky Mountains

The southern Canadian Rocky Mountains host numerous deposits and prospects, including Kicking Horse, Monarch, Shag, Munroe, and Oldman (Paradis et al., this volume). These deposits occur along the southeastern part of the Canadian Cordillera, which comprises platformal carbonate strata, deeper water basinal strata, and minor magmatic-arc rocks (McMechan, 2012). The southern Canadian Rocky Mountains are dominated by thrust faults, almost all of which are east verging (Price, 1981). The mineral deposits occur in Cambrian to Devonian carbonate reefs and breccias throughout the belt (Nesbitt and Muehlenbachs, 1994).

Kootenay Arc

The Kootenay Arc is a large, west-facing, monoclinal feature across which the change in structural level involves an aggregate stratigraphic thickness of up to 20 km (Price, 1981). The mineral deposits in the Kootenay Arc occur in a 400 km long, north-trending, arcuate structural zone that spans from northeast Washington, U.S.A., to southern British Columbia (Fyles, 1964; Höy, 1982). Samples were acquired from mineralized zones in the Reeves MacDonald deposit area (including Reeves, MacDonald, O'Donnell, Annex, Point, Prospect, B.L., No. 4, and Red Bird), Jersey-Emerald, HB, Abbott-Wagner, Rose, Wigwam, and Mastodon deposits. These deposits are hosted in miogeoclinal carbonate

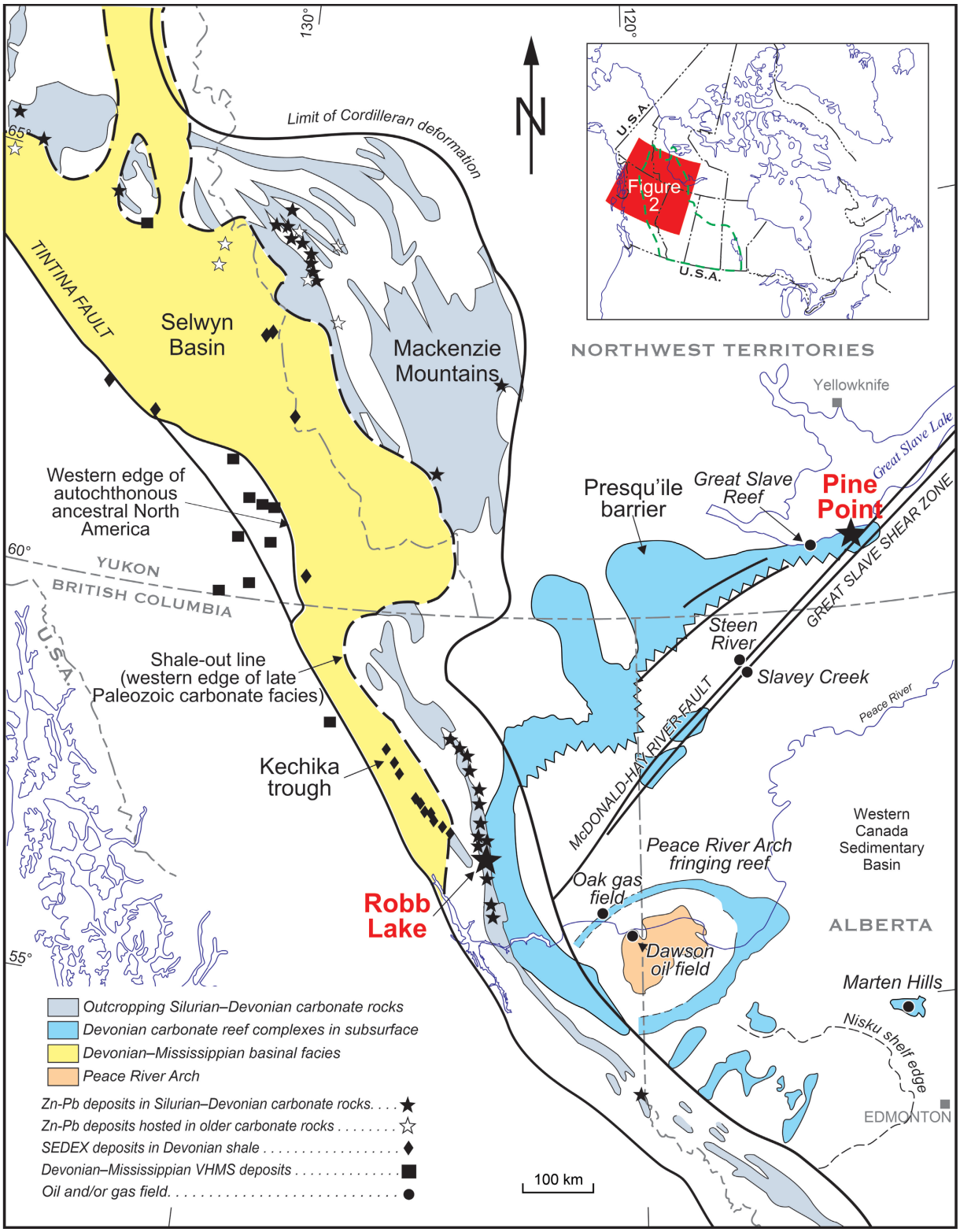

Figure 2. Location of carbonate-hosted Mississippi Valley–type Zn-Pb deposits and related areas within the Western Canadian Sedimentary Basin and the northern Rocky Mountains mentioned in this paper (i.e. Robb Lake, Pine Point, Robb Lake, Martens Hills, Steen River, Slavey Creek, Dawson oil field, Oak gas field, and Great Slave Reef). Map shows their stratigraphic, structural, and tectonic setting. The locations of sedimentary exhalative (SEDEX) and volcanic-hosted massive-sulfide (VHMS) deposits along the Devonian shelf margin are shown for reference. *Modified from* Paradis et al. (2006).

rocks of the lower Cambrian Badshot Formation and the Reeves member of the Laib Formation (Paradis, 2007; Simandl et al., this volume). Dolomitized, brecciated, and silicified carbonate rocks host the deposits, which are stratabound in nature (Paradis, 2007). Intense deformation has modified many of the primary features in these deposits, which has led to different interpretations of their formation, including sedimentary exhalative (SEDEX) and syngenetic-diagenetic origins (Irish-type; Fyles and Hewlett, 1959; Sangster, 1970; Höy, 1982; Paradis, 2007; Paradis et al., 2015).

Western Canadian Sedimentary Basin

The Western Canadian Sedimentary Basin is a vast sedimentary basin underlying 1 400 000 km² of western Canada. It consists of relatively undisturbed middle Proterozoic to lower Tertiary (i.e. Paleogene) sedimentary successions that thin to the east (Paradis et al., 2006). The stratigraphic record indicates deposition in two successive tectonosedimentary environments: 1) a late Proterozoic to Middle Jurassic passive continental margin and 2) a Middle Jurassic to Oligocene foreland basin (Price, 1994; Pană, 2006). The MVT deposits and showings are hosted by Cambrian to Devonian carbonate strata and occur over a wide area throughout the Western Canadian Sedimentary Basin in northern Alberta, with a concentration in the Pine Point district. Below we describe the two relevant settings in the Western Canadian Sedimentary Basin study areas.

North Alberta/Peace River Arch

In northern Alberta, the carbonate rocks favourable for MVT deposit exploration onlap the Precambrian crystalline basement and the unmetamorphosed early to mid-Proterozoic clastic rocks of the Athabasca Group (Pană, 2006). Most of the favourable rocks are overlain by a thick sequence of sedimentary rocks with less potential to host MVT mineralization (Pană, 2006). The most favourable rocks are exposed in the east, but are locally overlain by up to 445 m of Quaternary and Neogene sediments and sedimentary rocks (Atkinson and Lyster, 2010), and buried under post-Devonian rocks to depths of 1000 m in the west. It is not surprising, therefore, that exposure restricts exploration (and discoveries) to the shallower, northeastern portions of the Western Canadian Sedimentary Basin, where discoveries have historically been made. The samples we studied were collected from drill-core samples from occurrences that exhibited MVT-style mineralization in dolostone host rocks (Marten Hills, Steen River, and Slavey Creek).

The Peace River Arch, located in west-central Alberta, south of the McDonald-Hay River fault in the Western Canadian Sedimentary Basin (Fig. 2), is a large cratonic uplift that formed at a high angle to the passive margin during the latest Proterozoic, and remained a topographically elevated feature until the Middle to Late Devonian (Cant, 1988; Stephenson et al., 1989; O'Connell et al., 1990). The Peace River Arch was a stable, major, east-northeast–trending basement structure prior to the deposition of the Middle Devonian carbonate rocks (O'Connell et al., 1990). Our samples come from the Dawson oilfield and Oak gas field within this arch.

Pine Point district

The Pine Point mining district, southern Northwest Territories (N.W.T.; Fig. 2), is situated between the edge of the exposed Precambrian Shield to the east and the northern Rocky Mountains to the southwest and is hosted by Middle Devonian carbonate strata of the Western Canadian Sedimentary Basin (Pană, 2006). The Pine Point deposit (Fig. 2), comprising 100 Pb-Zn orebodies, is hosted in the Presqu'ile Barrier Reef, of which the dolomitized carbonate host rocks are typical of carbonate-reef complex facies (Adams et al., 2000; Hannigan, 2006). The reef is 200 m thick, more than 100 km long, and at least 10 km wide (Pană, 2006), and is mineralized at the northeastern end near Pine Point, where it partially overlies a number of aeromagnetic and gravity anomalies known as the Great Slave Shear Zone (Pană, 2006; McMechan, 2012).

Relevance of previous fluid-inclusion work

Fluid-inclusion studies of mineralized material (sphalerite), which in some cases was ore from former mine sites, and gangue (dolomite, calcite) phases in the areas of this study, have been previously reported (Roedder, 1968a; Kyle, 1981; Qing, 1991; Carrière and Sangster, 1999; Turner, 2006; Gleeson and Turner, 2007; Vandeginste et al., 2007). Summaries of the ice-melting temperatures (i.e. Tm_{ice}), salinities, and homogenization temperatures (Th; in °C) for these areas are given in Table 1. It is important to emphasize here that these data date back to the 1960s, prior to recent advances in fluid-inclusion research and understanding, which affects how such data are interpreted. Relevant in this context are: 1) post-entrapment modification of inclusions (e.g. necking; stretching due to burial); 2) classification of inclusions (i.e. primary versus secondary); and 3) application of the fluid-inclusion assemblage (FIA) approach. Criteria used by these earlier authors for primary and pseudosecondary inclusions may not conform in all cases to principles discussed by Goldstein and Reynolds (1994) and commonly adopted in the current literature (e.g. Bodnar, 2003a). Furthermore, lack of integration of thermometric measurements (e.g. Th values) with the FIA approach precludes our knowing if the data collected represent entrapment of a single fluid versus mixing of fluid populations or post-entrapment modification (e.g. Fall and Bodnar, 2018).

Table 1. Summary of fluid-inclusion data from previous studies of Mississippi Valley–type deposits in the southern Canadian Rocky Mountains and the Western Canadian Sedimentary Basin.

District	Deposit	Mineral	Stage	FI type	Tm_{ice} (ºC)	N	Th (ºC)	N	Source
NE Rocky Mountains	Robb Lake	Sphalerite	Ore stage	P, PS	-26 to -12	41	87 to 154	105	Sangster and Carrière (1994)
SE Rocky Mountains	Kicking Horse	Sphalerite	Ore stage	P, NC	-26.4 to -17.1	25	68 to 93	28	Vandeginste et al. (2007)
		Gray dolomite	Post ore	P, NC	-27.3 to -17.7	64	101 to 151	106	
		White dolomite	Post ore	P, PS, NC	-29.7 to -17.2	40	115 to 167	62	
		Coarse dolomite	Post ore	P, PS, NC	-30.5 to -17.4	33	106 to 152	35	
		Reddish dolomite	Post ore	P, PS, S, NC	-28.6 to -7.7	29	103 to 174	38	
		Calcite	Post ore	NC	-19 to -13.9	11	50 to 72	9	
SE Rocky Mountains	Monarch	Sphalerite	Ore stage	P, PS, NC	-24.8 to -18.6	22	66 to 109	32	
		Gray dolomite	Post ore	P, PS, S, NC	-27.1 to -17.3	64	93 to 146	97	
		White dolomite	Post ore	P, PS, NC	-29.9 to -18.5	58	94 to 142	78	
		Reddish dolomite	Post ore	P, PS, NC	-29.1 to -17.7	36	128 to 193	21	
WCSB	NE BC	Calcite	Post ore	P,S	-16 to -10	27	135 to 180	35	Qing (1991)
		Quartz	Post ore	NC	-13.6 to -6.8	10	165 to 211	19	
WCSB	Pine Point	Sphalerite	Ore stage	P, PS, S	-35 to -4	133	51 to 99	112	Roedder (1968)
		Dolomite	?	P, PS	-19 to -14	4	88 to 100	23	
		Calcite	Post ore	P, PS	-12 to -0.5	14			
	Pine Point	Sphalerite	Post ore	NC	-30 to -5	34	51 to 99	57	Kyle (1981)
	Pine Point District	FMD	Pre ore	P	-29.1 to -23.7	3	97 to 104	3	Turner (2006)
		Sphalerite	Ore stage	P	-33 to -22.2	9	60 to 108	9	
		CCD	Ore stage	P	-32.5 to -13.6	6	95.5 to 126	6	
		SD	Post ore	P	-18.5 to -30.6	13	86 to 112.5	13	
		Calcite	Post ore	P	-11.2 to -0.7	14	62 to 109	14	
	Pine Point	SD	Post ore	P, S	-23.5 to -14.5	4	75 to 115	24	Qing (1991)
		Calcite	Post ore	P, S	-5 to -3	8	70 to 130	8	
		SD	Post ore	P, S	-23.5 to -5.5	32	95 to 175	33	
		SD	Post ore	P, S	-34 to -5.5	34	105 to 210	74	
	Central Presqu'ile Barrier	Calcite	Post ore	P, S	-10 to -7	3	85 to 140	6	
	Northern Alberta	FMD	Pre ore	P	-13	1	130.9	1	Turner (2006)
		Sphalerite	Ore stage	NC			116	1	
		SD	Post ore	P			109 to 124	2	
		Calcite	Post ore	NC	-9.6	1	101	1	

CCD: coarse-grained crystalline dolomite; FMD: fine- to medium-grained crystalline dolomite; FI: fluid inclusions type (SD: saddle dolomite; FI type: NC: not classified; P: primary; PS: pseudosecondary; S: secondary; N: number measurements; Th: homogenization temperature; Tm_{ice} = melting temperature of ice; WCSB: Western Canadian Sedimentary Basin

The results of all the previous work show wide variations in Tm_{ice} across the study areas (–35 to –0.5°C), which indicates a wide range of salinities (0.8–28.5 weight per cent equiv. NaCl) in addition to the presence of divalent cations (e.g. Ca, Mg; Roedder, 1984). All authors cited problems with inclusions freezing due to metastability, which is not uncommon in such saline brines (e.g. Wilkinson, 2017). Given that Th values range from 50 to 211°C in different minerals and the FIA approach was not applied, it is possible in some cases that the anomalously high Th values may reflect post-entrapment modification, given that MVT deposit fluids are characterized by Th from approximately 75 to 175°C (Basuki and Spooner, 2004; Bodnar et al., 2014).

To illustrate the importance of the application of the FIA protocol to fluid-inclusion studies, we refer to the extensive study of Vandeginste et al. (2007) for the Kicking Horse and Monarch MVT settings. Their data relate to host mineral phases rather than groups of inclusions in a host or FIA; hence, all measured inclusions are assigned to a paragenetic stage. Furthermore, all data for a stage are averaged, as used in standard plots of salinity (using Tm_{ice}) versus temperature (Th). Examination of the data reveal large overall ranges for both Th and Tm_{ice} per host/stage. The Th data reveals ranges of less than 5°C to greater than 60°C per group, and plotting this reveals some relevant features (Fig. 3a): 1) an increase in Th as the range (i.e. variance) of a population increases, although for a few groups this is not the case and 2) the Th for sphalerite is less than 100°C in both the Kicking Horse and Monarch settings, also with a large variance. This data set can be interpreted in different ways, but we suggest the following and cite the recent work of Fall and Bodnar (2018) in this regard. For MVT settings, small deviations in Th are to be expected for an FIA, generally less than 5°C rather than tens of degrees Celsius. The observed large variations might reflect stretching due to subsequent post-entrapment modification (e.g. Bodnar, 2003b) related to burial. Thus, whereas sphalerite retains Th values of less than 100°C, dolomite-hosted inclusions record variable stretching. In some cases, all inclusions likely stretched, resulting in uniformly high temperatures that reflect later thermal equilibration and not initial entrapment.

The Tm_{ice} data, which are a proxy for salinity, also display large variations for a single host phase (e.g. Fig. 3b). Conversion of Tm_{ice} values to salinity indicates that average values are mostly between 21 and 28 weight per cent equiv. NaCl for the different host phases, but the overall salinity range for each of these averaged values is much larger, varying by approximately 2 to 14 weight per cent equiv. NaCl using the averaged values. Importantly, because post-entrapment modification does not affect salinity, these large ranges are real, but the data do not permit evaluation of the evolution of what is clearly an apparent mixing of fluids, as seen in Figure 3 in Fall and Bodnar (2018).

METHODS

Sample selection

A suite of 53 polished thin sections (each 30 μm thick) archived following the earlier work of Paradis (2007), Paradis et al. (2006, 2007), and Paradis and Simandl (2017) throughout the western Canada was used for an initial study of host rocks and sulfide mineralization. These polished thin sections were used for detailed petrographic, mineralogical, textural, and paragenetic studies. From these initial samples, eight were selected for SEM-EDS analysis. An additional 22 samples, also from the archived suite referred to above, were prepared as thick (100 μm), doubly polished sections for fluid-inclusion petrography and thermometric analysis. After detailed petrographic study, only six samples proved useful for microthermometry based on inclusion size and the distribution of FIA in sphalerite because this study specifically focused on ascertaining the thermal and chemical parameters during sulfide mineralization.

Petrographic analysis

Selected samples were examined using both transmitted- and reflected-light microscopic techniques at Laurentian University, Sudbury, Ontario, using an Olympus BX-51 microscope. Petrography was used to assess mineral phases, textures present in the carbonate cements and ore (sphalerite, galena) phases, and alteration types, in addition to the relative timing relationships of all of these features (e.g. Fig. 4). Our observations are summarized for mineralogy (Tables 2–4), paragenesis (Fig. 5–7), and textures (Tables 5–8).

Fluid-inclusion petrography and microthermometry

Details for classification and general features of fluid inclusions used in this study follow Goldstein and Reynolds (1994), whereby the FIA approach was used to identify and constrain fluid events (Bodnar, 2003a). Thus, only inclusions that could be petrographically demonstrated to define a fluid trapping event (i.e. a group of >2 inclusions) were considered, and these were classified as primary, secondary, pseudosecondary, or indeterminate in origin (Goldstein and Reynolds, 1994; Bodnar, 2003a). All samples were studied to identify the types and properties (e.g. V-L ratio) of the fluid inclusions to select those suitable for thermometric measurements. Only six samples spanning all mineralization types represented in the study areas were deemed useful for such work. This was due the scarcity of fluid inclusions and their small size (<5 μm), but mostly due to opacity caused by the high refractive index of sphalerite (n = 2.37) versus that of quartz (n = 1.54), which is a better host for fluid-inclusion studies. The issue of opacity could not be resolved with the use of low-Fe sphalerite (i.e. pale yellow), common in some

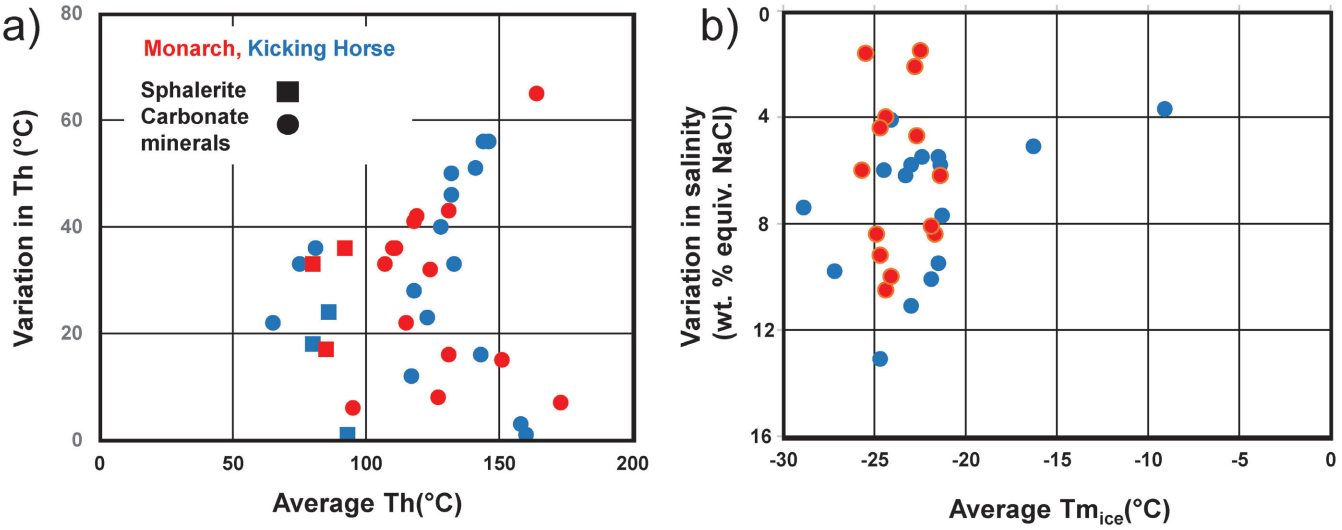

Figure 3. Plots of microthermometric data for sphalerite (squares) and carbonate (circles) phases from the fluid-inclusion study of the Kicking Horse and Monarch deposits (blue and red, respectively) as presented in Table 2 of Vandeginste et al. (2007): **a)** average Th values versus the variation in Th values (i.e. reflection of data variance); **b)** the average temperature of last ice melting (Tm_{ice}) versus the variation in salinity (in weight per cent equiv. NaCl).

samples, or the addition of an infrared camera coupled to the microscope. How this affected the thermometry work is addressed in the results section.

Fluid-inclusion microthermometry was performed at Laurentian University using a Linkham THMSG600 heating and freezing stage attached to an Olympus BX-51 microscope equipped with a QImaging capture system. A computer control unit regulated the heating and cooling rates to pre-set conditions (e.g. 150°C for heating or –100°C for cooling). The stage was calibrated using synthetic fluid inclusions for Tm_{CO_2} (–56.6°C), Tm_{ice} for pure H_2O (0°C), and the critical point of pure H_2O (374°C). Estimates of accuracy for the latter indicate values of ±0.1 to 0.2°C near 2°C and ±1 to 2°C for the extremes of the calibration. Repeated runs for natural samples in this study were made to ensure measurements were reproducible (i.e. <0.2°C and <1°C variability, respectively). Inclusion salinities were determined using the final melting temperature of ice (Tm_{ice}) for aqueous inclusions (i.e. H_2O-NaCl system) and Table 1 in Bodnar (1993). The inability to see hydrohalite melting in the studied inclusions precluded estimating the NaCl/(NaCl-$CaCl_2$) values, which is a parameter commonly reported in MVT settings (e.g. Gleeson and Turner, 2007). Thus, although salinity is reported in weight per cent equiv. NaCl, in reality the fluid inclusions contain unknown amounts of $CaCl_2$.

Cathodoluminescence

Optical microscopy CL imaging was conducted on four samples at Laurentian University using a MAAS/Nuclide Luminoscope ELM-2E. This method uses a polished thin section that is irradiated with electrons in a small vacuum chamber mounted on the stage of a petrographic microscope. The system used a 'cold cathode', whereby the discharge between cathode and anode takes place in an ionized gas. Operating conditions used an accelerating voltage of 15 kV, a current of 0.8 mA, and a vacuum of 0.5 Torr.

Secondary electron microscopy and energy dispersive spectroscopy

Imaging and analysis of select sections was done at Laurentian University using a JEOL 6400 SEM coupled to an Oxford INCA EDS solid-state detector. The following operating conditions were used: accelerating voltage of 20 kV, beam current of 1.005 nA, beam size of 1 µm, and 5 s counting time. The SEM-EDS was used to image the different carbonate types and characterize them chemically. The lower limit of detection for the latter analysis is 0.10 weight per cent, based on the repeated analysis of silicate and metal standards.

Secondary ion mass spectrometry

Samples with minerals of the appropriate petrographically determined paragenetic stage were selected for in situ O (carbonates) and S (sphalerite, pyrite) isotopic analyses using SIMS at the University of Manitoba, Winnipeg, Manitoba. Carbonate minerals were also characterized using the SEM-EDS to determine their composition (e.g. calcite versus dolomite) because the SIMS method is matrix dependent and for appropriate standards the carbonate type must be known prior to analysis. Cut-out parts of samples were polished and cleaned in a series of sonic baths and then

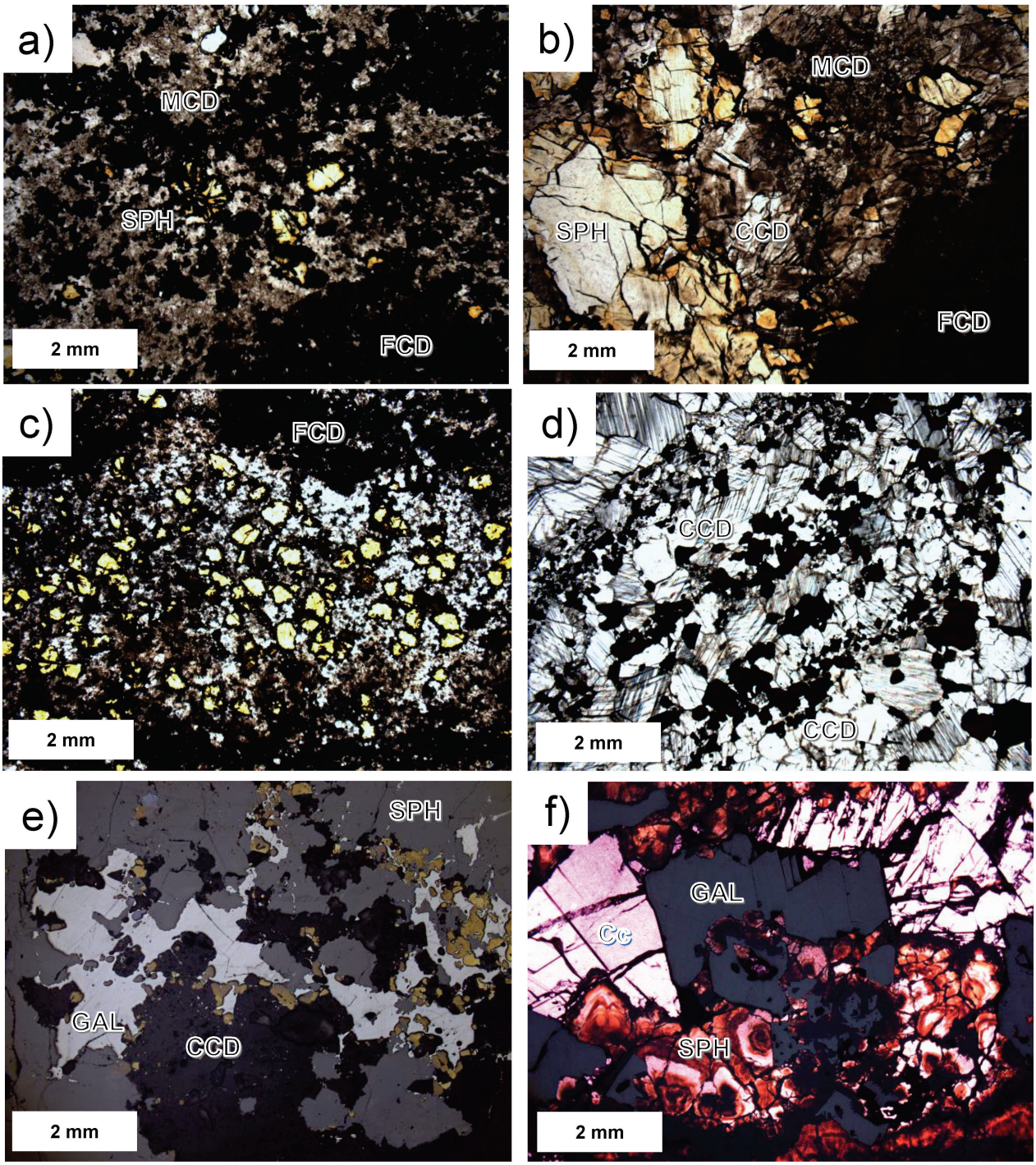

Figure 4. Typical microscopic textures in the host rocks and Mississippi Valley–type mineralization samples used in this study, as seen in transmitted light (TL) and reflected light (RL): **a)** Shag (TL): mixture of carbonate mineral types with earlier fine-grained crystalline dolostone (FCD) overprinted by colourless, translucent, and dark medium-grained crystalline dolomite (MCD) to coarse-grained crystalline dolomite (CCD) associated with pale yellow-brown anhedral sphalerite (SPH); **b)** Robb Lake (TL): coarse sphalerite associated with CCD overgrowing earlier dark MCD, which replaced FCD. The sphalerite is red-yellow on its margin and translucent and colourless in its core; **c)** Shag (TL): disseminated, equant, anhedral, pale yellow sphalerite intergrown with MCD. FCD is seen along the margins of the mineralization (*see* Fig. 9a, h for close-up); **d)** Jersey-Emerald (TL): equant sphalerite intergrown with CCD. This sphalerite appears pale yellow to orange at higher magnification (*see* Fig. 8c for close-up); **e)** Abbott-Wagner (RL): typical coarse-grained, late-stage galena (GAL) cutting earlier sphalerite and CCD; **f)** Pine Point (TL, RL): typical coarse-grained, late-stage galena cutting earlier zoned sphalerite and late-stage, cavity-filling calcite (Cc).

Table 2. Summary of the mineralogy, gangue, and ore minerals and their relative abundances for samples from the mineralized sites in the Kootenay Arc.

	Deposit	Reeves MacDonald	Jersey-Emerald	HB	Wigwam	Rose	Abbott-Wagner	Mastodon
	Number of Samples	1	4	1	1	1	1	1
Gangue minerals	FCD	***	**	***		*		*
	MCD	***	**		*		*	**
	CCD	**	***			*		
	SD	*	**			*	**	
	Cc	**	***	***	*	**		*
	Qtz	*	*	*	***	*		**
	Hem	*	**				**	
Ore mineralogy	Bar							
	PBit				*			
	Sph	**	***	***	***	***	***	***
	Gal	*					**	*
	Py	**	**	*	*		**	*
	Cpy				*		*	
	Mrc		*		*	* ?		

*: present; **: dominant; ***: abundant
Bar: barite; ; Bit: bitumen Cc: calcite; Cpy: chalcopyrite; CCD: coarse-grained crystalline dolomite; FCD: fine-grained crystalline dolomite; Gal: galena; Hem: hematite; Mrc: marcasite; MCD: medium-grained crystalline dolomite; SD: saddle dolomite; Py: pyrite; Qtz: quartz; Sph: sphalerite. The classification scheme for dolomite types is *after* Qing (1991).

Table 3. Summary of the mineralogy, gangue, and ore minerals and their relative abundances for samples from the mineralized sites in the Rocky Mountain fold and thrust belt.

	Deposit	Robb Lake	Monarch	Kicking Horse	Munroe	Shag	Oldman
	Number of Samples	2	3	4	2	7	1
Gangue minerals	FCD	***	**	***	***		
	MCD	**	*		**	*	**
	CCD	**	*	*	***	**	**
	SD	**	***	**	***	**	***
	Cc	*	*	*	*	*	**
	Qtz				*	*	*
	Hem						
Ore mineralogy	Bar						
	Bit						
	Sph	***	***	***	***	***	*
	Gal	*	**	*		*	***
	Py	**	*	**	*	*	*
	Cpy						
	Mrc						

*: present; **: dominant; ***: abundant
Bar: barite; ; Bit: bitumen Cc: calcite; Cpy: chalcopyrite; CCD: coarse-grained crystalline dolomite; FCD: fine-grained crystalline dolomite; Gal: galena; Hem: hematite; Mrc: marcasite; MCD: medium-grained crystalline dolomite; SD: saddle dolomite; Py: pyrite; Qtz: quartz; Sph: sphalerite. The classification scheme for dolomite types is *after* Qing (1991).

Table 4. Summary of the mineralogy, gangue, and ore minerals and their relative abundances for samples from the mineralized and barren sites in the Western Canadian Sedimentary Basin.

	Deposit	Pine Point	Martin Hills	Steen River	Slavey Creek	Dawson oil field	Oak gas field	Great Slave Reef
	Number of Samples	2	1	1	4	1	1	9
Gangue minerals	FCD		***	*	***	***		*
	MCD	**	**	*	**	***	***	*
	CCD	*			*		**	***
	SD	***		***	**	**	***	***
	Cc	*		**	*	***	*	**
	Qtz	*						*
	Hem							
	Bar			**				
Ore mineralogy	Bit				*			
	Sph	***			**		*	***
	Gal	**		*		*		***
	Py	*	***	*	***	***	*	*
	Cpy				*		*	
	Mrc							*

*: present; **: dominant; ***: abundant
Bar: barite; ; Bit: bitumen Cc: calcite; Cpy: chalcopyrite; CCD: coarse-grained crystalline dolomite; FCD: fine- grained crystalline dolomite; Gal: galena; Hem: hematite; Mrc: marcasite; MCD: medium-grained crystalline dolomite; SD: saddle dolomite; Py: pyrite; Qtz: quartz; Sph: sphalerite. The classification scheme for dolomite types is *after* Qing (1991).

sputter-coated with a thin gold coating. Ion detection was done on a Balzers SEV 1217 electron multiplier coupled with an ion-counting system. The instrument operated with a 20 µm sputtering diameter, a 300 V sample offset, –9 keV secondary accelerating voltage, a 247 µm slit, an 18 ns dead time, and a mass resolving power of 347. Analyses were done using a 2 nA primary beam of Cs^+ accelerated at 10 kV. Well characterized standards of calcite, dolomite, pyrite, and sphalerite were analyzed multiple times during the sessions to assess precision, providing estimated spot-to-spot reproducibility of approximately 0.5%. For the analyzed samples, the data are reported as $\delta^{18}O$ (SMOW; i.e. Vienna Standard Mean Ocean Water) and $\delta^{34}S$ (VCDT; i.e. Vienna Canyon Diablo Troilite) in per mil (‰), with errors of 1.2‰ and 0.5‰ for O and S, respectively.

RESULTS

Petrographic observations

Mineralogy

The studied samples have a mineralogy typical of MVT deposits (Leach and Sangster, 1993; Paradis et al., 2007). For example, several stages of carbonate minerals are present (Fig. 4a, b), including fine-grained crystalline dolostone and two types of coarser grained hydrothermal dolomite, referred to as medium- and coarse-grained crystalline dolomite and later saddle dolomite; this scheme follows that of earlier researchers (Qing, 1991, 1998; Qing and Mountjoy, 1994; see Fig. 3 of Qing (1998) for an explanation). The mineral residence site of the base-metal mineralization (e.g. sphalerite and galena) is sphalerite dominant where it occludes cavities (Fig. 4b), and occurs as fine-grained disseminations (Fig. 4a, c) or bands (Fig. 4d). Galena is commonly present, shows variable textural relationships with sphalerite, and is most often paragenetically later (Fig. 4e, f).

The general abundances of the gangue and ore phases at each study area are summarized in Tables 2 to 4. The estimated modes of mineral abundance are based on petrographic examination of samples and indicated as trace, minor, and major abundances. As noted above, classification of the four types of dolomite (fine-grained crystalline dolostone, medium- and coarse-grained crystalline dolomite, and saddle dolomite) follows the scheme of Qing (1991).

Some general comments on the content of the samples examined follow. Dolomite is the dominant carbonate mineral and is present as the four types noted above. Calcite is present in most of the deposits and is abundant specifically in the Kootenay Arc samples. Quartz occurs in a number

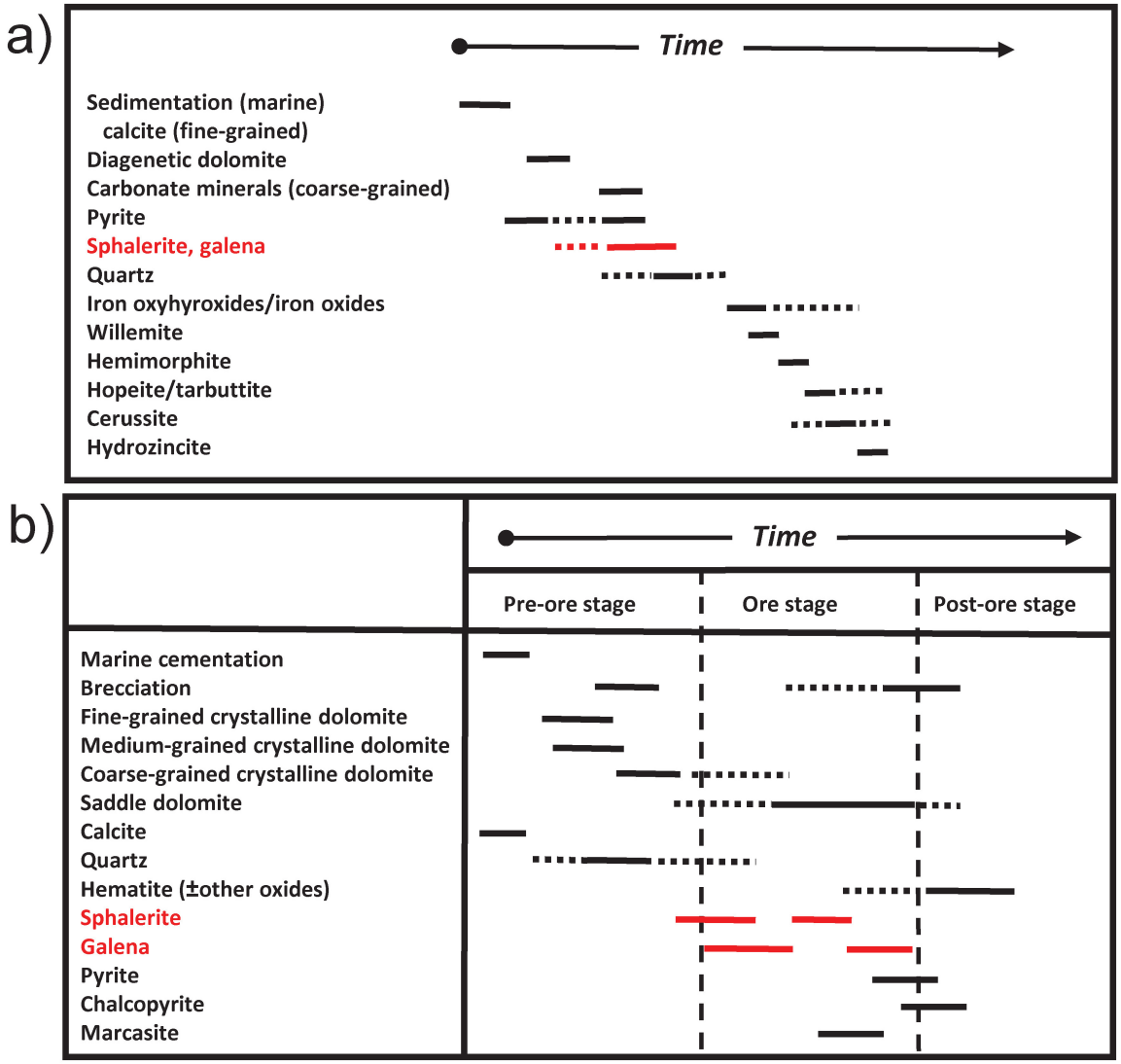

Figure 5. Proposed mineral paragenesis for Kootenay Arc deposits: **a)** paragenesis proposed by Paradis et al. (2015); **b)** paragenesis proposed in this study based on samples from our study areas and in Table 2. There are some differences in the study areas and samples used for these studies.

of samples as a late-stage, open-space filling mineral, but is notably more abundant in the Kootenay Arc samples, where, for example, it is the dominant gangue mineral in the Wigwam deposit. Hematite, barite, and pyrobitumen are post-sulfide phases. The sulfide phases documented in polished thin section are sphalerite, galena, pyrite, marcasite, and chalcopyrite; of these, sphalerite is the most abundant sulfide in all deposits except the Oldman deposit (Fig. 4), where galena dominates. In most deposits, pyrite is associated with later, post-mineralization–stage cementation. Marcasite is only observed in polished thin sections from the Wigwam and Abbott-Wagner deposits, where it predates pyrite and chalcopyrite, perhaps due to replacement of an earlier phase, and also occurs during a late fracture-filling event.

Paragenesis

Documentation of paragenetic sequences at the Zn-Pb deposits and occurrences in the studied areas have been previously presented (Kyle, 1981; Macqueen and Thompson, 1978; Qing, 1991, 1998; Paradis et al., 2006, 2015; Turner, 2006; Vandeginste et al., 2007) and is presented for deposits of the southeastern Canadian Cordillera by Paradis et al. (this volume); overall, the results of this work agree with the previous research. For this summary, the paragenetic observations are presented in sequential order, reflecting geological settings referred to above for which many similarities are apparent in terms of the timing of dolomitization and the main mineralizing event. Carbonate is present in all settings

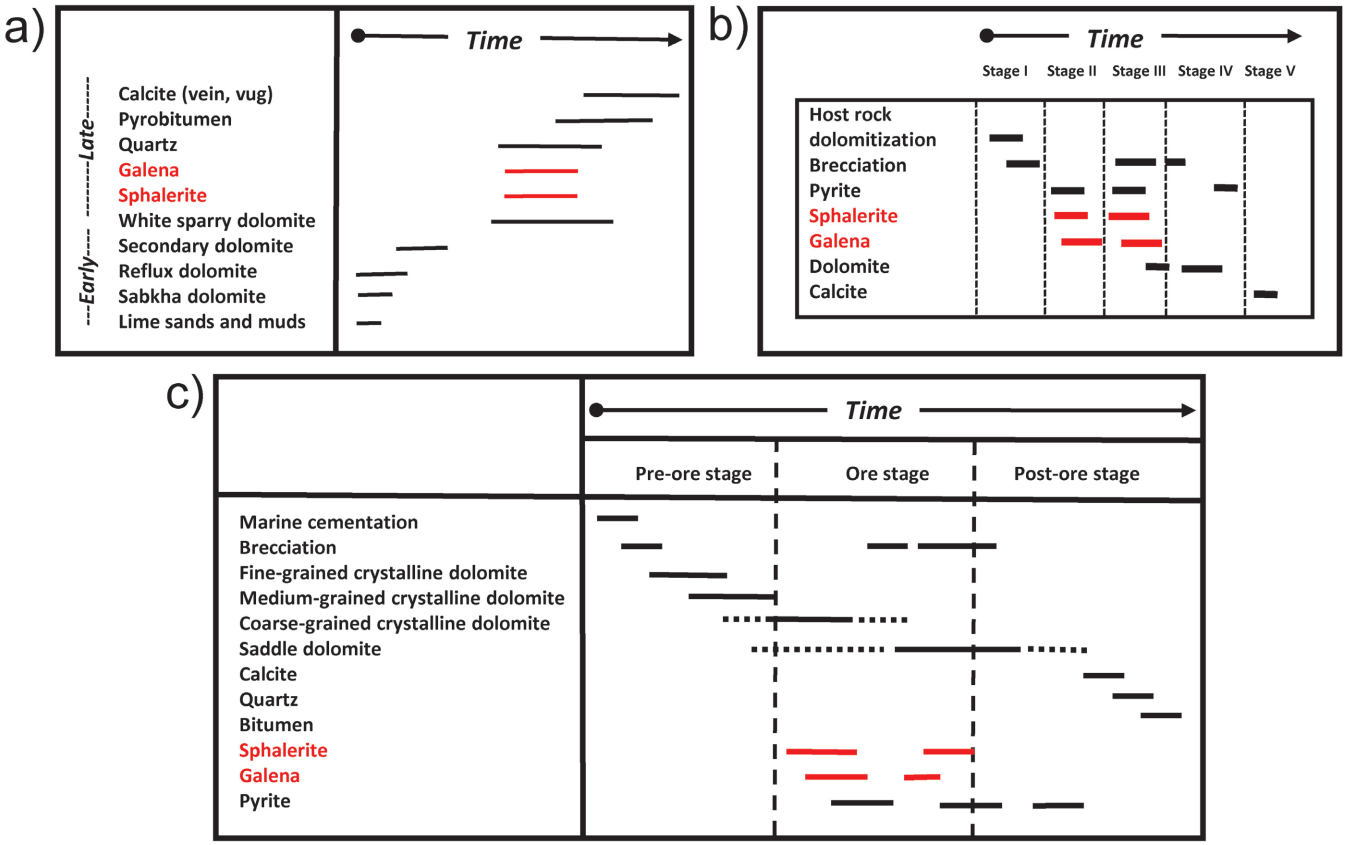

Figure 6. Mineral paragenesis for studied areas of the Rocky Mountain fold and thrust belt deposits based on previous work and this study: **a)** Robb Lake (Macqueen and Thompson, 1978); **b)** Kicking Horse and Monarch (Vandeginste et al., 2007); **c)** this study using samples described in the text and in Table 3.

in the form of early dolostone, various dolomite phases, and calcite. As noted above, the dolomitic phases are subdivided based on grain size and optical characteristics following earlier classification schemes (Qing, 1998; Turner, 2006) and show a consistent paragenesis (fine-grained crystalline dolostone to medium-grained crystalline dolomite to coarse-grained crystalline dolomite to saddle dolomite). The sulfide minerals, in order of relative decreasing abundance, are sphalerite, galena, pyrite, marcasite, and chalcopyrite. The generalized paragenetic sequences follow the convention of pre-, syn-, and post-mineralization stages corresponding to the formation and subsequent precipitation of sulfide minerals (Paradis et al., 2006).

A detailed paragenetic sequence common to all the regions, deposits, and occurrences studied cannot be established due to local deposit variations with respect to the relative timing of carbonate and sulfide phases; therefore, an overall general paragenesis is presented for each of the three main study areas (Kootenay Arc, Rocky Mountain fold and thrust belt, and Western Canadian Sedimentary Basin). The general features of each area are discussed in sequence and summarized in Tables 4 to 6.

Kootenay Arc

The paragenesis proposed for this region by Paradis et al. (2015; Fig. 5a), described as "carbonate-hosted non-sulfide Zn-Pb occurrences", is compared to our results in Figure 5a using samples from the Jersey-Emerald, Reeves MacDonald, HB, Abbott-Wagner, Wigwam, Rose, and Mastodon deposits. There are significant differences in the compared studies, specifically the lack of identified oxide phases noted in this study compared to the earlier work, which may simply reflect the different locations of samples used in the studies. In this context, the complexity of mineralization and replacement relationships in the Kootenay Arc deposits make it difficult to unambiguously establish a paragenesis due to the differences noted among the deposits studied. The paragenesis is broadly similar to that noted above for the Rocky Mountain samples, with early development of the types of dolomite, but much of the ore-stage event appears to be synchronous with the saddle dolomite in the Kootenay Arc samples. Chalcopyrite occurs in several deposits (e.g. Wigwam and Abbott-Wagner), and is paragenetically late.

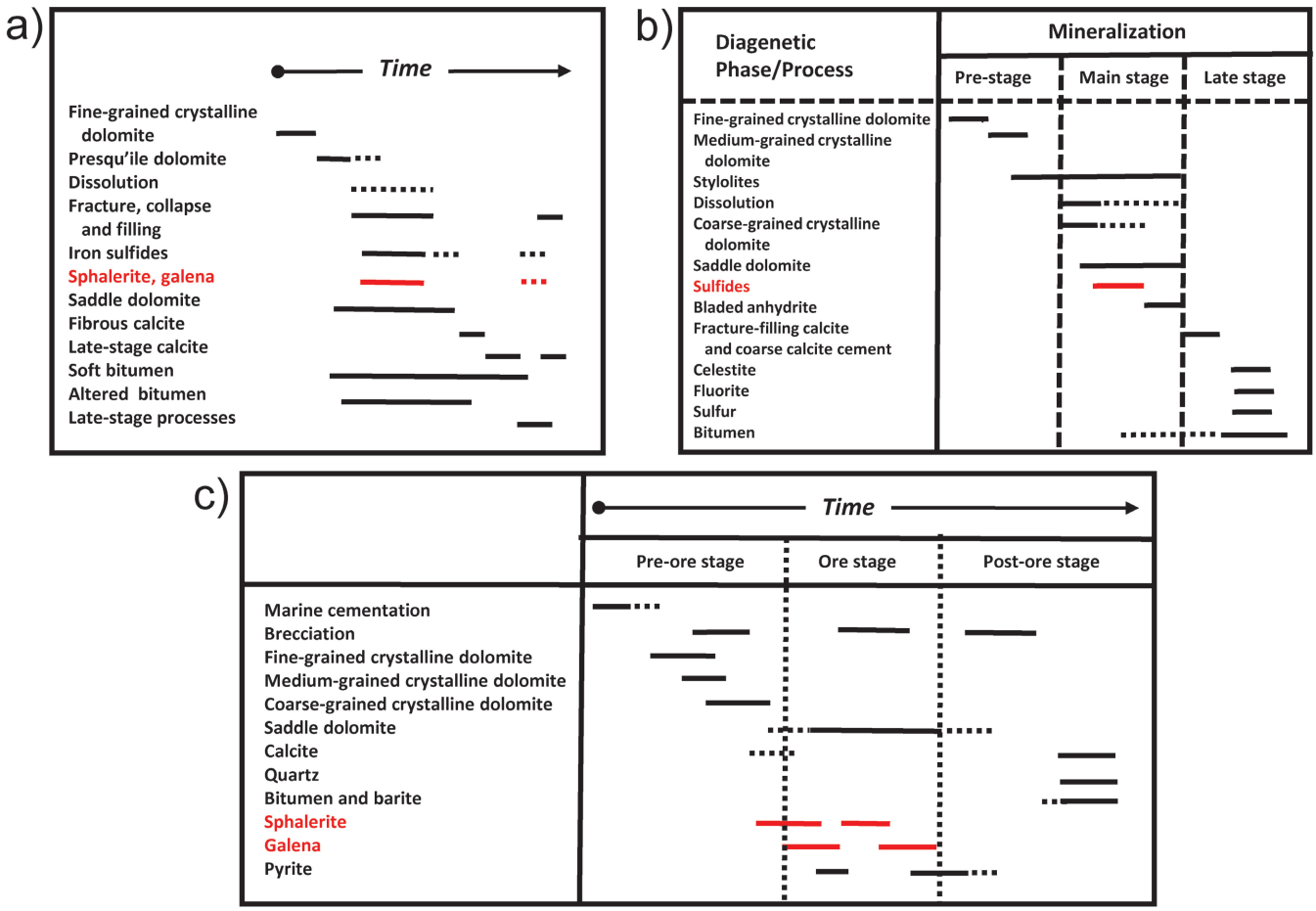

Figure 7. Mineral paragenesis for the studied areas of the Western Canadian Sedimentary Basin: **a)** Pine Point orebodies (Krebs and Macqueen, 1984); **b)** the Presqu'ile Barrier area (Paradis et al., 2006); **c)** this study based on the samples described in the text and in Table 4.

Table 5. Definitions of the textures observed in host rock and ore phases in samples of Mississippi Valley–type deposits in the Canadian Rocky Mountains and the Western Canadian Sedimentary Basin.

Texture	Definition
Crackle breccia (CB)	Slight displacement of fragments
Mosaic breccia (MB)	Fragments are largely but not wholly displaced
Rubble breccia (RB)	Fragments are completely displaced in both the host rock and sulfides
Pseudobreccia (PSE)	Breccia-like fabric produced by selective replacement of host rock fabric
Rhythmites (RHM)	Rhythmically banded ore containing distinct generations of sphalerite or gangue carbonate mineral(s) that usually develops from cycles of dissolution and open-space filling
Replacement (REP)	Original phase replaced by paragenetically later phase
Colloform (CF)	These are fine-scale (<1 mm), banded sulfides, spherulitic aggregates of colloform sphalerite, and dark bands of fibrous aggregates of crystal
Fine-grained banded ore (FGB)	Fine-scale banding (micron- to millimetre-scale bands) is common in individual crystals and in some deposits
Snow-on-roof (SOR)	Typically consists of sulfides preferentially coating the tops of crystals or breccia clasts in open space

Table 6. Summary of the textures observed in the host rocks, mineralized material, and ore minerals based on petrographic study of samples from the Kootenay Arc mineralized districts.

	Deposit	Reeves MacDonald	Jerse Emerald	HB	Wigwam	Rose	Abbott-Wagner	Mastodon
	Number of Samples	1	4	1	1	1	1	1
Host rock textures	CB		*		*		*	
	MB	*				*		*
	RB	*		*				*
Host rock mineralization textures	PSE							
	RHM	*	*					*
	REP	**	**	*	**	**	*	*
mineralization textures	CF						**	
	FGB	*						
	SOR		*		**			
	*: present; **: dominant CF = colloform banded; CB: crackle breccia; FGB: fine-grained banded; MB: mosaic breccia; PSE: pseudobreccia; REP: replacement; RHM: rhythmite layering; RB: rubble breccia; SOR: snow-on-roof.							

Table 7. Summary of the textures observed in the host rocks, mineralized material, and ore minerals of samples from the Rocky Mountains fold and thrust belt mineralized districts based on petrographic study.

	Deposit	Robb Lake	Monarch	Kicking Horse	Munroe	Shag	Oldman
	Number of Samples	2	3	4	2	7	1
Host rock textures	CB	*	*	**	**	*	
	MB	*	*	*	**	*	*
	RB	*	**	**	*	*	*
Host rock mineralization textures	PSE	*		**			**
	RHM	*	*	*		*	
	REP	**	**	**	**	**	*
mineralization textures	CF	*	**	*			
	FGB		*	*	*	*	
	SOR		*				
	*: present; **: dominant CF = colloform banded; CB: crackle breccia; FGB: fine-grained banded; MB: mosaic breccia; PSE: pseudobreccia; REP: replacement; RHM: rhythmite layering; RB: rubble breccia; SOR: snow-on-roof.						

Table 8. Summary of the textures observed in the host rocks, mineralized material, and ore minerals of samples from the Western Canadian Sedimentary Basin barren and mineralized districts based on petrographic study.

	Deposit	Pine Point	Marten Hills	Steen River	Slavey Creek	Dawson oil field	Oak gas field	Great Slave Reef
	Number of Samples	2	1	1	4	1	1	13
Host rock textures	CB		*		**	*	*	*
	MB			*	*			*
	RB			*	*			
Host rock mineralization textures	PSE				**			
	RHM							
	REP	**	*					**
mineralization textures	CF	**						**
	FGB	**						*
	SOR							

*: present; **: dominant
CF = colloform banded; CB: crackle breccia; FGB: fine-grained banded; MB: mosaic breccia; PSE: pseudobreccia; REP: replacement; RHM: rhythmite layering; RB: rubble breccia; SOR: snow-on-roof.

Rocky Mountains fold and thrust belt

Previous work on the paragenetic relationships at a few of the larger deposits in the region, such as Robb Lake (Krebs and Macqueen, 1984), Kicking Horse, and Monarch (Vandeginste et al., 2007), are compared with the results of the present study in Figure 6. Our paragenetic sequence is based on our observations also for the three aforementioned deposits in addition to Shag, Munroe, and Oldman. Our findings closely match those of Vandeginste et al. (2007), with some differences in the timing and classification of carbonate stages. Essentially, the mineralization follows a protracted development of various dolomite types and continues so that it overlaps with formation of the later coarse-grained crystalline dolomite and saddle dolomite types, which are then followed by calcite, quartz, and bitumen and pyrobitumen.

Western Canadian Sedimentary Basin

The number of previous studies of the deposits in the Western Canadian Sedimentary Basin reflects the importance of this area, as does the presence of the past-producing Pine Point MVT deposits. In this study, samples were used from Pine Point, Great Slave Reef, Slavey Creek, Dawson oil field, Oak gas field, Marten Hills, and Steen River areas (Fig. 2). Figure 7a shows the results of a previous study at Pine Point (Krebs and Macqueen, 1978) and Figure 7b shows the results of a more regional study of the Presqu'ile Barrier (Paradis et al., 2006). Figure 7a shows that the main sulfide mineralization follows a preparatory stage of dolomitized host rock that overlaps with saddle dolomite, which is followed by late calcite. Importantly, bitumen and pyrobitumen overlaps much of the paragenesis. This paragenesis is similar to that proposed by Paradis et al. (2006), but with notable additions: 1) subdivision of the coarse dolomite into coarse crystalline and saddle types; 2) addition of bladed anhydrite late in the ore stage; and 3) recognition of late celestite, fluorite, and native sulfur. The current study (Fig. 7c) provides further subdivision of the dolomite types (i.e. fine-grained crystalline dolostone, medium-grained crystalline dolomite, coarse-grained crystalline dolomite, and saddle dolomite) and also notes the presence of two generations of sphalerite, galena, and pyrite, based on petrographic study. The sphalerite occurs as 1) disseminations of fine- to coarse-grained crystals replacing the carbonate host rocks and 2) paragenetically later, massive, coarse-grained aggregates with colloform and botryoidal habits.

Host rock and mineral textures

Previous workers have demonstrated that identification of various textures at both the macroscopic and microscopic scale provides insight into physical conditions associated with base- and precious-metal mineralization (e.g. Fowler and L'Heureux, 1996; Henley and Hughes, 2000; Leach et al., 2005; Moncada et al., 2012). This topic is covered following the same three geological settings noted above to better illustrate any regional trends that might correlate with the textures. Tabulations of these observations are presented in Tables 5 to 8. Representative microscopic sphalerite textures within mineralization are presented in Figures 8 and 9.

Detailed observations indicate that nine textures (*see* Definitions in Table 5) are represented in the studied samples (the locations and number of samples used are summarized in Tables 6–8) based on petrographic characteristics. Textures were further separated into host rock, host rock mineralization, and mineralization for the various showings and deposits throughout the study areas. The textures observed are divided on a bipartite basis: 1) host rocks and cements and 2) sulfide mineralization. Host rock textures include various types of breccias (e.g. crackle, mosaic, and rubble), whereas sulfide mineralization textures include colloform, fine-grained banding, and snow-on-roof. Replacement, rhythmite, and pseudobreccia textures are present in both.

Host-rock textures

Host-rock textures reflect brecciation in various carbonate phases. Crackle breccias are minor displacements of gangue fragments, whereas mosaic breccias are largely, but not fully, displaced, and rubble breccias are fully displaced. Both crackle and mosaic breccias consist of mostly angular fragments. These textures are more common in the Rocky Mountain samples and are dominant at the Munroe, Kicking Horse, and Monarch (e.g. Fig. 8a, b) deposits. They are less dominant in the Western Canadian Sedimentary Basin deposits, and even less so in the Kootenay Arc deposits. Rhythmites or layered textures are present at seven sample sites — four from the Rocky Mountains and three from the Kootenay Arc — but they are lacking in the Western Canadian Sedimentary Basin samples.

Host rock and sulfide textures

A number of textures related to the host rock, gangue material, and mineralized ore phases are developed. Pseudobreccia was only documented at four sites: three in the Rocky Mountains and one in the Western Canadian Sedimentary Basin. This texture is considered to represent both earlier dissolution features, which created void space that was subsequently filled by carbonate and sulfide minerals, particularly sphalerite, and also post-ore modification related in part to deformation. Replacement textures occur in almost all samples throughout the study areas, except for five sites in the Western Canadian Sedimentary Basin. As noted, rhythmites (Fig. 4d) are present at seven sample of the sites in the Rocky Mountains and Kootenay Arc, but absent in all the Western Canadian Sedimentary Basin samples.

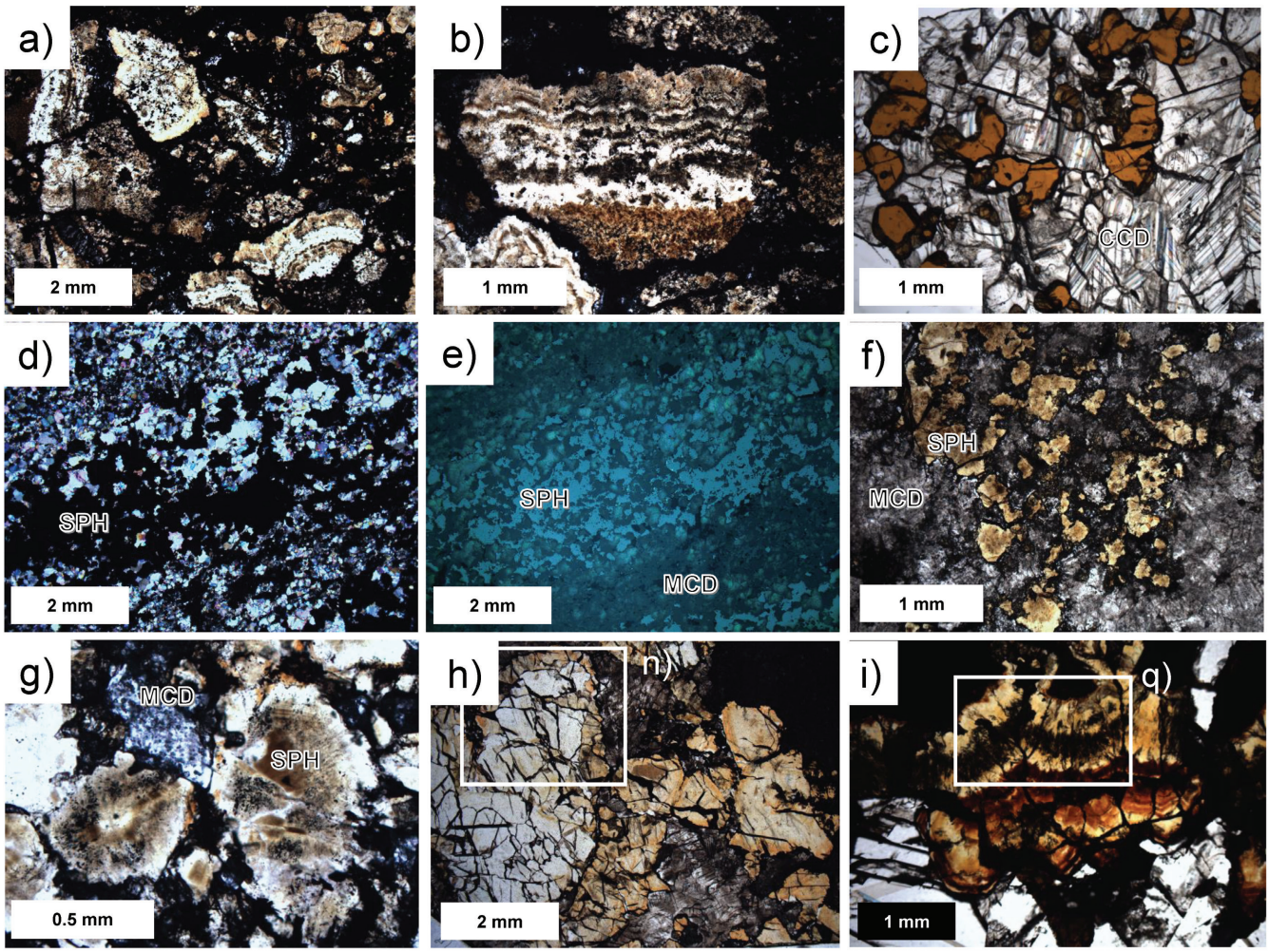

Figure 8. Representative photomicrographs of sphalerite mineralization in the studied deposit settings, taken with transmitted light (TL), reflected light (RL), and crossed nicols (CN): **a)** Monarch (TL): brecciated clasts of sphalerite in a carbonate matrix, with notable variation in the banding, colour, texture, and grain size of sphalerite; **b)** Monarch (TL): breccia clast of banded sphalerite–carbonate mineralization; **c)** Jersey-Emerald (TL): close-up of a banded ore sample showing intergrowth of yellow-brown, anhedral sphalerite with coarse-grained crystalline dolomite (CCD); **d)** Reeves MacDonald (CN): intergrowth of subhedral to anhedral sphalerite (SPH) and medium-grained crystalline dolomite (MCD); **e)** Reeves MacDonald (RL): anhedral sphalerite intergrown with MCD as a vein-like feature; **f)** Kicking Horse (TL): disseminated, subhedral, zoned, pale yellow-brown sphalerite intergrown with MCD. Finer-grained sphalerite is seen around the coarse grains, which is represented by dark material; **g)** Kicking Horse (TL): close-up of image f) showing zoned, clear to brown sphalerite and MCD. Note the dark areas in sphalerite are full of fluid inclusions; **h)** Robb Lake (TL): coarse-grained, subhedral, zoned pale to yellow sphalerite intergrown with CCD. White box is enlarged in image n); **i)** Pine Point (TL): colloform-textured, pale yellow to red-brown sphalerite. White box area enlarged in image q);

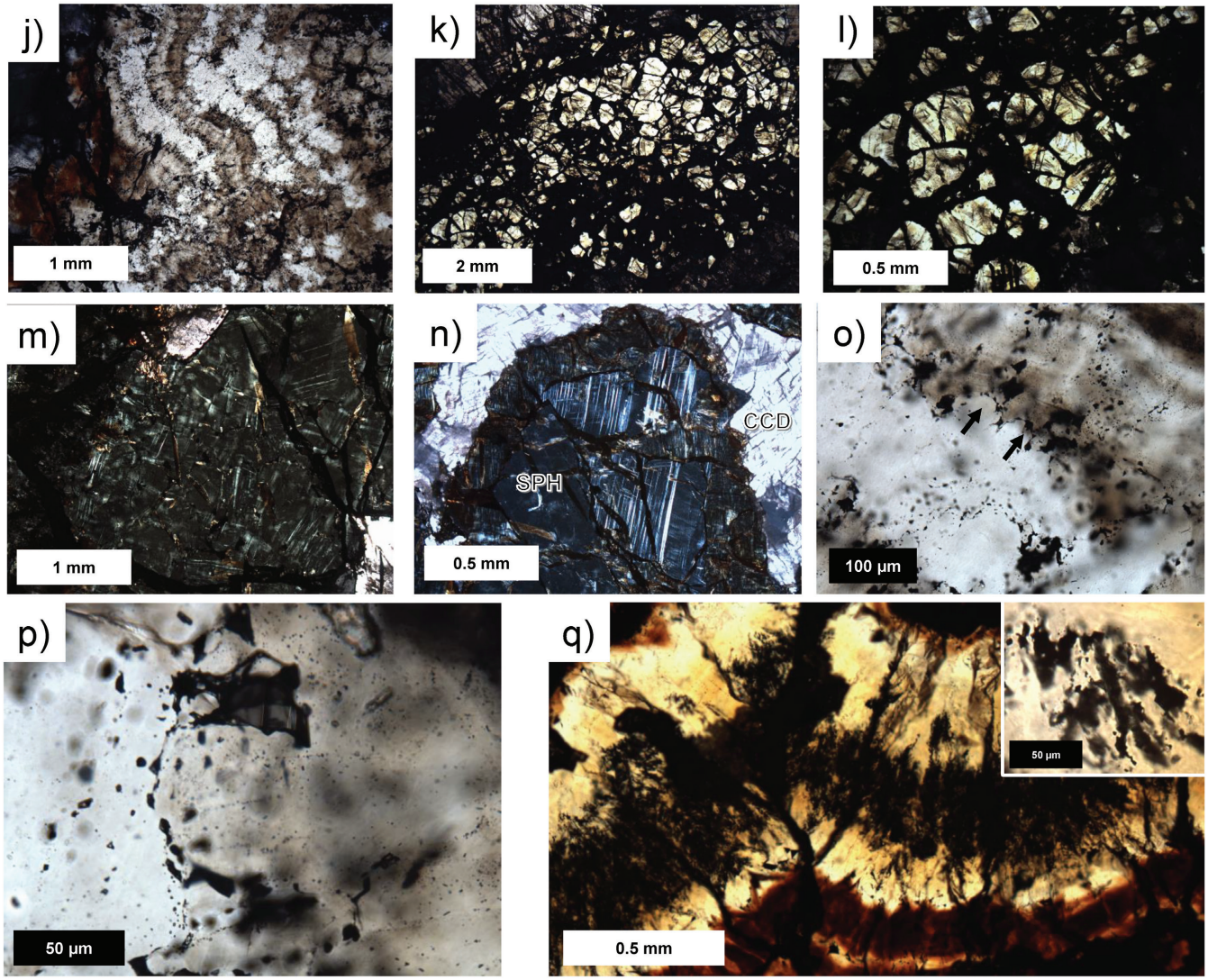

Figure 8.(cont.) j) Kicking Horse (TL): banded/colloform-textured, colourless, translucent, red-brown to pale brown sphalerite. *See* image j) for close-up of part of this image. **k)** Munroe (TL): anhedral, pale yellow to clear sphalerite with breccia texture that is cemented by fine-grained carbonate minerals; **l)** Munroe (TL): close-up of image k) showing anhedral pale yellow to clear sphalerite; **m)** Kicking Horse (CN): coarse-grained sphalerite with anisotropic behaviour due to strain and presence of twin lamellae; **n)** Robb Lake (CN): close-up of area in image h) showing subdomains and deformation twin lamellae in sphalerite surrounded by CCD; **o)** Kicking Horse (TL): close-up of image j) showing abundant, irregular-shaped, fluid inclusion forming in part along the interface of different coloured sphalerite and at the terminations of crystals (*see* black arrows); **p)** Kicking Horse (PL): close-up of image o) showing irregular-shaped, opaque fluid inclusions, the largest of which resembles decrepitate inclusions described in the literature; **q)** Pine Point (TL): close-up of image i) showing band of pale yellow sphalerite characterized by abundant, elongate fluid inclusions. Inset shows a close-up of these features.

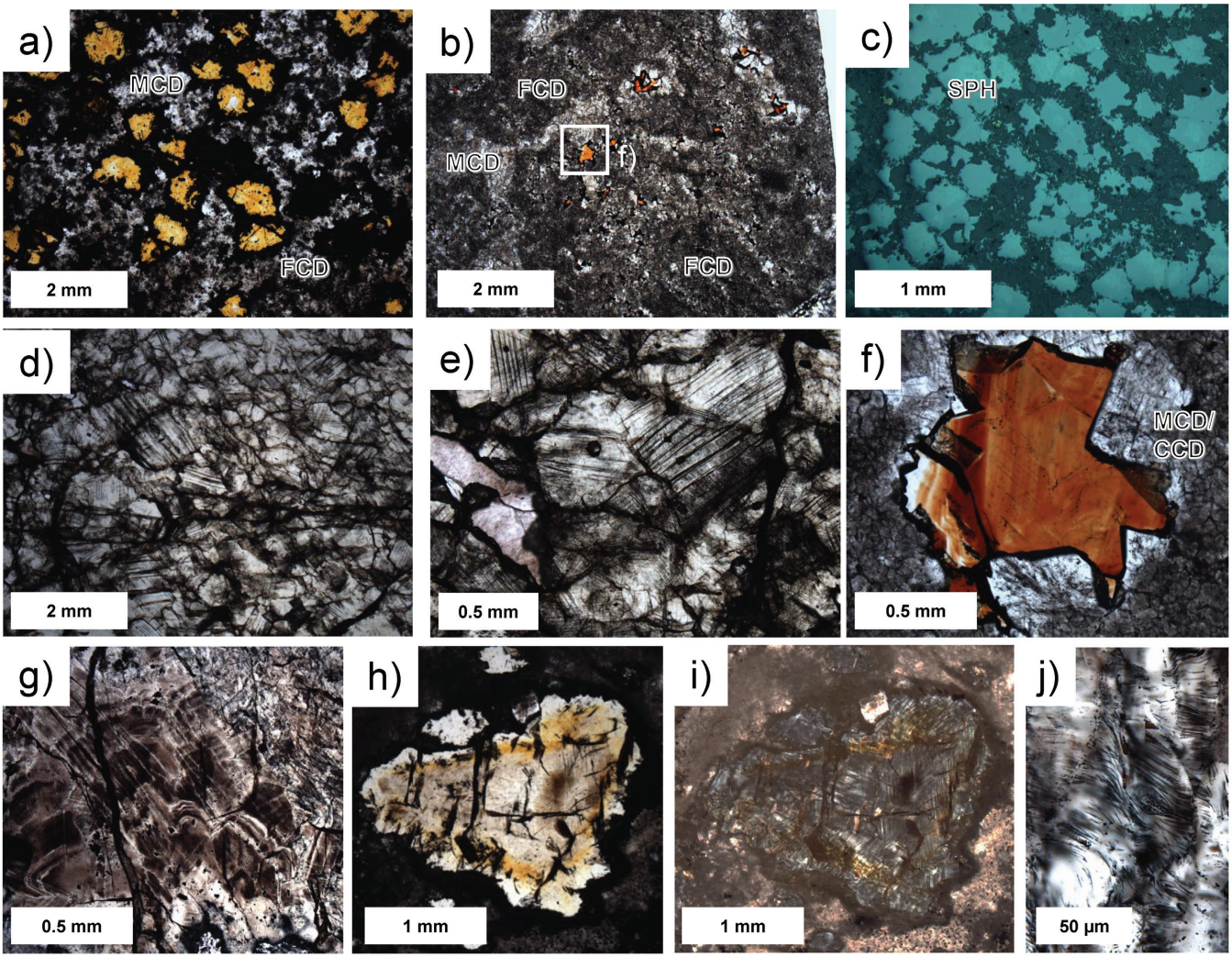

Figure 9. Representative photomicrographs of sphalerite mineralization in the studied deposit settings, taken with transmitted light (TL), reflected light (RL), and crossed nicols (CN): **a)** Shag (TL): disseminated equant, anhedral grains of pale yellow sphalerite intergrown with colourless, translucent fine-grained crystalline dolostone (FCD) and coarser grained, dark, medium-grained crystalline dolomite (MCD); **b)** BM (TL): pale red-brown, anhedral sphalerite disseminated in areas of colourless, translucent MCD that cuts FCD. White box is area enlarged in image f); **c)** Shag (RL): same sample seen in image a) showing the sphalerite (SPH) has a texture of tentacle-like apophyses that partially extend into the matrix; **d)** Rose (TL): recrystallized, coarse-grained, colourless, translucent sphalerite with subgrain development and extensive cross-cutting fractures; **e)** Rose (TL): close-up of image d) showing deformation lamellae in sphalerite that include submicron-sized opaque fluid inclusion; **f)** BM (TL): close-up of white box in image b) showing that the area around sphalerite is filled with MCD and coarser grained crystalline dolomite (CCD) that are considered to be pre- to syn-sphalerite; **g)** Abbott-Wagner (TL): pale brown to colourless, zoned sphalerite with colloform habit overgrown by finer grained sphalerite. See image j) for higher magnification of this sphalerite; **h)** Shag (TL): anhedral, pale brown and yellow to colourless sphalerite; **i)** Shag (CN): same area as in image h) showing that sphalerite is strongly anisotropic and has deformation lamellae; **j)** Abbott-Wagner (TL): pale brown to colourless sphalerite characterized at high magnification by wispy alignment of an unidentified fine-grained opaque material.

Sulfide textures

Sphalerite is the dominate sulfide mineral in most of the samples and is the most important economic mineral in the areas where mining occurred (e.g. Pine Point); thus, particular attention is given to its occurrence. There is considerable variation in sphalerite grain size, texture, habit, and colour (Fig. 8, 9).

The nature of the sphalerite mineralization varies considerably, from disseminated or isolated grains (Fig. 4a, c, 8c, 9a, b) to partly connected (i.e. net-textured; Fig. 4d, 8d, e, f, 9c) and massive (Fig. 9d, e). It occurs as cavity fillings (Fig. 4b, f, 8g, h, i, 9c, f), through replacement, to single or multiple layers (i.e. banding). The banding can be a primary feature of the ores, such as in colloform texture, which is well known at Pine Point (Fig. 8i) and also occurs in the Great Slave Reef samples, Monarch (Fig. 8a, b) and Kicking Horse (Fig. 8j). It can also occur as distinct banding (Fig. 4d), which may in part be due to post-ore recrystallization. Post-ore brecciation is dominantly brittle in nature and evident in several places (Fig. 8a; e.g. Monarch, Kicking Horse, Monroe), but ductile deformation features are also noted, referred to above as pseudobreccia and evidenced as augen-like features in samples from Shag. In some samples, there is a prominent halo of fine-grained sphalerite in the carbonate matrix around coarser aggregates, and in some samples coarser grains display tentacle-like apophyses that extend into the matrix where finer grained sphalerite occurs (Fig. 9c). The latter feature relates in part to the texture of the carbonate minerals; coarse-grained crystalline dolomite commonly surrounds this type of sphalerite and is a dissolution and precipitation feature (e.g. Fig. 9a, b, f; Putnis, 2009).

At a microscale, the texture of sphalerite varies considerably and reflects both primary features, such as faint to strong colour zoning (Fig. 8g, i, 9g, h) and colloform banding (Fig. 8b, g, i), or later overprinting processes, as represented by recrystallization textures (Fig. 8k, l). The intergrowth of both sphalerite and coarse carbonate in banded ore (Fig. 4d, 8c) is also a late feature. Well-developed anisotropy (Fig. 8m, n, 9i) is present in most samples, even though textural evidence of deformation (e.g. recrystallization of carbonate minerals) is almost always lacking. The complete absence of anisotropy in sphalerite for the Mastodon samples is atypical and distinct from samples of the other deposits. A fine wispy lamination of opaque material of unknown origin in otherwise optically clear, colourless sphalerite (Fig. 9j) is an atypical texture only evident in Abbott-Wagner samples.

Brecciation is relatively common at different spatial scales and clearly indicates post-mineralization comminution. This texture includes fragmentation of the sphalerite with cementation (Fig. 8a, b) or extensive fracturing in place, as in a crackle breccia (Fig. 8k, l).

A less common texture is snow-on-roof, which can be used as a paleotops indicator (e.g. Leach et al., 2005); this texture was documented in three samples and is only dominant in the Wigwam sample from the Kootenay Arc (images not shown). The infilling of radial cracks in fine-grained, banded sphalerite (e.g. Roedder, 1968b) by galena is also rare (e.g. Pine Point; images not shown).

The colour of sphalerite varies considerably and ranges from clear (i.e. transparent) through pale yellow and brown to dark shades of red and brown. Examples of this are further noted in our discussion of fluid inclusions below. The composition of the different-coloured varieties was not monitored in this study and thus cannot be further discussed.

Cathodoluminescence

Preliminary CL microscopy was done on a few select samples from the Kicking Horse, Jersey-Emerald, Robb Lake, and Slavey Creek deposits and occurrences to assess its potential application for studying the paragenetic evolution of carbonate minerals and how the process temporally relates to mineralization. Because CL is generated by the excitation of electrons due to specific chemical substitutions (i.e. activators; e.g. Fe, Mn, rare-earth elements (REE)) in a crystal structure, the method has the potential to track chemical changes in an evolving chemical system. Although CL has long been used to study carbonate diagenesis (e.g. Meyers, 1974; McLemore and Barker, 1987), in recent years it has been widely applied to hydrothermal systems (e.g. Götze, 2012; Götze et al., 2013).

Results for four imaged samples are presented below. These and other samples were selected based on the chemical composition of carbonate minerals and complementary petrographic studies (discussed above) and suggest that the main activator is iron, although low levels of REEs could not be identified using SEM-EDS analysis. The CL images reveal the effects of hydrothermal alteration, together with the presence of multiple generations of carbonate and sulfide minerals, which were not readily recognized using the petrographic microscope alone. These observations collectively indicate the potential application of CL imaging to better understand the paragenesis of samples in these and other similar settings.

The CL images in general show that the early, fine-grained crystalline dolostone and medium-grained crystalline dolomite phases are CL dull (Fig. 10a) and that the later coarse-grained crystalline dolomite and saddle dolomite types are CL bright (Fig. 10a, b, c). Thus, as shown in Figure 10a, the bright CL phase postdates the earlier recrystallized fine-grained matrix carbonate material. The CL-bright phases in Figure 10b and 10c occlude space generated from dissolution of the fine-grained matrix carbonate material and, furthermore, show compositional zoning as indicated by the CL red and blue in Figure 10b and the change from dark to pale red in Figure 10c; these colour changes are tentatively attributed to variations in Fe content. The CL images also clearly reveal that the coarse carbonate phases record the later development of hydrothermal carbonate minerals

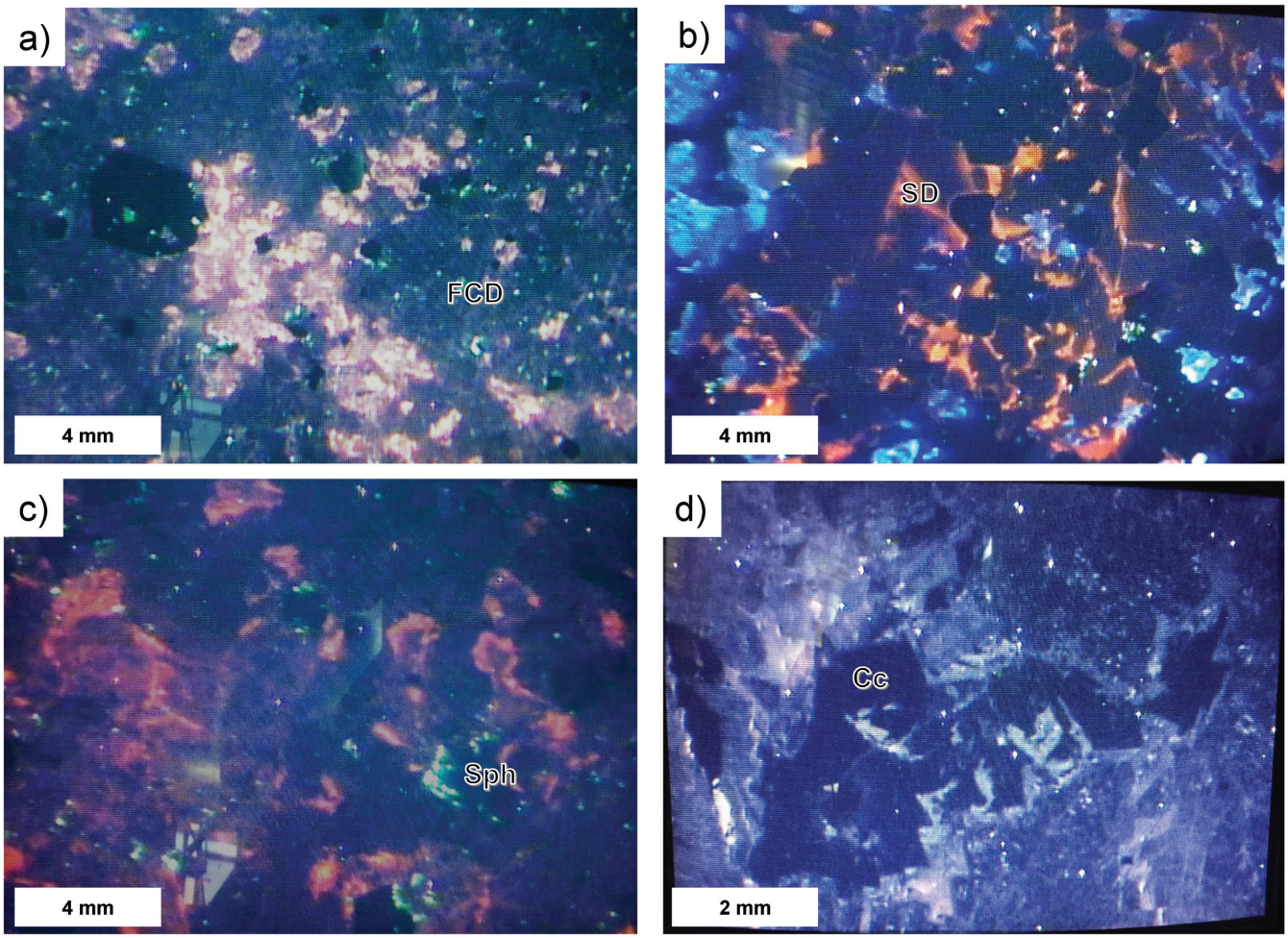

Figure 10. Cathodoluminescence (CL) images of carbonate samples from mineralized showings in the study areas. The colours are real, but without chemical data the elemental activators are unknown: **a)** sample KICK-16-5A from Kicking Horse in the southern Canadian Rocky Mountains. There is an abundance of the disseminated CL-bright green phase, which is sphalerite, within the CL-dark phase that is the fine-grained host dolomite (FCD). The CL-bright pinkish phase is a hydrothermal carbonate mineral, which accompanied the dissolution of the host rock. The dark euhedra is pyrite; **b)** sample JS-07-16-1 from the Jersey-Emerald deposit in the Kootenay Arc region. The variable CL brightness and colours (reddish and bluish) indicate that the coarse carbonate mineral phases, possibly saddle dolomite (SD), must have differing chemistry; **c)** sample Robb-6 from the Robb Lake deposit in the northern Canadian Rocky Mountains. The CL-bright red carbonate of hydrothermal origin is proximal to the CL-bright green phase, which is sphalerite (Sph); **d)** sample C-421039 from the Slavey Creek deposit in the Western Canadian Sedimentary Basin showing variably CL-bright carbonate that is zoned with the brightest phase outlining a cavity now occluded by late-stage CL-dark calcite (Cc).

at the expense of the earlier matrix carbonate material. That the later carbonate phases infill porosity generated in the former carbonate suggests that the passage of hydrothermal fluids through the samples generated space via dissolution of the host rock. The latest mineral phase in the samples is a CL-dull calcite that occludes porosity (Fig. 10d).

Another important feature observed in the CL images is the presence of sphalerite, which has a bright lime-green luminescence. The sphalerite occurs either disseminated in the fine-grained crystalline dolostone or medium-grained crystalline dolomite phases (Fig. 10a) or as coarser grained crystals occluding porosity and paragenetically overlapping formation of the coarse-grained crystalline dolomite (Fig. 10c) and saddle dolomite phases. Sphalerite in the fine-grained crystalline dolostone does not appear to be aligned along apparent fractures or brittle features in the sample (Fig. 10a) and instead appears to outline a halo of sphalerite in the matrix to the coarser saddle dolomite and coarse-grained crystalline dolomite phases.

Carbonate mineral chemistry

A total of 109 SEM-EDS analyses were completed for major- (Ca, Fe, Mg) and minor- (Mn and Zn due to sphalerite inclusions) element abundances in textural varieties

of dolomite and calcite. These results are summarized in a $CaCO_3$-$MgCO_3$-$FeCO_3$ ternary plot (Fig. 11) and in Table 9. In general, the dolomite types identified petrographically have similar chemical compositions, with MgO ranging from 25.29 to 32.81 weight per cent and CaO ranging from 17.62 to 30.21 weight per cent; the Mg-Ca ratios vary from 0.51 to 0.86. Zinc, considered to reflect the presence of micro-inclusions of sphalerite and thus syn-mineralization growth of carbonate minerals, was only noted for the coarse-grained crystalline dolomite, with up to approximately 1.0 weight per cent Zn (av. 0.13 weight per cent).

A detailed inspection of the data reveals distinct geochemical differences among the dolomite types:

- the fine-grained crystalline dolostone and medium-grained crystalline dolomite, which are texturally similar, overlap compositionally with the Fe-free coarse-grained crystalline dolomite, although some medium-grained crystalline dolomites are more rich in Mg;
- the coarse-grained crystalline dolomite falls into two groups, one free of Fe and the other bearing Fe (to 5 mol per cent $FeCO_3$);
- the saddle dolomite defines a distinct compositional space and is the most enriched in Fe (to 3.27 weight per cent FeO; 5–10 mol per cent $FeCO_3$), but there is some overlap with coarse-grained crystalline dolomite; and
- MnO was only present in the coarse-grained crystalline dolomite and saddle dolomite types.

Fluid-inclusion study

Types and characteristics of fluid inclusions

Samples were examined in detail to identify the types and properties (e.g. liquid-vapour (L-V) ratio, phases present) of fluid inclusions hosted in sphalerite to select samples suitable for thermometric measurements. Results of this detailed study, however, only produced seven samples (from six areas) that merited further analysis: these are from the Rocky Mountain fold and thrust belt (Robb Lake, Shag, Monarch, Munroe) and the Kootenay Arc (Mastodon, O'Donnell), which collectively span a variety of mineralization types. In general, these samples contained sphalerite that hosted abundant fluid inclusions (Fig. 12a, b, c, d, e, f); however, for most of these samples the small size (≤5 um) of inclusions combined with their opacity (e.g. Fig. 12b, d (inset), g, h) made their study challenging.

Where phases could be unambiguously determined, most of the fluid inclusions are two-phase aqueous type (vapour plus liquid; Fig. 12f, i), which contrasts with the opaque nature of most fluid inclusions in the same samples, for instance inclusions in Figure 12i, j are in the same area in

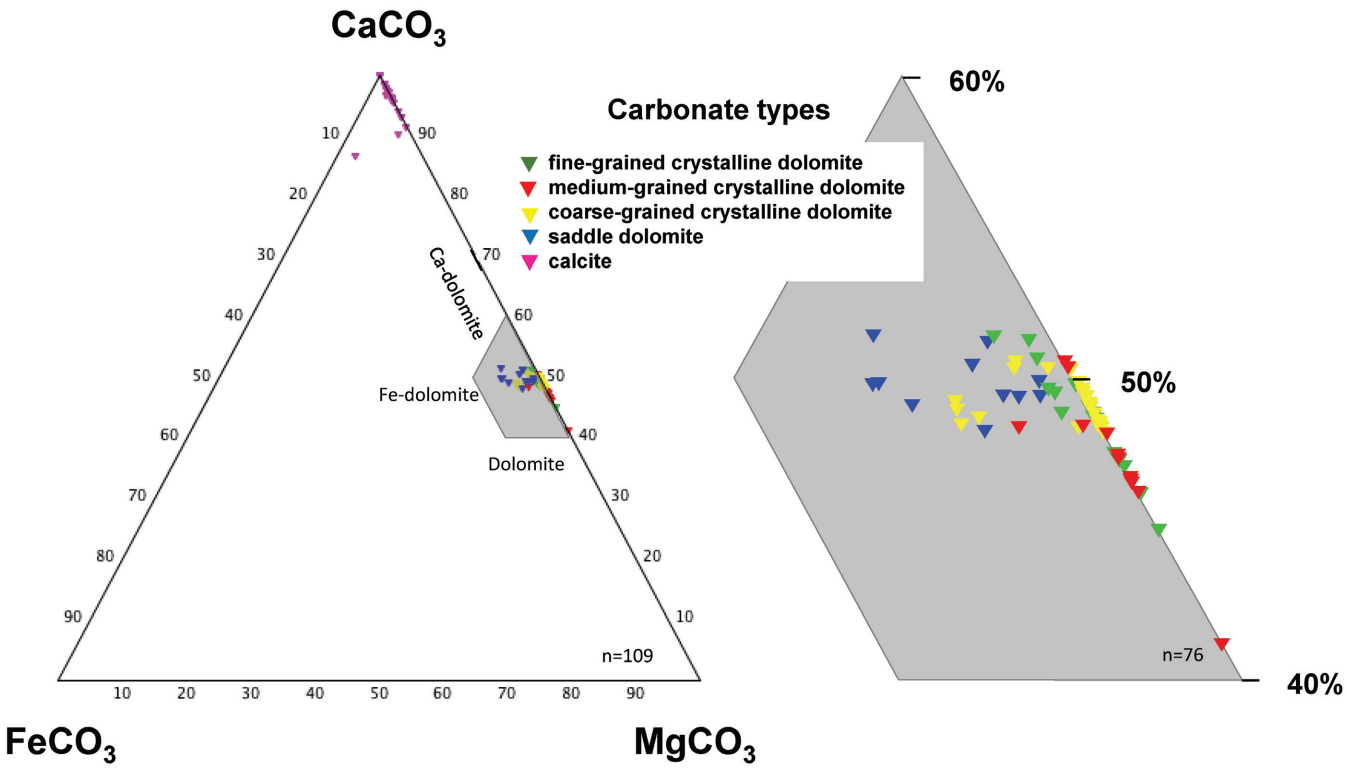

Figure 11. Ternary plot of $CaCO_3$-$FeCO_3$-$MgCO_3$ (in atomic per cent) for different dolomite types (*see* inset for types) and calcite from different study areas. Data were collected using scanning electron microscopy–energy dispersive spectrometry (SEM-EDS). The grey inset is enlarged to the right to show part of the ternary plot.

Table 9. Summary of the chemistry of carbonate mineral types encountered in studied samples of Mississippi Valley–type deposits in the Canadian Rocky Mountains and the Western Canadian Sedimentary Basin.

Phase	MgO	CaO	FeO	ZnO	MnO	Mg/Ca	$MgCO_3$	$CaCO_3$	$FeCO_3$
	←		(wt %)		→		←	(mol %)	→
FCD (n = 18)									
Min	26.00	19.97	0.00	0.00	0.00	0.55	45.00	46.88	0.00
Mean	29.46	22.42	0.26	0.00	0.00	0.64	48.40	51.27	0.33
Max	32.07	25.05	1.36	0.00	0.00	0.74	51.39	55.00	1.73
St. Dev	1.71	1.28	0.42	0.00	0.00	0.05	1.79	2.20	0.52
MCD (n = 14)									
Min	25.29	19.91	0.00	0.00	0.00	0.59	41.23	49.13	0.00
Mean	28.85	22.91	0.16	0.00	0.00	0.67	47.49	52.29	0.21
Max	32.48	30.21	1.88	0.00	0.00	0.86	50.56	58.77	2.45
St. Dev	2.11	2.65	0.50	0.00	0.00	0.07	2.22	2.41	0.66
CCD (n = 33)									
Min	25.33	18.67	0.00	0.00	0.00	0.57	48.22	46.84	0.00
Mean	30.59	22.40	0.47	0.13	0.05	0.62	49.23	50.16	0.60
Max	32.81	23.87	3.27	1.20	0.53	0.65	50.58	51.78	4.13
St. Dev	1.67	1.35	1.00	0.32	0.15	0.02	0.63	1.40	1.30
SD (n = 11)									
Min	27.62	17.62	0.80	0.00	0.00	0.51	48.29	43.27	1.09
Mean	29.13	19.62	2.55	0.00	0.11	0.57	49.87	46.72	3.41
Max	31.27	21.26	4.38	0.00	0.62	0.61	51.45	49.25	6.09
St. Dev	1.08	1.22	1.40	0.00	0.22	0.03	0.91	2.13	1.90
Cc (n =33)									
Min	18.18	0.00	0.00	0.00	0.00	0.00	69.62	0.00	0.00
Mean	44.41	1.09	0.19	0.00	0.00	0.02	96.07	3.53	0.40
Max	55.43	12.60	5.17	0.00	0.00	0.26	100.00	30.38	10.43
St. Dev	11.04	2.15	0.91	0.00	0.00	0.05	5.74	5.43	1.84

Cc: calcite; CCD: coarse-grained crystalline dolomite; FCD: fine-grained crystalline dolomite; MCD: medium-grained crystalline dolomite; SD; saddle dolomite.

Figure 12k. Halite, not uncommon in inclusions of MVT settings due to their high salinities (Basuki and Spooner, 2004; Bodnar et al., 2014), is not present in any inclusions studied, but solid phases of other minerals are rarely present and, based on their birefringence, are likely a mica and attributed to accidental trapping (Fig. 12i). Samples were examined with ultraviolet light to detect the presence of liquid petroleum, which can be a common phase in MVT deposits (Leach et al., 2005), but the lack of fluorescence indicates its absence as singular inclusion types or an immiscible phase in inclusions. Lastly, cooling (to –180°C) of what appeared to be monophase dark inclusions was done to check for the presence of COHN phases (i.e. CO_2, CH_4 or N_2; e.g. Kontak et al., 2006) or their mixtures, but no evidence of this was noted.

Inclusions were classified as primary, pseudosecondary, secondary, or indeterminate. Primary inclusions define growth zones (Fig. 12a, c, e) or occur in dense clusters within the cores of sphalerite (Fig. 12b, c, f). These primary inclusions are rarely equant (Fig. 12d, f, j), and are more commonly of irregular shape (Fig. 12b). Most inclusions are secondary and define both cleavage planes and healed fractures (Fig. 12j, k); where such inclusions decorate planes of limited extent, they are considered pseudosecondary (Fig. 12g). Due to prominent cleavage in sphalerite, intersecting planes with inclusions can be common; such inclusions are commonly equant and are also the largest of all inclusion types (Fig. 12i, j). The indeterminate type represents isolated occurrences of one or more inclusions that cannot be related to a growth zone or plane and commonly define 3-D arrays (Fig. 12h, l, m, n, o). These inclusions vary in shape from irregular to equant.

Atypical fluid-inclusion types are documented in samples from the Kicking Horse and Pine Point deposits. Inclusions from Kicking Horse are characterized as defining primary growth banding (Fig. 8j) and closer inspection reveals that they clearly decorate euhedral sphalerite crystals (Fig. 8o, p). These inclusions vary in size from small (<5 μm) to large (50–70 μm), with the latter being vapour rich based on the presence of a V-L meniscus (Fig. 8p). The very irregular shapes of these large inclusions, in addition to their atypical vapour-rich nature, suggests that they may

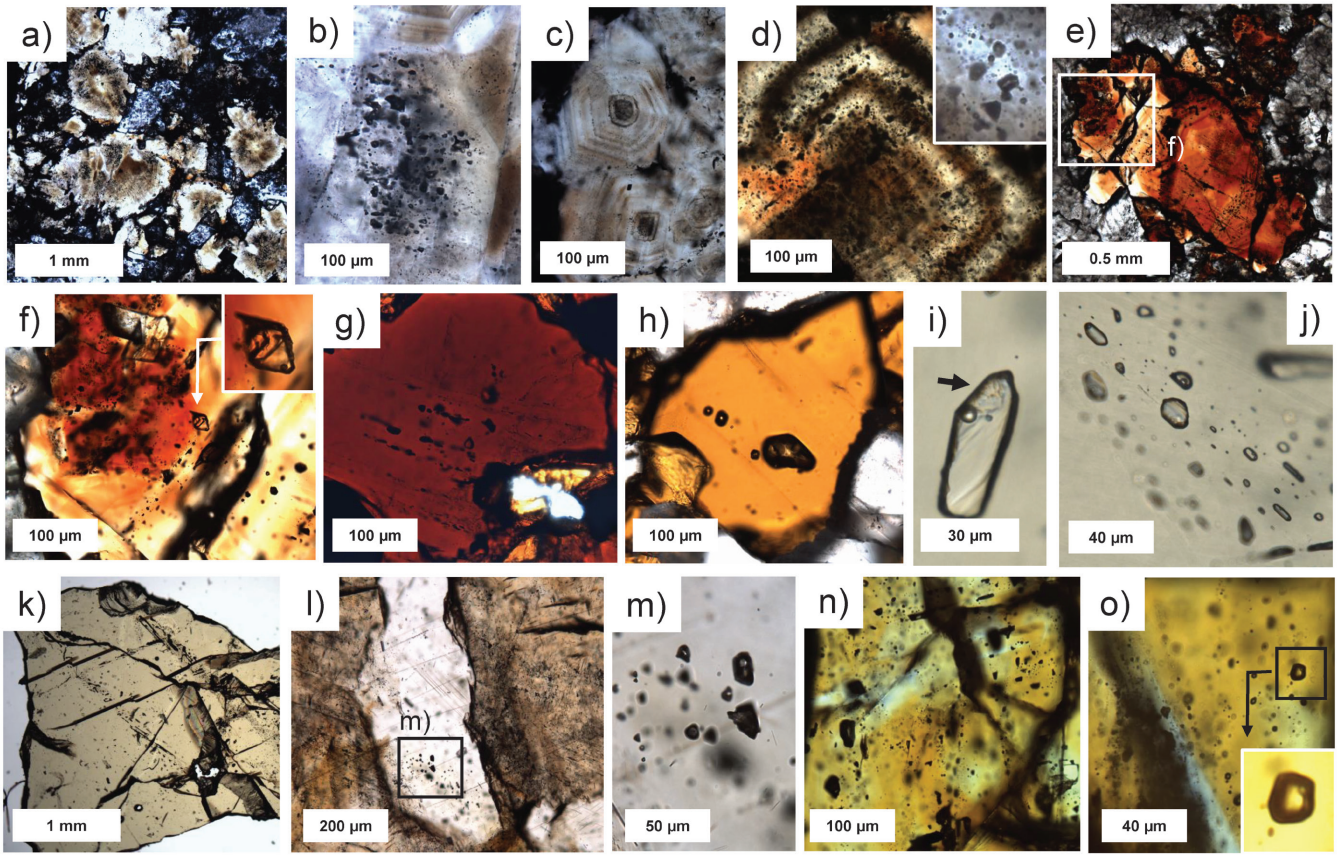

Figure 12. Photomicrographs in transmitted light of fluid inclusions (FI) hosted in sphalerite from studied deposits and districts. The inclusions are classified as primary (P), pseudosecondary (PS), secondary (S), or indeterminate (I). **a)** Kicking Horse: subhedral brown-yellow to colourless sphalerite with P-type FI defining growth zones; **b)** Kicking Horse: close-up of image a) showing a primary growth zone full of irregular-shaped opaque FI; **c)** Monarch: euhedral, zoned pale brown to colourless sphalerite crowded with opaque P-type FI; **d)** Monarch: colourless to red-brown zoned sphalerite inundated with irregular-shaped FI of P, S, and I origins. The inset image is a close-up of opaque FI; **e)** BM: subhedral zoned red-brown to colourless sphalerite with P- and S-type FI. The area outlined by the white box is enlarged in image f). **f)** BM: zoned red-brown to clear sphalerite with P- and S-type FI. Note the enlarged FI (denoted by white arrow) with a low vapour (V) to liquid (L) ratio and thus a low Th value (<80°); **g)** Jersey-Emerald: subhedral red-brown sphalerite with opaque PS-type FI in the core area; **h)** Jersey-Emerald: pale yellow sphalerite with large, irregular-shaped opaque I-type FI; **i)** Mastodon: colourless sphalerite hosting an unusually large FI with low V-L ratio, hence low-temperature origin, and an accidentally trapped solid inclusion of mica (indicated by arrow); **j)** Mastodon: colourless sphalerite hosting plane of S-type equant- to negative-shaped FI that either have low V-L ratios or are opaque; **k)** Mastodon: this chip of colourless sphalerite was used for microthermometry and it shows planes of S-type FI characterized by low V-L ratios (see images i) and j)); **l)** Robb Lake: colourless sphalerite bounded by pale yellow-brown sphalerite, with the former having opaque, PS-type FI. The colourless sphalerite may be a later generation than the brownish type. Area of black box is enlarged image m); **m)** Robb Lake: opaque PS-type equant FI in clear sphalerite; **n)** Shag: colourless to yellow, zoned sphalerite hosting small to large, equant I-type FI defining 3-D arrays. Most of the FI are opaque; **o)** Shag: yellow sphalerite with I-type FI defining 3-D array. Although most FI are opaque, one with a small V phase, outlined by black box, is enlarged in the inset image.

represent modified inclusions referred to as decrepitates, which commonly reflect pressure changes (Bodnar, 2003b). At Pine Point, atypical fluid inclusions inundate dark growth zones in colloform-banded sphalerite (Fig. 8i, q). These inclusions have several characteristics: they define primary growth bands; have a dendritic-like texture; and have elongate shapes that parallel the inferred growth direction of the host sphalerite. These features are similar to those observed in rapid growth zones of quartz from epithermal settings, which contain abundant fluid inclusions (e.g. Bodnar et al., 1985).

The size and shape of the fluid inclusions vary considerably in all samples. Inclusion size ranges from sub-micron to tens of microns, and very rarely 100 to 200 μm, within the same sample and also within a single FIA (Fig. 12h, j, m, o). Inclusion shapes also vary, commonly equant to more irregular (Fig. 12b, d, j). Necking of inclusions (Roedder, 1984) was a commonly observed feature and a wide variety of inclusion shapes can be present within a single FIA.

Most of the fluid inclusions in sphalerite appear opaque, unless the inclusions are flat and thin. Even within the same FIA some inclusions can be opaque, whereas others clearly show the V-L phases (e.g. Fig. 12i, j). That the sphalerite in these settings formed at low temperatures (*see* microthermometric data below) is consistent with the high density of the fluid inclusions (i.e. >0.95 g/cm^3), thus they will have a small vapour phase relative to liquid (V-L ratio <<0.05; see inset Fig. 12f). This observation, together with the opacity of the inclusions, hinders observation of the vapour phase, which precluded the use of most of these inclusions for Th measurements. In fact, as a result of this, only single inclusions could be measured in some FIAs. The same problem also applies to accurately determine the first melting and final ice melting temperatures (Tm_{ice}), thus the bulk composition of the system and salinity. Cycling (i.e. repeated cooling and warming; e.g. Goldstein and Reynolds, 1994) made no difference to our ability to see phases changes in the opaque inclusions. Thus, the opacity of fluid inclusions was the single most challenging aspect of obtaining microthermometric data and it limited the amount of data collected for the sphalerite-hosted inclusions discussed below.

Microthermometric measurements

Temperatures were typically lowered to between –75 and –100°C to initiate freezing of the inclusions, which generally occurred in the –35 to –60°C range, reflecting, in general, variation in salinity (low–moderate versus high, respectively) and dominance of a monovalent versus divalent cation chemical composition, that is NaCl versus Ca(-Mg) Cl_2 (Wilkinson, 2017). Where initial cooling did not freeze inclusions, successive low-temperature–cycling runs did induce freezing in some cases. Due to the issue of inclusion opacity, in some cases, isolated single inclusions or single inclusions in an FIA were measured, rather than several in an FIA, which is the preferred protocol.

The results of the cooling runs indicate a range of salinities between 1 and 28 weight per cent equiv. NaCl, but for single deposits and occurrences the data display a more restricted range, except for the Mastodon deposit, which ranges from 4 to 23 weight per cent equiv. NaCl. The narrow range of salinities noted here for a site may, however, relate to the limited amount of data and thus is more apparent than real. There is also an apparent separation of the data into two general populations of 1 to 16 and 20 to 28 weight per cent equiv. NaCl, which equates to less than 12 and greater than 20 weight per cent equiv. NaCl (Table 10, Fig. 13); again, this may also be a function of the amount of data. The salinity values also do not correlate with inclusion type.

Because the hydrohalite and ice-melting relationships could not be measured, estimates of the bulk chemistry (i.e. Ca-Na ratio), which are commonly done in similar settings (e.g. Gleeson and Turner, 2007), were not possible; however, the fact that some Tm_{ice} measurements are less than –21°C, combined with low freezing and first melting (i.e. approximately –50 to –40°C) values, does indicate the presence of divalent cations in solution (Wilkinson, 2017). Because no clathrates were observed, it can also be inferred that dissolved volatiles (COH) are absent (Roedder, 1984; Diamond, 1992).

The Th values (Table 10) show a wide range (77–214°C), as was also reported by previous researchers (Table 1). The largest amount of data for a single deposit (n = 9 FIAs) is from the Mastodon deposit, which has two populations for Th: 145 to 147°C and 188 to 214°C. The high Th values contrast markedly with the data for the other deposits, except for a single high value of 187°C for a sample from the Shag deposit.

In addition to conventional Th data (Table 4), the estimated V-L ratio of the fluid inclusions was used to infer Th based on the temperature-density plot for the H_2O system (Roedder, 1984). This approach was widely applied to the polished thin section samples studied in part because their thinner nature (i.e. 30 μm) circumvented the problem of inclusion opacity noted previously for thicker (i.e. 100–150 μm) fluid-inclusion sections. Using this approach, maximum Th values are inferred because the estimated V-L ratio is based on a 2-D image, whereas the inclusions are in general ellipsoidal to spherical. In addition, salinity will increase the minimum inferred Th values (Klyukina et al., 2019), but in general the principle is the same and a reliable estimate of Th can be made. This was validated based on correlating observations and actual Th values measured for other inclusions. This estimation method provided the means to obtain Th values for many more inclusions than were actually measured. The results, summarized in Figure 13, indicate a broad range of estimated Th values for the deposits, from approximately less than 80 to 200°C, which is in good agreement with the measured Th values. Three points are noted: 1) for any one FIA, the estimated Th is much lower than the overall range for the inclusions across the studied samples; 2) where Th values are estimated

Table 10. Summary of microthermometric data for fluid inclusions in sphalerite from studied samples of Mississippi Valley–type deposits in the Canadian Rocky Mountains.

Location	District	Sample	Chip	FIA	#FI	FI type	Tm_{ice} (ºC)	Th (ºC)	Salinity (wt % equiv. NaCl)
Robb Lake	NE RMFTB	RL-2-2	1	1	1	I	-11.1	77	15.07
		RL-2-2	1	2	1	I	-8.8	80	12.62
Robb Lake	NE RMFTB	IB-1	1	1	1	PS	-17	135	20.22
		IB-1	1	2	1	PS	-6.5	-	9.86
		IB-1	2	3	1	S	-30	99.4	28.5
		IB-1	2	4	1	S	-29.5	95.5	28
Shag	SE RMFTB	Shag-9X-B	1	1	1	PS	-18	-	20.97
		Shag-9X-B	2	2	1	S	-19.5	-	22.03
		Shag-9X-B	2	3	1	S	-18.4	187	21.26
Monarch	SE RMFTB	Mon 16-7	1	1	3	S	-0.5 to -3.6	111.5 to 119	0.88 to 5.86
		Mon 16-7	1	2	3	S	-16.7 to -17	-	19.99 to 20.22
		Mon 16-7	2	3	1	S	-2.8	102	4.65
		Mon 16-7	2	4	2	I	-0.9 to 1.1	108.3 to 110	1.57 to 1.91
Munroe	SE RMFTB	Munr-16-5	1	1	1	PS	-11.3	-	15.27
Jersey	Kootenay arc	2007-SP-031	1	1	1	PS	-9.6	-	13.51
Mastodon	Kootenay arc	08-SP-159B	1	1	2	S	-7.2 to -7.8	145 to 147	10.73 to 11.46
		08-SP-159B	1	2	1	I	-8.3	-	12.05
		08-SP-159B	1	3	2	S	-18 to -21	188 to 191	20.97 to 23.05
		08-SP-159B	2	4	3	S	-1.8 to -4	200 to 214	3.06 to 6.45
		08-SP-159B	2	5	1	I	-4.4	189	7.02
		08-SP-159B	2	6	1	I	-7.2	194	10.73
O'Donnell	Kootenay arc	2007-21-5	1	1	1	S	-3.1	121	5.11
		2007-21-5	1	1	1	I	-4.2	140	6.74

FIA: fluid-inclusion assemblage; #FI: number of fluid inclusions; FI type: I: indeterminate; PS: pseudosecondary; S: secondary; NE/SE RMFTB: northeast or southeast Rocky Mountains fold and thrust belt Th: homogenization temperature; Tm_{ice} = melting temperature of ice.

for single deposit sites such as Robb Lake, these estimates agree with the measured Th values (Fig. 13); and 3) overall, there is good correlation between the estimated and measured Th values, which supports the distribution of data in Figure 13 being fairly representative. Most important in this regard is the observation that the highest estimated Th values in Figure 14 are for Mastodon and Shag, which agrees with the actual measured Th values for these sites.

The data for Th and salinities are plotted in Figure 13. Despite limited data, there appears to be a very broad inverse trend in which salinity decreases with increasing Th. Figure 13 also highlights that for any one site there can be a large range in both salinity and Th and that, collectively, there is not a well-defined mixing trend of two endmember fluids, which instead suggests the likely mixing of several fluids of varying salinity and temperature.

Secondary ion mass spectrometry isotopic (S, O) studies

Results of in situ SIMS isotopic measurements are tabulated in Table 11, where values for dolomites (fine-grained crystalline dolostone, medium-grained crystalline dolomite, coarse-grained crystalline dolomite, saddle dolomite), calcite, sphalerite, and pyrite are listed along with comments on their occurrence. Because measurements were made on small (1 cm diameter) pucks cut from previously characterized polished thin sections, the data generated for carbonate and sulfide minerals from a single sample were for grains in close proximity (i.e. <1 cm). In most cases, several carbonate minerals in addition to sphalerite were analyzed. For this study, five representative samples for the paragenetic context of carbonate and sulfide phases were selected to provide coverage of the areas of interest. The results are considered preliminary and were done as a pilot study to assess the application of in situ measurements to these MVT deposits and occurrences.

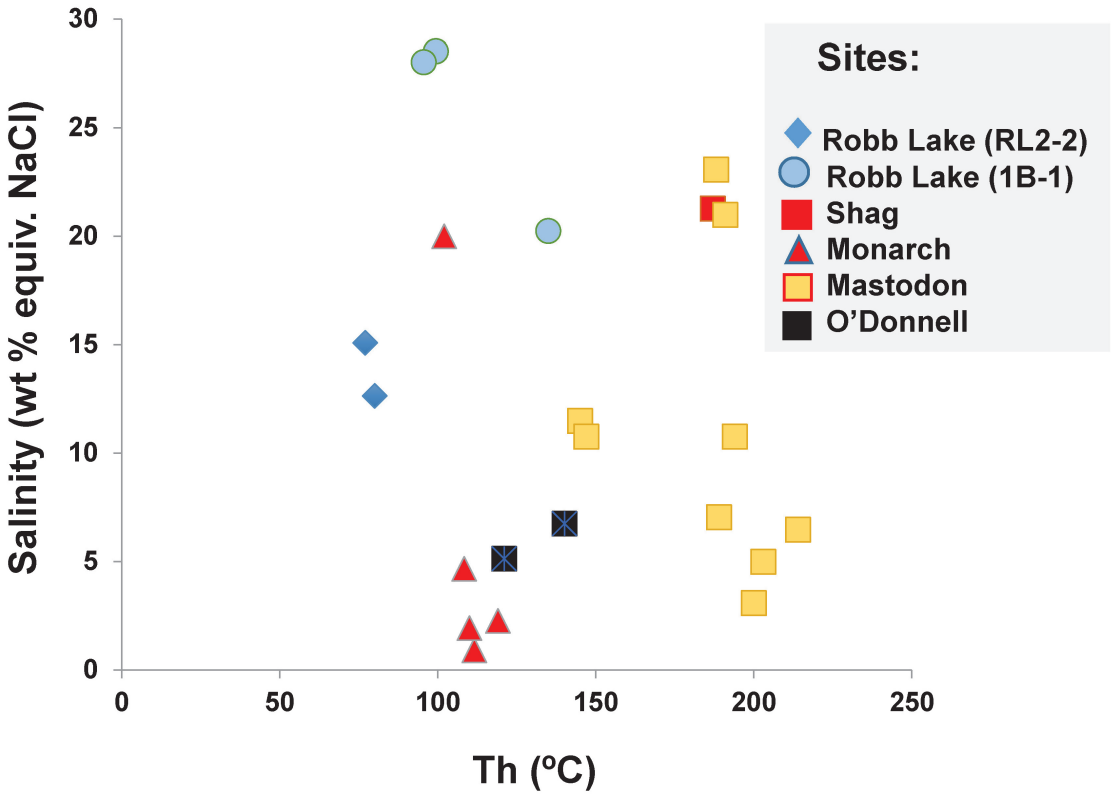

Figure 13. Microthermometric data for fluid inclusions that are part of fluid-inclusion assemblages (FIA) hosted in sphalerite from sample sites of this study, plotted as actual homogenization temperature (Th) versus salinity (weight per cent equiv. NaCl). The data are singular measurements of FIA except for Mastodon and Monarch, which represent averages for two or three measured fluid inclusions.

						
Inclusion L-V	**Very low temperature**	**Low temperature**	**Moderate to low temperature**	**Moderate to high temperature**	**High temperature**	**Very high temperature**
Th (ºC)	**80–100**	**100–120**	**120–140**	**140–160**	**160–180**	**180–200**
Deposits	**Robb Lake**	**Monarch Robb Lake (1B-1)**	**Robb Lake (1B-1) O'Donnell (2007-21-5)**	**Mastodon**	**not observed**	**Mastodon Shag**

Figure 14. Schematic showing a range of V-L ratios for aqueous fluid inclusions observed in sphalerite samples from the study areas. The estimated Th values shown are based on actual homogenization data and equate to what is inferred using the temperature-density plot for the pure H_2O system (Roedder, 1984). This approach was used to quickly infer the likely Th values for sphalerite-hosted fluid inclusions in fluid-inclusion assemblages and compare the data among the deposit settings. None of the inclusions studied were observed to have V-L ratios suggestive of Th values in the range of 160 to 180°C.

Table 11. Summary of secondary ion mass spectrometry isotopic data for carbonate (dolomite and calcite) and sulfide (sphalerite and pyrite) phases in studied samples of Mississippi Valley–type deposits in the Canadian Rocky Mountains and the Western Canadian Sedimentary Basin.

Deposit	Sample	Mineral	Relative age	$\delta^{18}O_{SMOW}$ (‰)	$\delta^{34}S_{VCDT}$ (‰)	Comments
Peace River Arch						
Dawson oil field	C-406244-C1	Calcite	Post-ore	18.4		Filling fractures after SD
	C-406244-C2	Calcite	Post-ore	15.5		Filling fractures after SD
	C-406244-C3	Calcite	Post-ore	17.6		Bordered by dolomite
	C-406244-C4	Calcite	Post-ore	17.9		Bordered by dolomite
	C-406244-C5	Calcite	Post-ore	16.4		Bordered by dolomite
	C-406244-C6	Calcite	Post-ore	16.3		Filling fractures after SD
	C-406244-D1	Dolomite	Pre-Ore	27.7		FCD; clear grains
	C-406244-D2	Dolomite	Pre-Ore	27.0		FCD; clear grains
	C-406244-D3	Dolomite	Pre-Ore	27.9		FCD; clear grains
	C-406244-D4	Dolomite	Syn-ore	31.2		Buff brown CCD-SD grains surrounded by pyrite
	C-406244-D5	Dolomite	Syn-ore	33.2		Buff brown CCD-SD grains surrounded by pyrite
	C-406244-D6	Dolomite	Syn-ore	30.2		Buff brown CCD-SD grains surrounded by pyrite
	C-406244-D4a	Dolomite	Syn-ore	31.4		Buff brown CCD-SD grains surrounded by pyrite
	C-406244-D5a	Dolomite	Syn-ore	29.0		Buff brown CCD-SD grains surrounded by pyrite
	C-406244-D7	Dolomite	Post-ore	29.2		Further into the “dark” buff brown SD
	C-406244-D8	Dolomite	Post-ore	29.1		End of SD area bordering large calcite
	C-406244-D9	Dolomite	Post-ore	27.9		Center of very clear central SD
	C-406244-D10	Dolomite	Post-ore	33.1		Outer fringe of same SD crystal
Pine Point district						
Great Slave Reef	C-421062-C1	Calcite	Post-ore	21.3		Fracture filling; associated with buff brown dolomite
	C-421062-C2	Calcite	Post-ore	23.1		Fracture filling; associated with buff brown dolomite
	C-421062-C3	Calcite	Post-ore	15.7		Comb like; surrounded by D1/D2 carbonate
	C-421062-C4	Calcite	Post-ore	17.0		Comb like; surrounded by D1/D2 carbonate
	C-421062-C5	Calcite	Post-ore	17.6		
	C-421062-D1	Dolomite	Pre-Ore	26.1		Coarse, jigsaw-like boundaries
	C-421062-D2	Dolomite	Pre-Ore	27.3		Coarse, jigsaw-like boundaries
	C-421062-D3	Dolomite	Pre-Ore	26.7		Yellowish colour
	C-421062-D4	Dolomite	Pre-Ore	27.0		Same as D3 but larger grain
	C-421062-S1	Sphalerite	Syn-ore		24.9	More orange band
	C-421062-S2	Sphalerite	Syn-ore		23.6	Dull brown grain
	C-421062-S3	Sphalerite	Syn-ore		24.7	Dull brown grain
	C-421062-S4	Sphalerite	Syn-ore		23.8	Core and more reddish than rim

Where numerals are provided (e.g. D1, SD1), they refer to the analysis for the sample being discussed. Cc: calcite; CCD: coarse-grained crystalline dolomite; FCD: fine-grained crystalline dolomite; MCD: medium-grained crystalline dolomite; SD; saddle dolomite.

Table 11. (cont.) Summary of secondary ion mass spectrometry isotopic data for carbonate (dolomite and calcite) and sulfide (sphalerite and pyrite) phases in studied samples of Mississippi Valley–type deposits in the Canadian Rocky Mountains and the Western Canadian Sedimentary Basin.

Deposit	Sample	Mineral	Relative age	$\delta^{18}O_{SMOW}$ (‰)	$\delta^{34}S_{VCDT}$ (‰)	Comments
NE Rocky Mountains Fold Belt						
Kootenay arc district	RL-2-2-D2	Dolomite	Pre/Syn-ore	16.7		MCD with clear irregular grain boundaries
	RL-2-2-D3	Dolomite	Post-ore	17.1		Clear CCD
	RL-2-2-D4	Dolomite	Post-ore	15.4		Clear CCD
	RL-2-2-D5	Dolomite	Post-ore	14.6		Coarse SD with rectangular shape
	RL-2-2-D6	Dolomite	Post-ore	13.8		Coarse SD with rectangular shape
	RL-2-2-S1	Sphalerite	Syn-ore		17.1	Coarse light brown to yellow
	RL-2-2-S2	Sphalerite	Syn-ore		19.3	Coarse light brown to yellow
	RL-2-2-S3	Sphalerite	Syn-ore		16.6	Darker red colour
	RL-2-2-S4	Sphalerite	Syn-ore		17.4	Coarse light brown to yellow
SE Rocky Mountains Fold Belt						
Kicking Horse	Kick-16-5A-D1	Dolomite	Pre/Syn-ore	19.5		Jigsaw-like MCD
	Kick-16-5A-D2	Dolomite	Pre/Syn-ore	17.3		Jigsaw-like MCD
	Kick-16-5A-D4	Dolomite	Post-ore	16.0		SD with crystalline texture
	Kick-16-5A-D5	Dolomite	Post-ore	18.4		Cross cuts SD; clear to pale brown
	Kick-16-5A-D7	Dolomite	Post-ore	19.5		SD; very clear
	Kick-16-5A-P1	Pyrite	Syn-ore(?)		31.1	Euhedral
	Kick-16-5A-P2	Pyrite	Syn-ore(?)		30.1	Euhedral
	Kick-16-5A-P3	Pyrite	Syn-ore(?)		29.3	Euhedral
	Kick-16-5A-P4	Pyrite	Syn-ore(?)		30.0	Euhedral
	Kick-16-5A-P5	Pyrite	Syn-ore(?)		31.4	Euhedral
	Kick-16-5A-P6	Pyrite	Syn-ore(?)		30.7	Euhedral
	Kick-16-5A-S1	Sphalerite	Syn-ore		33.0	Coarse, cloudy
	Kick-16-5A-S2	Sphalerite	Syn-ore		31.6	Coarse, cloudy
	Kick-16-5A-S3	Sphalerite	Syn-ore		33.2	Coarse, cloudy
	Kick-16-5A-S4	Sphalerite	Syn-ore		29.4	Coarse, cloudy

Where numerals are provided (e.g. D1, SD1), they refer to the analysis for the sample being discussed. Cc: calcite; CCD: coarse-grained crystalline dolomite; FCD: fine-grained crystalline dolomite; MCD: medium-grained crystalline dolomite; SD; saddle dolomite.

Sulfide mineral $\delta^{34}S$ data

For the sample from the Great Slave Reef area in the Pine Point district, results of four $\delta^{34}S_{VCDT}$ analyses on a single coarse grain of sphalerite intergrown with coarse carbonate minerals are uniform at 23.6 to 24.9‰ and essentially overlap each other in terms of analytical uncertainty.

For Reeves MacDonald in the Kootenay Arc district, four individual sphalerite grains intergrown with matrix carbonate material yielded $\delta^{34}S_{VCDT}$ values from 7.4 to 9.3‰. This range is slightly outside the analytical uncertainty of approximately 0.5‰ and thus indicates minor variation of $\delta^{34}S$ values among the grains.

In the Rocky Mountains, data were acquired for the Robb Lake and Kicking Horse deposits. For Robb Lake, four analyses of coarse yellow to reddish sphalerite intergrown with carbonate minerals yielded $\delta^{34}S_{VCDT}$ values of 16.6 to 19.3‰. These values are well outside of the analytical uncertainty and thus must either reflect differences in the $\delta^{34}S_{H_2S}$ values of the mineralizing fluid or variable processes of sulfide formation at this site, which generated different $\delta^{34}S_{H_2S}$ values. For Kicking Horse, $\delta^{34}S$ values were obtained for both pyrite and sphalerite. Small, euhedral pyrite grains (n = 6) in close proximity have similar $\delta^{34}S_{VCDT}$ values from 29.3 to 31.4‰. In contrast, a total of four analyses were made on two grains of coarse sphalerite. In one grain (S1, S3) the $\delta^{34}S_{VCDT}$ values were similar at 33.0 and 33.2‰, respectively, whereas the other grain (S2, S4) had values of 29.4 and 31.6‰, respectively. Thus, the $\delta^{34}S_{VCDT}$ values for both pyrite and sphalerite are overall similar, but the total range of 2.3‰ is slightly more than expected for analytical variation.

Carbonate mineral $\delta^{18}O$ data

Results for $\delta^{18}O_{carbonate}$ for a sample from the Dawson oil field yielded data for pre- and syn-ore dolomite and post-ore dolomite and calcite. Three analyses of pre-ore fine-grained crystalline dolostone in close proximity yielded essentially identical $\delta^{18}O_{SMOW}$ values of 27.0 to 27.9‰ (D1–D3). For the syn-ore coarse-grained crystalline dolomite, a total of five analyses made in the same area (D4–D6, D4a, D5a), gave $\delta^{18}O_{SMOW}$ values of 29.0 to 33.2‰, outside the range of analytical error. For post-ore coarse saddle dolomite, two analyses each of two grains yielded $\delta^{18}O_{SMOW}$ values of 29.1 and 29.2‰ (D7, D8) and 27.9 and 33.1‰ (D9, D10). For the post-ore calcite, six analyses of cavity-filling material in two areas gave $\delta^{18}O_{SMOW}$ values of 15.5 to 18.4‰ (C1, C2, C6) and 16.4 to 17.9‰ (C3–C5), which together fall outside the range due to analytical variation.

For the Great Slave Reef sample, pre-ore dolomite and post-ore calcite were analyzed. Two areas of pre-ore coarse-grained crystalline dolomite yielded similar $\delta^{18}O_{SMOW}$ values of 26.1 and 27.3‰ (D1, D2) and 26.7 and 27.0‰ (D3, D4). Two cavity fills of post-ore calcite were analyzed; the first yielded $\delta^{18}O_{SMOW}$ values of 21.3 and 23.1‰ (C1, C2) and the second yielded 15.7 to 17.6‰ (C3–C5).These post-ore calcites therefore have very different δ18O signatures from one another.

In the Kootenay Arc, data for the Reeves MacDonald deposit were obtained for pre-ore fine-grained crystalline dolostone and post-ore calcite. For pre-ore fine-grained crystalline dolostone, three analyses of separate grains in close proximity yielded $\delta^{18}O_{SMOW}$ values of 22.2 to 26.0‰ (D1–D3). For post-ore calcite, two cavity fills had similar $\delta^{18}O_{SMOW}$ values in terms of the analytical uncertainty, at 19.8 to 22.0‰ (C1–C5) and repeat analysis of two samples (C3, C4) returned similar values of 21.1 and 19.8‰, respectively.

In the Rocky Mountains, data were obtained for the Robb Lake and Kicking Horse deposits. For Robb Lake, early medium-grained crystalline dolomite and syn-ore coarse-grained crystalline dolomite had $\delta^{18}O_{SMOW}$ values of 13.4 and 16.7‰ (D1, D2). These values differ by more than the expected analytical variation. For post-ore coarse saddle dolomite, four analyses yielded $\delta^{18}O_{SMOW}$ values of 17.1 and 15.4‰ (D3, D4) and 14.6 and 13.8‰ (D5, D6) for two grains in close proximity. Intragrain variations are analytically similar, but the intergrain differences are analytically meaningful. For the Kicking Horse deposit, two analyses of pre-/syn-ore medium-grained crystalline dolomite in close proximity yielded $\delta^{18}O_{SMOW}$ values of 19.5 and 17.3‰ (D1, D2), whereas three analyses of coarse post-ore saddle dolomite (D4, D5, D7) gave $\delta^{18}O_{SMOW}$ values of 16.0 to 19.5‰, which fall outside of the expected analytical variation. Thus, the $\delta^{18}O_{SMOW}$ values of all the dolomite types overlap, regardless of their relative timing.

DISCUSSION

General deposit characteristics

In this study, we used, where possible, the same classification for all ore and gangue phases as previous researchers of the same study areas to facilitate better delineation of both local and regional variations in deposit features. Based on the petrographic study of samples using transmitted and reflected light microscopy, SEM-EDS, and CL, a mineral paragenesis was constructed for each area and compared and contrasted among the deposits and occurrences studied. The overall paragenesis we developed for the sites indicates that in all cases an initial marine cementation was followed by subsequent widespread dolomitization linked to progressive development of specific textural types of dolomite (i.e. fine-grained crystalline dolostone through saddle dolomite) and is in agreement with the conclusions of many previous studies (e.g. Qing 1991, 1998; Qing and Mountjoy, 1994; Nelson et al., 2002; Paradis et al., 2006; Paradis and Simandl, 2019). The paragenetic sequences are similar, despite the age difference of the host rocks and the time of fluid flow. Cathodoluminescence imaging of the few samples with favourable mineral chemistry (i.e.

elemental activators) shows that these samples accurately record the textural modification of the carbonate rocks during diagenesis with the formation of early fine-grained crystalline dolostone through to medium-grained crystalline dolomite and finally the coarse-grained crystalline dolomite and saddle dolomite phases. The overlap in all cases of the coarsening of the dolomites with sulfide formation signals the significance of this textural stage of development in terms of a mineralizing event.

In all deposit settings, a simple sulfide mineralogy is present that consists of sphalerite, galena, and pyrite; whereas chalcopyrite and marcasite were not abundant, they are present in some of the deposits (*see* Tables 2, 3, 4). In general, sulfide precipitation begins with a first generation of sphalerite, galena, and pyrite and is subsequently followed by these same mineral phases, punctuated by a stage of brecciation, which is most pervasive and apparent for the limited samples studied from Pine Point. The latter sulfide formation is accompanied by a second stage of dolomitization, represented by the coarse-grained crystalline dolomite and saddle dolomite, which are syn- or post-sulfide stage. The latter dolomites (coarse-grained crystalline dolomite, saddle dolomite) have Fe contents that are higher than the other dolomites (Fig. 11) and, further, some coarse-grained crystalline dolomite contains Zn due to the presence of micro-inclusions of sphalerite. Late vug- and fracture-filling calcite and quartz is in all of the deposits. The Kootenay Arc deposits also have a late hematite filling, which suggests oxidation of the system (Paradis et al., 2015).

Deposition of MVT sulfide ore and gangue minerals is the result of a complex interplay between host rock dissolution and replacement, fracturing and open space filling, sulfide precipitation, and brecciation, in addition to the mixing of different fluids (Leach et al. 2005; Wilkinson, 2014). Breccias are an important feature present in all districts; all of these process created the porosity and permeability that provides access for ingressing fluids, which is a critical part of the MVT genetic model (Leach et al., 2005). Post-ore, breccia-related textures are particularly prevalent in the Rocky Mountain deposits, which are absent in the other districts.

A variety of sulfide mineral textures are observed in the mineralized samples, with a particular focus on those in sphalerite because it is an ore (i.e. not gangue) mineral and thus provides insight to aspects of fluid conditions attending mineralization. For example, the well developed banding in sphalerite (colloform texture) is a common feature in several of the sites studied (Fig. 8, 9). The origin of this texture is variably interpreted in the literature (see reviews by Barrie et al. (2009) and Boyce et al. (2015)) as: 1) the interplay between rates of crystal growth, diffusion of solutes, and surface tension, which results in these self-organized patterns (Fowler and Heureux, 1996). Fowler and Heureux (1996) attribute these textures to the alternation of Fe and Zn contents at the 0.1 to 1.0 mm scale; however, Roedder (1968b) pointed out that this is only a generalization and not a perfect correlation based on observations at Pine Point ore; 2) colloidal suspension due to fluid mixing, as suggested for the Irish-type MVT deposits (Barrie et al., 2009; Boyce et al., 2015); and 3) supersaturation due to fluid mixing rather than colloid formation (Roedder, 1968c). Regardless of the preferred model, what is more relevant as part of the MVT ore system is the importance and strong evidence of the colloform texture for fluid mixing (Leach et al., 2005, 2010b; Wilkinson, 2014)). That fluid chemistry, as revealed in previous fluid-inclusion studies and also here, reflects a large range in fluid salinity (i.e. <1–30 weight per cent equiv. NaCl) supports mixing of different fluids during sphalerite mineralization is consistent with previous assertions that this is a critical factor for the development of colloform-banded ores. As for the source of the fluids in the study area, the absence of both magmatism and metamorphism coincident with mineralization precludes these fluid sources, which leaves surficial or meteoric fluids and basinal-brine fluids, which is discussed later.

Replacement textures are the most widespread and notable feature in the studied samples. Development of the carbonate types, from fine-grained crystalline dolostone to coarser types (medium-grained crystalline dolomite, coarse-grained crystalline dolomite, saddle dolomite; Fig. 4a, b), represents the coupling of dissolution and re-precipitation of carbonate minerals (e.g. Putnis, 2009). The fact that sphalerite precipitated in the later paragenetic stages and overlaps with formation of medium- and coarse-grained crystalline dolomite indicates that it also used the porosity generated due to dissolution of earlier carbonate minerals.

The common zonation from red-brown or light red-yellow to clearer sphalerite indicates a change in the geochemical state of the system (e.g. oxidation or sulfidation states). The sphalerite texture, regardless of colour, varies from fine to coarse grained and disseminated to pervasive, locally massive (Fig. 4c, 9c, d), in the carbonate host rocks; at a local scale, there can be nearly complete replacement of the host rock in places. It is apparent that mineralization can also be very selective, which might relate to certain rock fabrics; however, this was not determined in this study. The presence of disseminated sphalerite forming local haloes around coarse sphalerite observed with CL (Fig. 10a, c) provides evidence of the fine scale of the replacement process; in some cases, there was complete dissolution and development of cavities prior to sphalerite deposition (Fig. 4b). In many cases sphalerite extends into the matrix via tentacle-like features (Fig. 9c), which is further textural evidence that dissolution of dolostone occurred. Where massive fine-grained sphalerite occurs, very little relict original carbonate host rock remains (Fig. 8k, 9d).

Coarse-grained sphalerite is rarely seen coating the tops of carbonate minerals, a texture known as snow-on-roof and is not uncommon in MVT deposits where mineralization occludes cavities. Importantly, this texture it can be used to infer paleotop directions (e.g. Peace et al., 2003; Leach et al., 2010b), but the few occurrences and lack of oriented samples precluded such an application in this study.

Macro- and microscale observations suggest that the main ore-stage event is generally pre- and syn-formation of coarse-grained crystalline dolomite and saddle dolomite (see above); however, CL provides further relevant insight with respect to this process. In two of the samples examined, there is pervasive disseminated sphalerite in the fine-grained crystalline dolostone, which pre-dates the coarse-grained crystalline dolomite and saddle dolomite phases. Two interpretations are offered for the origin of this sphalerite: 1) it represents an earlier sphalerite mineralizing event commensurate with dolomitization of the marine carbonate minerals and is evidence for the protracted duration of the Zn-mineralizing event; or 2) it relates to ingress of the mineralizing fluids into the host rocks beyond where coarse sphalerite is associated with the coarse-grained crystalline dolomite and saddle dolomite, in which case it is part of the main sphalerite-forming event. The latter interpretation is favoured at present.

Carbonate mineral chemistry

Five carbonate mineral phases are distinguished based on petrographic study (Tables 2–4) and their chemistry is discussed here in the context of their paragenesis. The early dolomites are near stoichiometric, with the exception of some of the fine-grained crystalline dolostones, which have up to 1.4 weight per cent FeO (Table 9), a feature that may be attributed to ingress of a paragenetically later, Fe-rich fluid. This is supported by CL images showing the presence of disseminated sphalerite in this carbonate rock. This Fe enrichment is attributed to being synchronous with the modification of the original chemistry of the fine-grained crystalline dolostone through coupled dissolution-precipitation processes (Putnis, 2002, 2009). The coarse-grained crystalline dolomite phase is either free of Fe or bearing Fe and because it pre-dates the Fe-rich saddle dolomite phase, it may also record a modified signature post formation by interaction with a later fluid. More importantly, the presence of micro-inclusions of sphalerite, as indicated by elevated Zn contents for coarse-grained crystalline dolomite (to 1.2 weight per cent ZnO; Table 9) and CL images showing sphalerite inclusions, suggests a change in the fluid chemistry during the syn-ore stage of the paragenesis. The latest dolomite phase, the saddle dolomite, is the most Fe rich and in part forms a distinct chemical population (Fig. 11). This Fe enrichment is also reflected in the bright red CL images of the dolomite. The Fe-rich nature of this phase is most easily attributed to two processes: 1) the cessation of sphalerite precipitation, hence no competition for the available Fe in the fluid; and 2) the change in reduction-oxidation (redox) conditions so that sulfate is stabilized over sulfide, which terminates precipitation of Fe-bearing sulfide phases. Both of these processes would have resulted in preferential enrichment of Fe in the saddle dolomite. In deposits in which there is an abundance of late-stage pyrite, process 1 is more likely to have occurred.

Fluid inclusions

Two-phase (L + V) aqueous fluid inclusions in sphalerite give insight into the thermal and chemical characteristics of the fluids at the time of entrapment. Even though the inclusions for which thermometric data were collected vary in terms of entrapment classification (i.e. primary through secondary), it is assumed that they overlap with sphalerite precipitation and, hence, can be used to infer conditions of ore formation. This conclusion is supported by the fact that similar fluids are documented in many of the areas in the present study, and in MVT districts in general (Basuki and Spooner, 2004; Bodnar et al., 2014; Wilkinson, 2014).

The Th data, derived from both microthermometry and petrography, indicate that the lower temperatures (77–135ºC) are mostly confined to the Rocky Mountain deposits (except for one Shag sample at 187°C). These values generally equate to the more commonly reported Th data for fluid inclusions from phases coincident with MVT deposit formation (Basuki and Spooner, 2004; Leach et al., 2005; Bodnar et al., 2014). Assuming these fluids were in thermal equilibrium with the host rocks, this indicates depths of formation of approximately 2.5 to 4.5 km for a geotherm of 30°C; shallower depths would be expected if this assumption was invalid. Using the depth estimates and assuming lithostatic conditions, the pressure correction needed for these inclusions of approximately 30 bar/°C (Steele-MacInnis et al., 2012) gives trapping temperatures that range between 100 and 180°C (for Th ranging from 77–135°C); however, these latter values are considered a maximum because a component of hydrostatic pressure is likely in these settings.

Higher Th values of 145 to 214°C, which fall at the higher end of the range for MVT deposits and beyond the historical data summarized in Table 10, are seen in the Mastodon samples from the Kootenay Arc. These values are also much higher than the 121 to 140°C Th values for the O'Donnell samples, also in the Kootenay Arc. Again, assuming thermal equilibrium of the fluids and host rocks, estimates of depths of formation range from 5 to 7 km, and range to shallower depths if thermal equilibrium was not attained. The pressure correction for these Th values, similar to that for the Rocky Mountain samples, raises the temperature of formation to between 195 and 280°C, which is well beyond the range typical of MVT deposits (Leach et al., 2005; Bodnar et al., 2014; Wilkinson, 2014), but as noted above, these calculations assume lithostatic pressure only and some hydrostatic component is likely. These atypically high Th values for the Kootenay Arc deposits are more similar to data reported for the Irish-type MVT Zn-Pb deposits (e.g. Wilkinson, 2001, 2014) and may reflect a similarly high geothermal gradient. The presence of some chalcopyrite mineralization in the Kootenay Arc samples is consistent with the inferred higher formation temperatures.

The salinity data for sphalerite-hosted inclusions in the study areas range from less than 1 to 28 weight per cent equiv. NaCl ($\pm CaCl_2$), with ranges generally smaller for any

one setting, but still significant. Salinities (in weight per cent equiv. NaCl) range as follows: Robb Lake: 10 to 28, Monarch less than 1 to 21, and Mastodon 5 to 23; both O'Donnell (5–7) and Shag (21–22) have very narrow ranges. Although these data are generally similar to salinities measured in sphalerite from the study areas by previous workers (Table 1), none of the earlier work recorded salinities below approximately 7 weight per cent equiv. NaCl. Roedder (1968a) and Turner (2006) did, however, record lower salinities (approximately 1 weight per cent equiv. NaCl) for post-ore carbonate from the Pine Point deposit. Since no Pine Point data for sphalerite were obtained in the present study, we cannot further address the differences in the salinity data for this locality and our work; however, we can make a comparison for Monarch, where six inclusions gave salinities between 1 and 6 weight per cent equiv. NaCl, and another three measured approximately 20 weight per cent equiv. NaCl. This contrasts with the data for Monarch reported by Vandeginste et al. (2007), in which all 23 measured sphalerite-hosted inclusions had salinities exceeding 20 weight per cent; however, 19 of these inclusions came from a single sample. The low-salinity values recorded for Monarch contrast with the generalization that MVT fluids are of high salinity; although low salinities may occur in gangue phases it is a rare occurrence for sphalerite (Basuki and Spooner, 2004; Leach et al., 2005; Bodnar et al., 2014). Low salinities for fluid inclusions hosted in sphalerite (approximately 4 weight per cent NaCl) are reported in less than 0.5% of global data (n = 598; Bodnar et al., 2014).

Finally, the data in temperature-salinity space (Fig. 13) show a very broad trend toward lower salinity with increasing Th values, but we realize that more data are needed to verify this trend, thus any conclusions are tentative. This diagram simply highlights the variations discussed above, that being the large overall ranges in temperature and salinity, even in some cases for single settings (e.g. Monarch 0.9–20.2 weight per cent equiv. NaCl; Mastodon 3.1–23.1 weight per cent equiv. NaCl). These temperature-salinity ranges can only be accommodated by involving different fluids, the simplest model being dilution of a saline fluid by a less saline one. Furthermore, the low salinities of some deposits and occurrences, in particular Monarch, which falls below unmodified seawater (i.e. 3.2 weight per cent NaCl; Bischoff and Rosenbauer, 1985), suggests the local involvement of a low-salinity fluid, which must be meteoric water. As noted, further work is required to address the scatter of data and its implications, such as anion (Br, Cl; e.g. Wilkinson, 2014) and volatile gas (e.g. Jones and Kesler, 1992; Kontak, 1995) chemistry.

Isotopic data

Stable and radiogenic isotopes are used in the context of ore deposits to trace the possible source reservoirs for metals and anions (e.g. S) and also assess processes relevant to ore formation as revealed by site-specific changes in fluid conditions such as T, pH, or fO_2 (e.g. Ohmoto and Rye, 1979). We explore this aspect in the context of the analyzed samples from the deposits, but we also discuss the use of the more recently applied method of SIMS to such studies. Secondary ion mass spectrometry is particularly relevant where high-resolution understanding of the paragenesis is needed, such as for complex intergrowths of phases. The paragenesis of the different carbonate phases in this study (i.e. fine-grained crystalline dolostone to coarse-grained crystalline dolomite and saddle dolomite) is such an example.

Sulfur isotopes

The in situ $\delta^{34}S_{VCDT}$ measurements (Table 11) of single samples of sphalerite from each of four sites reveal that in each case the data are uniform: 1) $\delta^{34}S_{VCDT}$ = 23.6 to 24.9‰ for sphalerite from the Great Slave Reef, Pine Point district; 2) $\delta^{34}S_{VCDT}$ = 8.4 to 9.3‰ for sphalerite from the Reeves MacDonald deposit, Kootenay Arc; and 3) $\delta^{34}S_{VCDT}$ = 17.1 to 19.3‰ for sphalerite from the Robb Lake deposit, and $\delta^{34}S_{VCDT}$ = 29.4 to 33.2‰ for sphalerite, and $\delta^{34}S_{VCDT}$ = 29.3 to 31.4‰ for pyrite from the Kicking Horse deposit, both in the Rocky Mountain fold and thrust belt. In all of these settings, the data are close to, or just outside, the range of analytical variation; thus, in all cases isotopic homogeneity on the scale of mineral growth is retained. Isotopic homogeneity is particularly relevant because the sphalerites analyzed occlude cavities, and this indicates that a uniform value of $\delta^{34}S_{H2S}$ can be inferred regardless of how it was generated, as discussed below.

In the Kicking Horse deposit, both sphalerite and pyrite were analyzed, but only a single coarse domain of sphalerite was analyzed, whereas six small grains of matrix-hosted pyrite adjacent to the sphalerite grain were analyzed. For a temperature of formation of approximately 200°C we might expect the pyrite to have a $\delta^{34}S_{VCDT}$ value of approximately 2‰ more than sphalerite, based on their equilibrium fractionation (Ohmoto and Rye, 1979); however, the opposite is noted, with Δpyrite–sphalerite = –1.4‰ using the average measured $\delta^{34}S$ values. This suggests that there was a subtle change in some parameters between when these phases grew that affected their $\delta^{34}S$ values. Such detailed assessment of equilibrium and processes is only possible using the high spatial resolution offered by SIMS.

Whereas $\delta^{34}S_{VCDT}$ values for sulfide may be uniform within a mineral deposit (i.e. Δsulfide <5‰), there may be a large variation among sulfides between different MVT deposits and districts (i.e. Δsulfide to >40‰; Ohmoto and Rye, 1979; Leach et al., 2005). These differences in $\delta^{34}S_{sulfide}$ values reflect the ways sulfur can be reduced from its oxidized form, which involves either thermochemical sulfate reduction (TSR) or bacterial sulfate reduction (BSR). Where TSR dominates, the value of $\delta^{34}S_{H2S}$ produced can either be similar to the starting sulfate in the fluid or up to 10 to

15‰ less depending on the total or partial (i.e. distillation) reduction of sulfate, as discussed in detail by, for example, Wilkinson (2014) and Brueckner et al. (2015). In contrast, BSR generates much lower $\delta^{34}S_{H2S}$ values due to fractionation (i.e. tens of per mils) when sulfate is metabolized (see discussion in Seal, 2006). Thus, where the measured $\delta^{34}S_{sulfide}$ values are similar to the $\delta^{34}S_{VCDT}$ values of the inferred source evaporate, then TSR is suggested; when $\delta^{34}S_{sulfide}$ values are much less (e.g. by >20‰), BSR is the more likely mechanism (Leach et al., 2005; Seal, 2006; Wilkinson, 2014; Brueckner et al., 2015). Also relevant for interpreting the $\delta^{34}S_{sulfide}$ values is the secular variability of $\delta^{34}S$ for evaporitic sulfate (Farquhar et al., 2010). Thus, for the Great Slave Reef ($\delta^{34}S_{sphalerite} \approx 25‰$), which is similar to data for Pine Point orebodies ($\delta^{34}S_{sphalerite} \approx 21‰$; Sasaki and Krouse, 1969), and Kicking Horse deposits ($\delta^{34}S_{sphalerite, pyrite} \approx 31‰$), an evaporitic source coupled with an efficient TSR is considered the most likely means of producing reduced sulfur in these mineralized systems based on the geological settings (*see* Paradis et al., this volume). In contrast, for the Reeves MacDonald deposit ($\delta^{34}S_{sphalerite} \approx 9‰$), either partial TSR of sulfate occurred or there was mixing of TSR and BSR to produce sulfide in adequate proportions to generate the measured $\delta^{34}S$ values. Lastly, for Robb Lake ($\delta^{34}S_{sphalerite} \approx 18‰$), a partial TSR process (i.e. distillation where the proportion of sulfate reduced is approximately 70–80%) is considered to be the most likely means of generating sulfide (e.g. Brueckner et al., 2015).

Oxygen isotopes

The in situ SIMS $\delta^{18}O$ data (Table 11) provide the means to track the evolution of fluid-rock interactions from the early marine cementation stage (i.e. fine-grained crystalline dolostone), through the various coarser dolomites (medium-grained crystalline dolomite, coarse-grained crystalline dolomite, and saddle dolomite) and the late calcite occluding cavities. Given the temperature dependence of ^{18}O fractionation between carbonate minerals and fluid (Ohmoto, 1986), assumptions about constraining temperatures were made using fluid-inclusion microthermometric data from this study (Table 10) and earlier research (Table 1): 1) for samples from the Dawson oil field in the Peace River Arch, and Great Slave Reef samples, from the Pine Point district, we used a marine cementation (i.e. diagenesis) value of 40°C, hence less than 1 km burial, and 100°C for hydrothermal dolomite and post-ore calcite; 2) as there are no temperature constraints for Reeves MacDonald samples we instead used the upper Th value for the O'Donnell material (121–140°C; Table 4), which is from one of the many ore zones at Reeves MacDonald; and 3) for the Robb Lake and Kicking Horse deposits, we used Th values from Sangster and Carrière (1991) and Vandeginste et al. (2007) of 150 and 170°C, respectively, to constrain the upper limits. Because all of the above temperatures are based on Th, some degree of pressure correction must be added to account for lithostatic load, thus, these must be considered as minimum trapping temperatures.

Using the temperature constraints above and the $\delta^{18}O_{carbonate}$ data from the various settings, we constructed a plot of temperature (°C) versus $\delta^{18}O_{carbonate}$ with isopleths for $\delta^{18}O_{H2O}$ (Fig. 15). In general the plot shows that fine-grained crystalline dolostone records early marine dolomitization followed by development of coarser dolomite related to the infiltration of heated fluids during subsequent burial and formation of the various coarse dolomites and, lastly, post-ore calcite. The only data for the earliest stage of dolomite formation is for fine-grained crystalline dolostone from the Dawson oil field and Reeves MacDonald deposit, which either retained the original marine signature (i.e. typical value of marine cement; Lohmann and Walker, 1989) or records equilibration with seawater at a low temperature. The fine-grained crystalline dolostone is followed by the growth of coarse dolomite phases with much lower $\delta^{18}O$ values, which is typical for MVT-type settings (Leach et al., 2005), and reflects the interaction of the dolomites with warm fluids having variable $\delta^{18}O_{H2O}$ signatures from 4 to 16‰ (i.e. a basinal-type fluid; e.g. Wilkinson, 2014). These data are also the best estimate of the $\delta^{18}O$ signature of the Zn-Pb mineralizing fluids. The variable $\delta^{18}O$ signatures of these dolomites in part also reflect variable fluid-rock ratios, with those values furthest from the $\delta^{18}O$ of the fine-grained crystalline dolostone reflecting the greatest equilibration with the fluid (i.e. highest fluid-rock ratios). Thus, the data can be arranged in order of possible highest to lowest fluid-rock ratio as follows: Dawson oil field, Kicking Horse, and Robb Lake. In addition, because temperatures are loosely constrained in most cases, calculated $\delta^{18}O_{H2O}$ vary as temperature changes, which has the greatest effect at lower temperatures (i.e. <100°C) compared to higher temperatures as the $\delta^{18}O_{H2O}$ isopleths steepen (Fig. 15). Lastly, the cavity-filling calcite represents a much later fluid event, but again as the fluid reacts with the host, some influence of fluid-rock ratio might be expected. The calcite data for Reeves MacDonald have the highest inferred $\delta^{18}O_{H2O}$ value (6–12‰), which suggests, therefore, a greater host rock influence. In contrast, for Great Slave Reef and Dawson oil field, the calcite data reflect much lower $\delta^{18}O_{H2O}$ values and suggest a more fluid-dominated system.

By integrating petrography with in situ SIMS $\delta^{18}O$ data, it is possible to document the evolution of fluid-rock interactions. Because the replacement of fine-grained crystalline dolostone by coarse-grained crystalline and saddle dolomite occurred via a progressive coupled dissolution-precipitation process (e.g. Putnis, 2002), it is to be expected that there will be a range of $\delta^{18}O$ values recorded by these phases, increasing toward that of the fluid at higher fluid-rock ratios, as recorded in progressively altered rocks. The variation within the data presented here for the different hydrothermal dolomite phases reflects the known variables: the temperature, fluid-rock ratio, and $\delta^{18}O$ signatures of the reacting fluid and

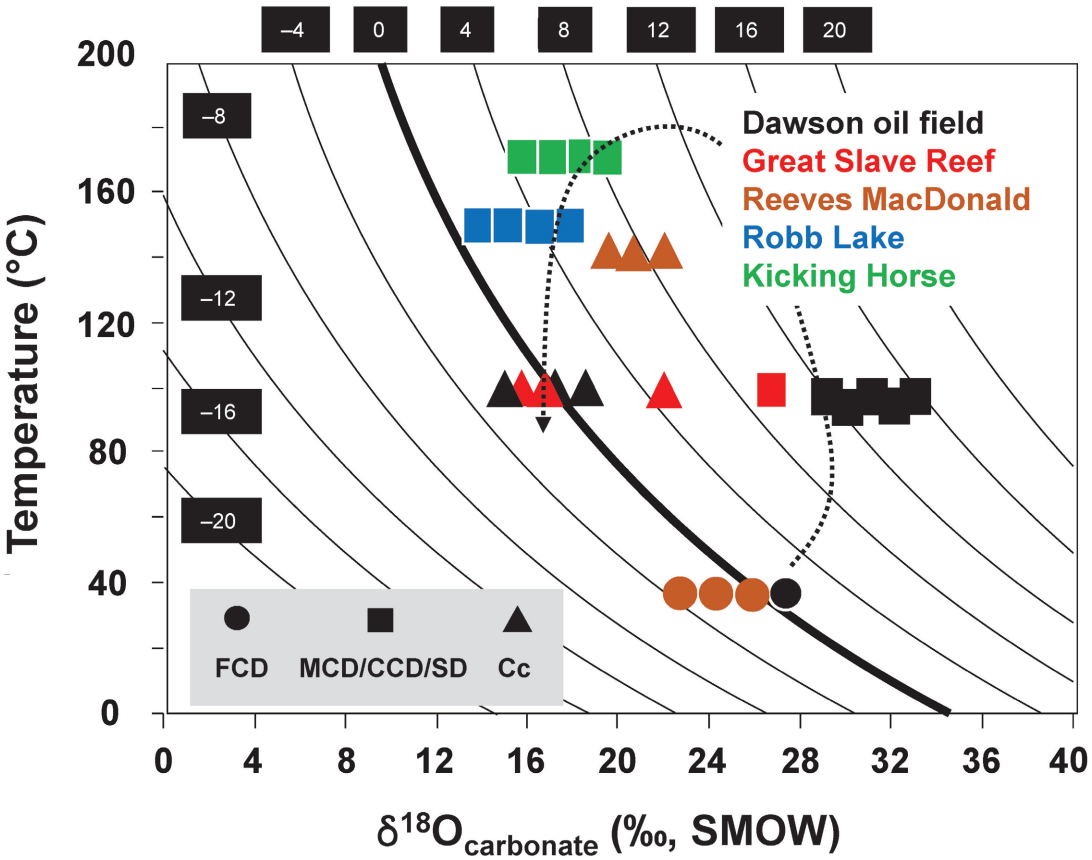

Figure 15. Plot of $\delta^{18}O_{carbonate}$ (‰;VSMOW) values for different carbonate mineral types versus estimated temperatures of formation The curved lines are isopleths of $\delta^{18}O_{H2O}$ values (indicated by the black boxes) of precipitating fluids calculated using the dolomite-H_2O fractionation equation of Horita (2014). Data are colour coded by setting and symbols denote the type of carbonate mineral analyzed. Because the secondary ion mass spectrometry $\delta^{18}O$ data for each phase analyzed was uniform (i.e. ±1–2‰), average values are plotted for grains and, hence, fewer points are shown than analyses in Table 5. Because the difference in the calcite-H_2O fractionation (compared to dolomite-H_2O) is not significant (i.e. only 2‰ at 100°C; Horita, 2014), the isopleths for dolomite-H_2O fractionation are used for all data. The dashed black line traces the idealized evolutionary trend of a fluid in a Mississippi Valley–type setting. Abbreviations: Cc: calcite; CCD: coarse-grained crystalline dolomite; FCD: fine-grained crystalline dolostone; MCD: medium-grained crystalline dolomite; SD: saddle dolomite.

rock (Taylor, 1977). This is relevant in the context of the present study because the reacting fluid is the one responsible for the Zn-Pb mineralization; hence, the most abundant and highest grades of mineralization would be expected to coincide with areas of greatest fluid-rock interaction as the system equilibrated toward the ingressing mineralizing fluid. The application of the $\delta^{18}O$ signature of the syn-ore carbonate minerals to determine the degree of fluid-rock interaction as an indication of potential for mineralization in carbonate replacement deposits has been discussed for both MVT settings (Savard et al., 2000) and Carlin-type gold deposits (Barker et al., 2013).

In summary, we show in Figure 15 an idealized evolution (*see* black dashed line) of a fluid in a MVT setting such as those studied here. The initial dolomite (fine-grained crystalline dolostone), reflects the interaction of the host carbonate rocks with heated seawater during shallow burial. As burial continues, there is a gradual shift toward lower $\delta^{18}O_{carbonate}$ values as the fluid is heated and $\Delta_{carbonate\text{-}H2O}$ decreases; this is also due to mixing with a fluid characterized by a higher $\delta^{18}O$ signature. Variation in temperature and $\delta^{18}O_{H2O}$ can lead to a range in the final $\delta^{18}O_{carbonate}$ values, as is evident in the data for Robb Lake and Kicking Horse. The last part of the loop, which is generally recorded as a late-stage post-ore calcite, reflects the combined effects of cooling and ingress of a fluid with a lower $\delta^{18}O$ value.

SUMMARY AND CONCLUSIONS

A detailed petrographic, geochemical (SEM-EDS, CL), and in situ SIMS isotopic (O, S) study of a suite of samples from three MVT districts across the eastern Canadian Cordillera (i.e. the Rocky Mountains foreland belt, the Kootenay Arc, and the Western Canadian Sedimentary Basin) through British Columbia, northern Alberta, and southwest Northwest Territories was conducted using archived samples. The study is the first geographically comprehensive examination of such materials as part of a single study and, therefore, provides the means to compare and contrast materials.

In all three districts, initial widespread dolomitization of marine carbonate rocks was followed by different stages of hydrothermal dolomite formation (e.g. medium- to coarse-grained crystalline and saddle dolomites) and sulfide deposition, mainly sphalerite, galena, and pyrite, and subsequent cavity- and fracture-filling carbonate minerals. This widespread and generally common paragenesis is consistent with that noted previously (e.g. Kyle, 1981; Qing, 1991; Paradis et al., 2006, 2015; Turner, 2006; Vandeginste et al., 2007); however, we do note that at any one site there may be some differences. The sphalerite mineralization is divided into two stages: an early light to dark red-brown transitioning through zoning to a pale, honey-yellow variety; additionally, late-stage colloform or banded textures are noted for some sites where sphalerite occludes remaining open space. Galena is paragenetically later, cuts sphalerite, and also occludes cavities to locally form a coarse cubic variety.

The conditions attending ore formation are constrained by studying sphalerite-hosted fluid inclusions. Despite challenges, in particular the opacity of the inclusions, sufficient data were generated to make preliminary conclusions for Th and fluid salinities. For samples from the Rocky Mountain fold and thrust belt, fluids have a lower temperature (Th = 77–135°C; trapping temperatures of 100–180°C) than those of the Kootenay Arc (Th = 145–214°C; trapping temperatures of 195–280°C). Whereas the former range extends to the higher end typical for MVT mineralization globally, the latter range falls well above this, but within the temperature range of Irish-type MVT deposits (e.g. Wilkinson, 2014). Salinities of the mineralizing fluids range overall from 1 to 28 weight per cent equiv. NaCl ($\pm CaCl_2$), but with narrower ranges for individual deposits. The variation among MVT districts for both the temperature and salinity of the mineralizing fluids suggests different fluid reservoirs, which best equate to basinal-type fluids and surficial or meteoric fluids. Our results also indicate a lack of dissolved volatile species (COH) in the studied samples and, in addition, the lack of fluorescence of inclusions under UV light precludes the presence of liquid petroleum; however, the local presence of bitumen (e.g. Great Slave Lake, Pine Point district, Western Canadian Sedimentary Basin (Rhodes et al., 1984) and Munroe and Shag, Canadian Rocky Mountains) does indicate that liquid petroleum flowed through these systems at one time.

Four distinct textural varieties of dolomite of similar paragenesis occur in all the MVT districts studied. The early fine-grained crystalline dolostone and medium-grained crystalline dolomite are generally Fe poor, but later coarse-grained crystalline dolomite contains Fe and (locally) Zn, present as micro-inclusions of sphalerite, and thus consistent with coarse-grained crystalline dolomite overlapping the mineralization. The saddle dolomite is the most Fe rich, syn- to post-sphalerite, and the latest dolomite to precipitate. Cathodoluminescence observations of four samples indicate that the ingress of the Zn (±Pb) mineralizing fluid was more pervasive than petrographic observations suggest, based on the presence of disseminated sphalerite within the early carbonate phases (fine-grained crystalline dolostone, medium-grained crystalline dolomite). Thus, our data show that the paragenesis and fluid (migration) histories in MVT systems may (in some deposits or districts) be more complex than generally considered.

In situ SIMS measurements of $\delta^{34}S_{VCDT}$ (sphalerite, pyrite) and $\delta^{18}O_{SMOW}$ (carbonate minerals) on select samples from different districts and/or deposits (Dawson oil field, Great Slave Reef (Pine Point district), Reeves MacDonald, Robb Lake, Kicking Horse) across the study areas were used to assess the use of this method where conventional bulk-type analysis had been done before. Results are comparable to previous data, where available, and indicate isotopic homogeneity at a micron scale. The $\delta^{34}S_{VCDT}$ data confirm previous conclusions that invoke an evaporitic source for sulfur and that TSR was the dominant processes to generate the reduced sulfur species in the precipitated sulfide phases. The $\delta^{34}S_{VCDT}$ data indicate a possible contribution by BSR processes in only one deposit studied (i.e. Reeves MacDonald). The fact that the $\delta^{34}S$ data favour TSR processes to generate reduced sulfide species suggests that a H_2S-bearing fluid was likely at the sites of mineralization prior to ingress of the metal-bearing fluid, or their fluid-flow paths intersected there. The $\delta^{18}O_{SMOW}$ data record the evolution of fluid-rock interactions to form the early fine-grained crystalline dolostone, later coarser hydrothermal dolomites during burial, and, finally, late calcite. The signatures of these carbonate phases reflect variable rock and fluid $\delta^{18}O_{SMOW}$ values (i.e. reservoirs), different temperatures, and different fluid-rock ratios.

Collectively, the data sets imply that at least three fluids are responsible for the observed chemical signature of the mineralized sites: the fluid-inclusion studies require at least two (if not more) fluid reservoirs and the $\delta^{34}S_{VCDT}$ data indicate that TSR was the dominant process to generate reduced sulfide, which indicates that metals were transported by another fluid that was low in sulfur. As with previous formation models suggested for MVT deposits (Leach et al., 2005, 2010a, b; Wilkinson, 2014), we favour the two-fluid mixing model because TSR is a relatively slow process, thus, the most efficient process is to have a ready supply of sulfur at the site where mineralization is formed. The two-fluid mixing model is also favoured by the presence of colloform-textured sphalerite at many of the study

sites. Lastly, the $\delta^{18}O_{SMOW}$ data are consistent with multiple fluid reservoirs, including a surficial or meteoric water fluid reservoir.

Future work and outstanding questions

The lack of a complete, well-constrained record of fluid-rock interactions provided via isotopes and fluid inclusions for both this and previous studies severely limits interpretation of the record of fluid ingress and its reaction with the host rocks in the MVT deposits examined here. Furthermore, as noted for the data for the Kicking Horse and Monarch deposits, the fact that earlier work was not done using a modern protocol (i.e. FIA approach) hinders interpretation of these data, and our further examination of the results of others (e.g. Qing, 1991; Qing and Mountjoy, 1992, 1994), although not discussed herein, suggests the same applies. To address this issue, we suggest that a different approach be adopted, as has been presented elsewhere (Mathieu et al., 2015, 2018, 2019; Hahn et al., 2018), whereby a fully integrated study involves detailed petrographic examination complemented with SEM-EDS mapping and CL imaging, fluid-inclusion microthermometry following FIA protocol, in situ laser-ablation inductively coupled plasma mass spectrometry analysis of gangue (carbonate minerals, quartz), and in situ SIMS isotopic analysis of gangue (carbonate minerals, quartz) and sulfide minerals (sphalerite, pyrite). Our preliminary work on SIMS $\delta^{18}O_{carbonate}$ illustrates the application of this approach. The power of this protocol is that varied methods are in part complementary, so that the lack of one set of data does not preclude interpretation of an event. For example: 1) redox-sensitive trace-element data (Fe, Mn, Ce, Eu) reflect changing fluid chemistry; 2) ΣREE+Y chemistry reflects changes in fluid types and mixing/dilution with/by meteoric water; and 3) Eu* and Ce* anomalies are also proxies for fluid chemistry, as is $\delta^{18}O$ and calculated $\delta^{18}O_{H_2O}$. We are currently conducting such work on the samples used in the present study.

Two applications of the suggested protocol that address important outstanding aspects of MVT deposits are noted. First, where salinity data cannot be obtained, the other proxies allow inference of fluid type, which was previously not possible; hence, if low-salinity fluids deposited carbonate minerals but fluid inclusions are lacking or metastable during freezing, then both ΣREE+Y and in situ $\delta^{18}O$ may provide evidence of such a fluid. Second, where temperature of formation is lacking (due to absence or modification of fluid inclusions, or inclusions that are too difficult to measure), then the $\delta^{18}O$ signature can be used to estimate temperature, as noted in this study.

ACKNOWLEDGMENTS

This paper is a contribution to Natural Resource Canada's Targeted Geoscience Initiative program (TGI-5). Support for this study was provided through the Volcanic- and Sedimentary-hosted Base Metal Mineralization project's 'Activity VS-2.1: Is there a genetic link between various types of sediment-hosted deposits of the Canadian Cordillera?'.

The component of the work done at Laurentian University (Sudbury) used the Hydrothermal Fluid Laboratory and was supported through a NSERC RTI grant to D. Kontak, and the SIMS analysis at the University of Manitoba is supported by NSERC grants to M. Fayek. The authors thank R. Sharpe at the University of Manitoba (Winnipeg) for assistance with SIMS analyses and W. Zhi and R. Poulin at Laurentian University for assistance with the SEM-EDS and CL work, respectively. This study benefited from the field assistance and collaboration of Fiona Katay (British Columbia Ministry of Energy, Mines and Petroleum Resources, Regional Geologist based in Cranbrook). Chris Graf kindly provided samples from the Shag deposit. We would particularly like to thank J. Peter, M. Gadd, and G. Chi for their very careful reviews, which resulted in substantial improvements and clarification of our thoughts.

REFERENCES

Adams, J.J., Rostron, B.J., and Mendoza, C.A., 2000. Evidence for two-fluid mixing at Pine Point, NWT; Journal of Geochemical Exploration, v. 69–70, p. 103–108. https://doi.org/10.1016/S0375-6742(00)00014-5

Atkinson, N. and Lyster, S., 2000. Thickness of Quaternary and Neogene sediment in Alberta, Canada; Energy Resources Conservation Board, ERCB/AGS MAP 551, scale 1:1 500 000.

Barker, S.L.L, Dipple, E.G.M., Hickey, K.A., Lepore, W.A., and Vaughn, V., 2013. Applying stable isotopes to mineral exploration: teaching an old dog new tricks; Economic Geology, v. 108, no. 1, p. 1–9. https://doi.org/10.2113/econgeo.108.1.1

Barrie, C.D., Boyce, A.J., Boyle, A.P., Williams, P.J., Blake, K., Lowther, J.M., McDermott, P., Wilkinson, J.J., and Prior, D.J., 2009. On the growth of colloform textures: a case study of sphalerite from the Galmoy ore body, Ireland; Geological Society of London, Journal, v. 166, no. 3, p. 463–483. https://doi.org/10.1144/0016-76492008-080

Basuki, N.I. and Spooner, E.T.C., 2004. A review of fluid inclusion temperatures and salinities in Mississippi Valley-type Zn-Pb deposits: identifying thresholds for metal transport; Exploration and Mining Geology, v. 11, no. 1–4, p. 1−17. https://doi.org/10.2113/11.1-4.1

Bodnar, R.J., 1993. Revised equation and table for determining the freezing point depression of H2O-NaCl solutions; Geochimica et Cosmochimica Acta, v. 57, no. 3, p. 683–684. https://doi.org/10.1016/0016-7037(93)90378-A

Bodnar, R.J., 2003a. Introduction to fluid inclusions; *in* Fluid inclusions: analysis and interpretation, (ed.) I.M. Samson, A.J. Anderson, and D. Marshall; Mineralogical Association of Canada, Short Course Series, v. 32, p. 1–8.

Bodnar, R.J., 2003b. Re-equilibration of fluid inclusions; *in* Fluid inclusions: analysis and interpretation, (ed.) I.M. Samson, A.J. Anderson, and D. Marshall; Mineralogical Association of Canada, Short Course Series, v. 32, p. 213–230.

Bodnar, R.J., Reynolds, T.J., and Kuehn, C.A., 1985. Fluid-inclusion systematics in epithermal systems; Reviews in Economic Geology, v. 2, p. 73–97. https://doi.org/10.5382/Rev.02.05

Bodnar, R.J., Lecumberri-Sanchez, P., Moncada, D., and Steele-MacInnis, M., 2014. Fluid inclusions in hydrothermal ore deposits; Chapter 5 *in* Volume 13: Geochemistry of mineral deposits; Treatise on geochemistry, 2nd edition, (ed.) S.D. Scott; Elsevier, Oxford, United Kingdom, p. 119–142. https://doi.org/10.1016/B978-0-08-095975-7.01105-0

Boyce, A.J., Barrie, C.D., Samon, I.M., and Williams-Jones, A.E., 2015. Aspects of the geochemistry of zinc – a journey to sphalerite; *in* Current perspectives on zinc deposits, (ed.) S.M. Archibald and S.J. Piercey; Irish Association for Economic Geology, Dublin, Ireland, p. 17–35.

Bischoff, J.L., and Rosenbauer, R.J., 1985. An empirical equation of state for hydrothermal seawater (3.2 percent NaCl); American Journal of Science, v. 285, no. 8, p. 725–763. https://doi.org/10.2475/ajs.285.8.725

Brueckner, S.M., Piercey, S.J., Layne, G.D., Piercey, G., and Sylvester, P.J., 2015. Variations of sulfur isotope signatures in sulfides from the metamorphosed Ming Cu(−Au) volcanogenic massive sulphide deposit, Newfoundland Appalachians, Canada; Mineralium Deposita, v. 50, p. 619–640. https://doi.org/10.1007/s00126-014-0567-7

Burchfiel, B.C. and Davis, G.A., 1972. Structural framework and evolution of the Southern part of the Cordilleran Orogen, western United States; American Journal of Science, v. 272, no. 2, p. 97–118. https://doi.org/10.2475/ajs.272.2.97

Cant, D.J., 1988. Regional structure and development of the Peace River Arch, Alberta: a Paleozoic failed-rift system?; Bulletin of Canadian Petroleum Geology, v. 36, no. 3, p. 284–295. https://doi.org/10.35767/gscpgbull.36.3.284

Carrière, J.J. and Sangster, D.F., 1999. A multidisciplinary study of carbonate-hosted zinc-lead mineralization in the MacKenzie platform (a.k.a. Blackwater and Lac de Bois platforms), Yukon and Northwest Territories, Canada; Geological Survey of Canada, Open File 3700, 145 p. https://doi.org/10.4095/210821

Coniglio, M., Morrow, D.W., and Wilson, N., 2006. Reassessment of Middle Devonian dolomites, Presqu'ile barrier, Northwest Territories; *in* Potential for carbonate-hosted lead-zinc Mississippi Valley-type mineralization in Northern Alberta and Southern Northwest Territories: Geoscience Contributions, Targeted Geoscience Initiative, (ed.) P.K. Hannigan; Geological Survey of Canada, Bulletin 591, p. 195–219. https://doi.org/10.4095/222937

Diamond, L.W., 1992. Stability of CO_2-clathrate-hydrate + CO_2 liquid + CO_2 vapour + aqueous KCl–NaCl solutions: experimental determination and application to salinity estimates of fluid inclusions; Geochimica et Cosmochimica Acta, v. 56, no. 1, p. 273–280. https://doi.org/10.1016/0016-7037(92)90132-3

Drage, N. and Paradis, S., 2018. Geology and petrography of selected carbonate-hosted Zn-Pb deposits of the southeastern Cordillera, British Columbia and Alberta; Geological Survey of Canada, Open File 8410, 27 p. https://doi.org/10.4095/311220

Fall, A. and Bodnar, R.J., 2018. How precisely can the temperature of a fluid event be constrained using fluid inclusions?; Economic Geology, v. 113, no. 8, p. 1817–1843. https://doi.org/10.5382/econgeo.2018.4614

Farquhar, J., Wu, N.P., Canfield, D.E., and Oduro, H., 2010. Connections between sulfur cycle evolution, sulfur isotopes, sediments, and base metal VMS, SEDEX, and MVT deposits; Economic Geology, v. 105, p. 509–533. https://doi.org/10.2113/gsecongeo.105.3.509

Fowler, A., and L'Heureux, I., 1996. Self-organized banded sphalerite and branching galena in the Pine Point ore deposit, Northwest Territories; The Canadian Mineralogist, v. 34, no. 6, p. 1211–1222.

Fyles, J. T., 1964. Geology of the Duncan Lake area, Lardeau district, British Columbia; British Columbia Ministry of Energy and Mines, British Columbia Geological Survey, Bulletin 49, 87 p.

Fyles, J.T. and Hewlett, C.G., 1959. Stratigraphy and structure of the Salmo lead-zinc area; British Columbia Ministry of Energy and Mines, British Columbia Geological Survey, Bulletin 41, 162 p.

Gleeson, S.A. and Turner, W.A., 2007. Fluid inclusion constraints on the origin of the brines responsible for Pb–Zn mineralization at Pine Point and coarse non-saddle and saddle dolomite formation in southern Northwest Territories; Geofluids, v. 7, no. 1, p. 51–68. https://doi.org/10.1111/j.1468-8123.2006.00160.x

Götze, J., 2012. Application of cathodoluminescence microscopy and spectroscopy in geosciences; Microscopy and Microanalysis, v. 18, p. 1270–1284. https://doi.org/10.1017/S1431927612001122

Götze, J., Hans-Peter Schertl, H.-P., Neuser, R.D., and Kempe, U., and Hanchar, H.M., 2013. Optical microscope-cathodoluminescence (OM–CL) imaging as a powerful tool to reveal internal textures of minerals; Mineralogy and Petrology, v. 107, p. 373–392. https://doi.org/10.1007/s00710-012-0256-0

Goldstein, R.H. and Reynolds, T.J., 1994. Systematics of fluid inclusions in diagenetic minerals; Society for Sedimentary Geology, Short Course No. 31, 199 p. https://doi.org/10.2110/scn.94.31

Hahn, K.E., Turner, E.C., Kontak, D.J., and Fayek, M., 2018. Fluid-chemical evidence for one billion years of fluid flow through Mesoproterozoic deep-water carbonate mounds (Nanisivik zinc district, Nunavut); Geochimica et Cosmochimica Acta, v. 223, p. 493–519. https://doi.org/10.1016/j.gca.2017.12.001

Hannigan, P.K., 2006. Synthesis of Mississippi Valley-type lead-zinc deposit potential in northern Alberta and southern Northwest Territories; *in* Potential for carbonate-hosted lead-zinc Mississippi Valley-type mineralization in northern Alberta and southern Northwest Territories: Geoscience Contributions, Targeted Geoscience Initiative, (ed.) P.K. Hannigan; Geological Survey of Canada, Bulletin 591, p. 305–347. https://doi.org/10.4095/222945

Henley, R.W. and Hughes, G.O., 2000. Underground fumaroles: "excess heat" effects in vein formation; Economic Geology, v. 95, no. 3, p. 453–466. https://doi.org/10.2113/gsecongeo.95.3.453

Horita, J., 2014.Oxygen and carbon isotope fractionation in the system dolomite-water-CO_2 to elevated temperatures; Geochimica et Cosmochimica Acta, v. 129, p. 111–124. https://doi.org/10.1016/j.gca.2013.12.027

Höy, T., 1982. Stratigraphic and structural setting of stratabound lead-zinc deposits in southeastern British Columbia; CIM Bulletin, v. 75, p. 114–134.

Jones, H.D. and Kesler, S.E., 1992. Fluid inclusion gas chemistry in East Tennessee Mississippi Valley-type districts: evidence for immiscibility and implications for deposition mechanisms; Geochimica et Cosmochimica Acta, v. 56, p. 137–154. https://doi.org/10.1016/0016-7037(92)90122-Y

Klyukina, Y.L., Steele-MacInnis, M., Lecumberri-Sancheza, P., and Bodnar, R.J. 2019. Fluid inclusion phase ratios, compositions and densities from ambient temperature to homogenization, based on PVTX properties of H2O-NaCl; Earth-Science Reviews, v. 198, 102924. https://doi.org/10.1016/j.earscirev.2019.102924

Kontak, D.J., 1995. A study of fluid inclusions in sulfide and nonsulfide mineral phases from a carbonate-hosted Zn-Pb deposit, Gays River, Nova Scotia, Canada; Economic Geology, v. 93, p. 793–817. https://doi.org/10.2113/gsecongeo.93.6.793

Kontak, D.J., Kyser, K., Gize, A. and Marshall, D., 2006, structurally controlled vein barite mineralization, Maritimes Basin of Eastern Canada: geological setting, stable isotopes and fluid inclusions; Economic Geology, v. 101, p. 407–430. https://doi.org/10.2113/gsecongeo.101.2.407

Krebs, W., and Macqueen, R., 1984. Sequence of diagenetic and mineralization events, Pine Point lead-zinc property, Northwest Territories; Canada; Bulletin of Canadian Petroleum Geology, v. 32, p. 434–464. https://doi.org/10.35767/gscpgbull.32.1.027

Kyle, J.R., 1981. Geology of the Pine Point lead–zinc district; Chapter 11 *in* Volume 9, Regional and specific deposits, 1st edition; Handbook of strata-bound and strataform ore deposits, (ed.) K.H. Wolf; Elsevier, New York, U.S.A., v. 9, p. 643–741.

Leach, D.L., and Sangster, D.F., 1993. Mississippi Valley-type lead-zinc deposits; *in* Mineral deposit modelling, (ed.) R.V. Kirkham; Geological Association of Canada, Special Paper 40, p. 289–314.

Leach, D.L., Sangster, D.F., Kelley, K.D., Large, R.R., Garven, G., Allen, C.R., Gutzmer, J., and Walters, S., 2005. Sediment-hosted lead-zinc deposits: a global perspective; *in* Economic Geology, 100th anniversary volume, 1905–2005, (ed.) J.W. Hedenquist, J.F.H. Thompson, R.J. Goldfarb, and J.P. Richards; Society of Economic Geologists, Littleton, Colorado, p. 561–607. https://doi.org/10.5382/AV100.18

Leach, D.L., Bradley, D.C., Huston, D., Pisarevsky, S.P., Taylor, R.D., and Garoll, S.J., 2010a. Sediment-hosted lead-zinc deposits in Earth history; Economic Geology, v. 105, no. 3, p. 593–625. https://doi.org/10.2113/gsecongeo.105.3.593

Leach, D.L., Taylor, R.D., Fey, D.L., Diehl, S.F., and Saltus, R.W., 2010b. A deposit model for Mississippi Valley-Type lead-zinc ores. Chapter A of Mineral Deposit Models for Resource Assessment; U.S. Geological Survey Scientific Investigations Report 2010–5070–A, 52 p.

Logan, J.M., and Colpron, M. 2006, Stratigraphy, geochemistry, syngenetic sulfide occurrences and tectonic setting of the lower Paleozoic Lardeau Group, northern Selkirk Mountains, British Columbia; Geological Association of Canada, Special Paper 45, p. 361–382.

Lohmann, K.C., and Walker, J.C.G., 1989. The $\delta^{18}O$ record of Phanerozoic Abiotic marine calcite cement; Geophysical Research Letters, v. 16, p. 319–322. https://doi.org/10.1029/GL016i004p00319

Macqueen, R.W. and Thompson, R.I., 1978. Carbonate-hosted zinc-lead occurrences in northeastern British Columbia with emphasis on the Robb Lake deposit; Canadian Journal of Earth Sciences, v. 15, no. 11, p. 1737–1762. https://doi.org/10.1139/e78-183

Mathieu, J., Turner, E.C., Kontak, D.J., Fayek, M., and Layne, G., 2015. In situ SIMS (O, S) and LA ICP-MS (trace elements) micro-analysis of multiple cement phases reveal a complex diagenetic fluid history: A case study of Phanerozoic cements on Victoria Island, NWT; Chemical Geology, v. 415, p. 47–69. https://doi.org/10.1016/j.chemgeo.2015.08.016

Mathieu, J., Turner, E.C., Kontak, D.J., Fayek, M., and Mathur, R., 2018. Atypical Cu mineralization in the Cornwallis carbonate-hosted Zn district: Storm copper deposit in the Cornwallis, Arctic Canada; Ore Geology Reviews, v. 99, p. 86–115. https://doi.org/10.1016/j.oregeorev.2018.06.009

Mathieu, J., Turner, E.C., Kontak, D.J., and Fayek, M., 2019. Fluid histories and controlling factors on mineralization in the Cornwallis Zn-Pb district, Arctic, Canada; SGA Meeting, Glasgow, Scotland. Program and extended abstracts, v. 3, p. 1264–1267.

Meyers, W.J., 1974. Carbonate cement stratigraphy of the Lake Valley Formation (Mississippian) Sacramento Mountains, New Mexico; Journal of Sedimentary Research, v. 44, no. 3, p. 837–861. https://doi.org/10.1306/212F6BC2-2B24-11D7-8648000102C1865D

McLemore, V.T. and Barker, J.M., 1987. Some geological application of cathodoluminescence: examples from the Lemitar Mountains and Riley travertine, Socorro County, New Mexico; New Mexico Geology, May issue, p. 37–40.

McMechan, M.E., 2012. Deep transverse basement structural control of mineral systems in the southeastern Canadian Cordillera; Canadian Journal of Earth Sciences, v. 49, no. 5, p. 693–708. https://doi.org/10.1139/e2012-013

Moncada, D., Mutchler, S., Nieto, A., Reynolds, T.J., Rimstidt, J.D., and Bodnar, R.J., 2012. Mineral textures and fluid inclusion petrography of the epithermal Ag–Au deposits at Guanajuato, Mexico: application to exploration; Journal of Geochemical Exploration, v. 114, p. 20–35. https://doi.org/10.1016/j.gexplo.2011.12.001

Nelson, J., Paradis, S., and Zantvoort, W., 1999. The Robb Lake carbonate-hosted lead-zinc deposit, northeastern British Columbia: a Cordilleran MVT deposit; *in* Geological Fieldwork 1998; British Columbia Ministry of Energy and Mines, British Columbia Geological Survey, Paper 1999-1, pages 89–102.

Nelson, J., Zantvoort, W., and Paradis, S., 2000. Geology of the Robb Lake Pb-Zn deposit, northeastern B.C.; British Columbia Ministry of Energy, Mines and Petroleum Resources, British Columbia Geological Survey, Open File 2000-3, scale 1:20 000.

Nelson, J., Paradis, S., Christensen, J., and Gabites, J., 2002. Canadian Cordilleran Mississippi Valley-type deposits: A case for Devonian-Mississippian back-arc hydrothermal origin; Economic Geology, v. 97, no. 5, p. 1013–1036. https://doi.org/10.2113/gsecongeo.97.5.1013

Nesbitt, B.E. and Muehlenbachs, K., 1994. Paleohydrogeology of the Canadian Rockies and origins of brines, Pb-Zn deposits and dolomitization in the Western Canada Sedimentary Basin; Geology, v. 22, no. 3, p. 243–246. https://doi.org/10.1130/0091-7613(1994)022%3C0243:POTCRA%3E2.3.CO;2

O'Connell, S., Dix, G.R., and Barclay, J.E., 1990. The origin, history, and regional structural development of the Peace River Arch, Western Canada; Bulletin of Canadian Petroleum Geology, v. 38A, p. 4–24. https://doi.org/10.35767/gscpgbull.38a.1.004

Ohmoto, H., 1986, Stable isotope geochemistry of ore deposits; *in* Stable isotopes in high-temperature geological processes, (ed.) J.W. Valley, H.P. Taylor, Jr., and J.R. O'Neil; Mineralogical Association of America, Reviews in Mineralogy, v. 16, p. 185–225.

Ohmoto, H., and Rye, R.O., 1979. Isotopes of sulfur and carbon; in Geochemistry of hydrothermal ore deposits, 2nd edition, (ed.) H. Barnes; John Wiley and Sons, New York, p. 509–567.

Pană, D., 2006. Unravelling the structural control of Mississippi Valley-type deposits and prospects in carbonate sequences of the Western Canada Sedimentary Basin; *in* Potential for carbonate-hosted lead-zinc Mississippi Valley-type Mineralization in northern Alberta and southern Northwest Territories: geoscience contributions, Targeted Geoscience Initiative, (ed.) P.K. Hannigan; Geological Survey of Canada, Bulletin 591, p. 255–304. https://doi.org/10.4095/222944

Paradis, S., 2007. Carbonate-hosted Zn-Pb deposits in southern British Columbia: potential for Irish-type deposits; Geological Survey of Canada, Current Research 2007-A10, 10 p. https://doi.org/10.4095/224161

Paradis, S. and Nelson, J.L., 2007. Metallogeny of the Robb Lake carbonate-hosted zinc-lead district, northeastern British Columbia; *in* Mineral deposits of Canada: a synthesis of major deposit types, district metallogeny, the evolution of geological provinces, and exploration methods, (ed.) W.D. Goodfellow; Geological Association of Canada, Mineral Deposits Division, Special Publication No. 5, p. 633–654.

Paradis, S. and Simandl, G.J., 2017. Is there a genetic link between the SEDEX and MVT deposits of the Canadian Cordillera?; *in* Targeted Geoscience Initiative: 2016 report of activities, (ed.) N. Rogers; Geological Survey of Canada, Open File 8199, p. 107–113. https://doi.org/10.4095/299623

Paradis, S. and Simandl, G.J., 2019. Preliminary carbon and oxygen isotope analyses of hydrothermal carbonate from Mississippi Valley-type and REE-F-Ba deposits of the southern Canadian Rocky Mountains – a comparison; *in* Targeted Geoscience Initiative: 2018 report of activities, (ed.) N. Rogers; Geological Survey of Canada, Open File 8549, p. 205–216. https://doi.org/10.4095/313652

Paradis, S., Nelson, J.L., and Zantvoort, W., 1999. A new look at the Robb Lake carbonate-hosted lead-zinc deposit, northeastern British Columbia; Geological Survey of Canada, Current Research 1999-A, p. 61–70. https://doi.org/10.4095/210143

Paradis, S., Turner, W.A., Coniglio, M., Wilson, N., and Nelson, J.L., 2006. Stable and radiogenic isotopic signatures of mineralized Devonian carbonate rocks of the northern Rocky Mountains and the Western Canada Sedimentary Basin; *in* Potential for carbonate-hosted lead-zinc Mississippi Valley-type mineralization in northern Alberta and southern Northwest Territories: geoscience contributions, Targeted Geoscience Initiative, (ed.) P.K. Hanningan;, Geological Survey of Canada, Bulletin 591, p. 75–103. https://doi.org/10.4095/222922

Paradis, S., Hannigan, P., and Dewing, K., 2007. Mississippi Valley-type lead-zinc deposits; *in* Mineral deposits of Canada: a synthesis of major deposit types, district metallogeny, the evolution of geological provinces, and exploration methods, (ed.) W.D. Goodfellow; Geological Association of Canada, Mineral Deposits Division, Special Publication No. 5, p. 185–203.

Paradis, S., Keevil, H., Simandl, G.J., and Raudsepp, M., 2015. Carbonate-hosted nonsulphide Zn–Pb mineralization of southern British Columbia, Canada; Mineralium Deposita, v. 50, p. 923–951. https://doi.org/10.1007/s00126-014-0565-9

Peace, W.M., Wallace, M.W., Holdstock, M.P., and Ashton, J.H., 2003, Ore textures within the U lens of the Navan deposit; Mineralium Deposita, v. 38, p. 568–584. https://doi.org/10.1007/s00126-002-0340-1

Price, R.A., 1981. The Cordilleran foreland thrust and fold belt in the southern Canadian Rocky Mountains; *in* Thrust and nappe tectonics, (ed.) K.R. McClay and N.J. Price; Geological Society of London, Special Publication No. 9, p. 427–448. https://doi.org/10.1144/GSL.SP.1981.009.01.39

Price, R A., 1994. Cordilleran tectonics and the evolution of the Western Canada Cordilleran Tectonics and the Evolution of the Western Canada Sedimentary Basin; *in* Geological Atlas of the Western Canada Sedimentary Basin; (comp.) G.D. Mossop and I. Shetson; Canadian Society of Petroleum Geologists and Alberta Research Council, Calgary, p. 13–24.

Putnis, A., 2002. Mineral replacement reactions: from macroscopic observations to microscopic mechanisms; Mineralogical Magazine, v. 66, no. 5, p. 689–708. https://doi.org/10.1180/0026461026650056

Putnis, A., 2009. Mineral replacement reactions; in Thermodynamics and Kinetics of Water-Rock Interaction, (ed) E.H. Oelkers and J. Schott; Mineralogical Society of America, Reviews in Mineralogy and Geochemistry, v. 70, p. 87–124.

Qing, H., 1991. Diagenesis of Middle Devonian Presqu'ile dolomite Pine Point NWT and adjacent subsurface; PhD thesis, McGill University, Montreal, P.Q., 292 p.

Qing, H., 1998. Petrography and geochemistry of early-stage, fine-and medium-crystalline dolomites in the Middle Devonian Presqu'ile Barrier at Pine Point, Canada; Sedimentology, v. 45, no. 2, p. 433–446. https://doi.org/10.1046/j.1365-3091.1998.0154f.x

Qing, H. and Mountjoy, E.W., 1992. Large-scale fluid flow in the Middle Devonian Presqu'ile barrier, Western Canada Sedimentary Basin; Geology, v. 20, no. 10, p. 903–906. https://doi.org/10.1130/0091-7613(1992)020%3C0903:LSFFIT%3E2.3.CO;2

Qing, H. and Mountjoy, E.W., 1994. Origin of dissolution vugs, caverns, and breccias in the Middle Devonian Presqu'ile barrier, host of Pine Point Mississippi Valley-type deposits; Economic Geology, v. 89, no.4, p. 858–876. https://doi.org/10.2113/gsecongeo.89.4.858

Rhodes, D., Lantos, E.A., Lantos, J.A., Webb, R.J., and Owens, D.C., 1984. Pine Point ore bodies and their relationship to the stratigraphy, structure, dolomitization and karstification of the Middle Devonian Barrier Complex; Economic Geology, v. 79, no. 5, p. 991–1055. https://doi.org/10.2113/gsecongeo.79.5.991

Roedder, E., 1968a. Temperature, salinity, and origin of the ore-forming fluids at Pine Point, Northwest Territories, Canada, from fluid inclusion studies; Economic Geology, v. 63, no. 5, p. 439-450. https://doi.org/10.2113/gsecongeo.63.5.439

Roedder, E., 1968b. Non-colloidal origin of colloform textures in sphalerite ores; Economic Geology, v. 63, no. 5, p. 451–471. https://doi.org/10.2113/gsecongeo.63.5.451

Roedder, R., 1968c. Sphalerite color banding: Lack of correlation with iron content, Pine Point, Northwest Territories, Canada; American Mineralogist, v. 53, no. 9–10, p. 1523–1529.

Roedder, E., 1984. Fluid inclusions; *in* Reviews in mineralogy, (ed.) P.H. Ribbe; Mineralogical Society of America, v. 12, 644 p.

Sasaki, A., and Krouse, H.R., 1969, Sulfur isotopes and the Pine Point lead-zinc mineralization; Economic Geology, v. 64, p. 718–730. https://doi.org/10.2113/gsecongeo.64.7.718

Sangster, D.F., 1970. Metallogenesis of some Canadian lead-zinc deposits in carbonate rocks; Geological Association of Canada-Mineralogical Association of Canada, Abstracts with Proceedings, v. 22, p. 27–36.

Sangster, D.F. and Carrière, J.J., 1991. Preliminary studies of fluid inclusions in sphalerite from the Robb Lake Mississippi Valley-type deposit, British Columbia; Geological Survey of Canada, Current Research Part E, Paper No. 91-1E, p. 25–32. https://doi.org/10.4095/132625

Savard, M.M., Chi, G., Sami, T., Williams-Jones, A.E., and Leigh, K., 2000. Fluid inclusion and carbon, oxygen and strontium isotope study of the Polaris Mississippi Valley-type Zn-Pb deposit, Canadian Arctic Archipelago: implications for ore genesis; Mineralium Deposita, v. 35, no. 6, p. 495–510. https://doi.org/10.1007/s001260050257

Seal, R., 2006, Sulfur isotope geochemistry of sulfide minerals; *in* Sulfide Mineralogy and Geochemistry, (ed.) D.J. Vaughan; Mineralogical Society of America, Reviews in Mineralogy and Geochemistry, v. 61, p. 633–677.

Steele-MacInnis, M., Lecumberri-Sanchez, P., and Bodnar, R.J., 2012. HOKIEFLINCS_H2O-NACL: A Microsoft Excel spreadsheet for interpreting microthermometric data from fluid inclusions based on the PVTX properties of H_2O-NaCl; Computer Geoscience, v. 49, p. 334–337. https://doi.org/10.1016/j.cageo.2012.01.022

Stephenson, R.A., Zelt, C.A., Ellis, R.M., Hajnal, Z., Morel-a-l'Huissier, P., Mereu, R.F., Northey, D.J., West, G.F., and Kanasewich, E.R., 1989. Crust and upper mantle structure and the origin of the Peace River Arch; Bulletin of Canadian Petroleum Geology, v. 37, p. 224–235. https://doi.org/10.35767/gscpgbull.37.2.224

Taylor, H.P., Jr., 1977. Water/rock interactions and the origin of H_2O in granitic batholiths; Journal of the Geological Society, v. 133, no. 6, p. 509–558. https://doi.org/10.1144/gsjgs.133.6.0509

Turner, W. A., 2006. Microthermometric study of fluids associated with Pb–Zn mineralization in the vicinity of the Pine Point mining camp; *in* Potential for carbonate-hosted lead-zinc Mississippi Valley-type mineralization in northern Alberta and southern Northwest Territories: Geoscience Contributions, Targeted Geoscience Initiative, (ed.) P.K. Hannigan; Geological Survey of Canada, Bulletin 591, p. 221–240. https://doi.org/10.4095/222941

Vandeginste, V., Swennen, R., Gleeson, S.A., Ellam, R.M., Osadetz, K., and Roure, F., 2007. Geochemical constraints on the origin of the Kicking Horse and Monarch Mississippi Valley-type lead-zinc ore deposits, southeast British Columbia, Canada; Mineralium Deposita, v. 42, no. 8, p. 913–935. https://doi.org/10.1007/s00126-007-0142-6

Wheeler, J.O., and McFeely, P., 1991. Tectonic assemblage map of the Canadian Cordillera and adjacent parts of the United States of America; Geological Survey of Canada, Canadian Geoscience Map 1712A, scale 1:2 000 000. https://doi.org/10.4095/133549

Wilkinson, J.J., 2001. Fluid inclusions in hydrothermal ore deposits; Lithos, v. 55, no. 1–4, p. 229–272. https://doi.org/10.1016/S0024-4937(00)00047-5

Wilkinson, J.J., 2014. Sediment-hosted zinc-lead mineralization: processes and perspectives; *in* Geochemistry of mineral deposits: Treatise on geochemistry (second edition), (ed.) S.D. Scott; Elsevier, v. 13, p. 219–249. https://doi.org/10.1016/B978-0-08-095975-7.01109-8

Wilkinson, J.J., 2017. Metastable freezing: A new method for the estimation of salinity in aqueous fluid inclusions; Economic Geology, v. 112, no. 1, p. 185–193. https://doi.org/10.2113/econgeo.112.1.185